Politecnico di Milano
Dipartimento di Energia
Doctoral Program in
Energy and Nuclear Science and Technology

Tungsten-based coatings for magnetic fusion research: damage and hydrogen retention

Doctoral Dissertation of:
Andrea Pezzoli

Supervisors:
Prof. Matteo Passoni, Dr. David Dellasega

Tutor:
Prof. Carlo E. Bottani

The Chair of the Doctoral Program:
Prof. Carlo E. Bottani

Year 2016 – Cycle XXIX

Abstract

PLASMA Facing Materials (PFMs) are fundamental components in fusion devices like ITER. Since PFMs face the thermonuclear plasma directly, they are subjected to various phenomena which can dramatically change their properties. Different PFM solutions were tested, but tungsten (W) is currently the most promising material to be used. Despite its favorable properties, W can suffer various modifications in the harsh environment foreseen in ITER. These modifications can lead to forming re/co-deposited W-based layers, which exhibit different properties from those of W. These changes and their effects on the overall system must be known and predictable.

The main goal of this Ph.D. thesis is to provide an experimental investigation, at the laboratory scale, into non-conventional W-based films and their behaviors when faced to divertor-like plasma. The pulsed laser deposition technique is used to deposit tungsten-based films with tailored properties. Thermal annealing procedures are performed to have an extra degree of freedom in controlling film properties. The most relevant W-based coatings are exposed to divertor-like plasma to study their property modifications and different deuterium retention values, with the aim of finding the relationship between film properties and their behavior when exposed to different plasma conditions.

The results presented in this thesis can provide valuable insights into the use of a versatile deposition technique to produce films relevant for nuclear fusion research and into the physics of the behavior of these non-conventional W-based films when exposed to divertor-like plasmas.

Sinossi

In ITER, il ruolo dei materiali direttamente esposti al plasma termonucleare (dall' inglese *Plasma Facing Materials*, PFMs) è cruciale. In queste condizioni, i PFMs possono subire diversi effetti che contribuiscono a modificare le proprietà degli stessi. Durante le ricerche sulla fusione termonucleare controllata diversi PFMs sono stati testati, ma attualmente la soluzione più promettente è quella rappresentata dal tungsteno (W). Il W può essere fortemente modificato quando lavora in ambienti aggressivi come quello previsto in ITER. In queste condizioni si può assistere alla formazione di depositi di materiale precedentemente eroso. Queste strutture hanno tipicamente proprietà molto diverse rispetto a quelle del tungsteno. Questi cambiamenti e il loro effetto sul sistema devono essere conosciuti e pronosticabili.

L' obiettivo principale di questa tesi di dottorato è quello di fornire un' indagine sperimentale riguardo depositi di tungsteno non convenzionali e il loro comportamento quando esposti a un plasma che simula quello che sarà presente nella zona del divertore di ITER (dall'inglese *divertor-like*). La tecnica di deposizione a laser pulsata è stata utilizzata per realizzare film di W con le proprietà desiderate; trattamenti termici sono stati condotti per poter meglio controllare le proprietà dei depositi. I depositi di W più interessanti sono stati selezionati per essere esposti a dai plasmi divertor-like con l' obiettivo di comprendere la relazione esistente tra le proprietà del deposito e il suo comportamento quando esposto a un plasma.

I risultati presentati in questa tesi possono fornire utili informazioni utili riguardo la possibilità di utilizzare una tecnica sperimentale versatile per realizzare depositi con proprietà rilevanti per le ricerche sulla fusione nucleare e riguardo la fisica del comportamento di questi depositi non convenzionali di W quando esposti a dei plasmi divertor-like.

Contents

Introduction

Human development strongly depends on the ability to access energy sources. The progress made in the twentieth century was possible because of the assumption that humans have unlimited energy resources.

Today, fossil fuels cover about 80% of the global energy demand, even though these sources may be exhausted in 100-200 years and are responsible for more than 70% of anthropogenic greenhouse emissions, which are related to global warming and its harmful effects.

There is no unique road-map for going beyond our dependency on fossil fuels. Some options involve mature technological development (e.g. hydro power, wind power, nuclear fission), others are currently being investigated intensively (e.g. *next generation* in photovoltaics and nuclear fission). Amongst these various possibilities, nuclear fusion is believed to have many of the advantages typical of renewable energy sources (no greenhouse emissions, virtually unlimited fuel reserves) and the benefits of fossil fuels (uninterrupted power delivery, very high power density).

The basic idea behind nuclear fusion is to reproduce at the laboratory-scale what happens in a star. Basically, nuclear fusion is the process in which 2 light nuclei react together to form a heavier nucleus. During this reaction, other particles and energy can be released. To reach a favorable condition, in which the two reactant nuclei can interact with each other, it is necessary that they have sufficient energy to overcome their reciprocal Coulomb repulsion energy. The Coulomb barrier is minimized in the case of hydrogen isotopes and, nowadays, the most accessible nuclear reaction seems to be that which involves deuterium and tritium and, for this reason, the first generation nuclear fusion power plants foresee the use of this reaction. To overcome the Coulomb barrier between deuterium and tritium, it is necessary to supply them with a sufficient amount of kinetic energy, at least in the order of keV. In order to reach these kinetic energy values, the system must heat up to a temperature in the order of tens of millions of K. Under these conditions, atoms are completely ionized by forming the so-called plasma state. In order to achieve a net energy gain from nuclear fusion reactions, the required conditions must be satisfied for a sufficient time; this is possible by confining the plasma properly. Since a plasma is made by electrical charge particles, one possible confinement solution is to use magnetic fields. Nowadays, the so-called tokamak configuration is regarded as the reference design for nuclear fusion power plants that use magnetic confinement. The most advanced tokamak experiment is ITER, currently under construction in Cadarache (France). ITER aims to take a fundamental step in the transition from experimental studies to full-scale electricity-producing fusion power plants. In particular, ITER aims to demonstrate net energy production from a magnetically-confined thermonuclear plasma and provide the technological and engineering knowledge necessary for making the first demonstrative nuclear fusion power plant (DEMO).

Given its complexity, ITER is one of the greatest challenges in human history. In particular, the comprehension of plasma-material interactions is a key issue because the simultaneous presence of plasma facing materials and thermonuclear plasma generates various effects, both on plasma and on materials. In particular, during thermonuclear plasma discharges, plasma facing materials must sustain very energetic neutrons (14.1 MeV neutrons able to generate radiation fields of about $2 \cdot 10^3$ Gy s^{-1}), high particle fluxes (up to 10^{24} $m^{-2}s^{-1}$) and extreme heat loads (20 MW m^{-2} during steady-state operations and 10 GW m^{-2} during off-normal events). All these effects modify the properties of plasma facing materials in depth up to having evident erosion and sputtering phenomena, changes in material surface morphology and crystallinity, defect creation and melting phenomena. Since tokamaks are closed systems, eroded materials must re/co-deposit somewhere else. The re/co-deposited layers can exhibit different properties with regard to those of plasma facing materials and, therefore, their behavior, during the interaction with thermonuclear plasma, can be totally different and non-predictable. It is fundamental to fill these knowledge gaps by using different approaches, one of which is to use an advanced material science method which consists in using suitable deposition techniques to produce relevant coatings for nuclear fusion research to be tested in fusion-relevant experiments, e.g. linear divertor-like plasma generators.

This doctoral thesis uses this approach and aims to provide an experimental investigation, at the laboratory-scale, to study the properties of non-conventional W-based materials, which are relevant for nuclear fusion research, and to understand their behavior when faced to tokamak-like plasmas. The research activities, reported here, have been developed within the framework of the Energy and Nuclear Science and Technology (STEN) Ph.D. program at the Politecnico of Milan (Italy). The present doctoral dissertation is organized as follows.

Chapter 1 In the first chapter, the general scientific background is reported. After an introductory part regarding the basic principles related to energy production by nuclear fusion, the focus is on the current methods used to confine a thermonuclear plasma. In particular, possible magnetic confinement methods are discussed, the tokamak configuration is presented, and some details about the ITER project are given. The tokamak solution, which is the most widely studied, is described by touching on the most important topics, with particular attention to those related to the plasma facing materials.

Chapter 2 The second chapter deals with the topic of the use of tungsten in magnetic fusion systems. After a general introduction about the plasma wall interaction and the possible choices of materials for the tokamak first wall, the focus is on the use of tungsten as a first wall material; in particular, ITER and supporting-ITER tokamaks, which adopt tungsten as a plasma facing material, are presented. Emphasis is given to the problem of re/co-deposition phenomena and hydrogen isotope retention. Since the available results, coming from tokamak experiments, are limited, alternative laboratory-scale approaches are introduced.

Chapter 3 The third chapter presents the specific goals of this thesis and the experimental methodology employed to pursue them. A suitable physical vapor deposition technique has been used to produce W-based films, which are relevant for magnetic fusion research in order to study their properties and to test their behaviors when faced to a plasma in conditions relevant for ITER and future reactors. In addition, the experimental tools and techniques used in this thesis are also introduced in Chapter 3.

Chapter 4 The fourth chapter describes the production of tailored W-based films by means of Pulsed Laser Deposition. The films (metallic and oxide and nitride) are designed and tailored to cover a widespread range of structures and morphologies (from compact to porous) that could be present in the first wall of a future fusion reactor. These films are characterized with different techniques and thermally annealed at ITER-relevant temperatures to understand modifications induced by different temperature regimes.

Chapter 5 The fifth chapter is devoted to the description of ITER-relevant plasma exposures of selected W-based samples. Particular attention is paid to deuterium plasma exposures. Different tungsten-based films are exposed to plasmas with different properties (e.g. flux, temperature, voltage bias) to investigate the morphological modifications induced by the plasma, the mutual relationship between film features and plasma properties and the role of film properties in the retained D. In particular, both metallic films and tungsten-oxygen films are tested. In conclusion, a preliminary exposure of a few samples to mixed helium-deuterium plasma is presented.

Chapter 6 Finally, the sixth chapter presents the main conclusions that can be extracted from this Ph.D. thesis, together with some possible future developments of the topics here addressed.

The original contents of this Ph.D. thesis have led to the publication of the following peer-reviewed papers, ordered by year:

- A. Pezzoli, D. Dellasega, V. Russo, A. Gallo, P. A. van Emmichoven, M. Passoni. Thermal annealing and exposure to divertor-like deuterium plasma of tailored tungsten oxide coatings. *Journal of Nuclear Materials*, 463:1041-1044, 2015.
- M.H.J. 't Hoen, D. Dellasega, A. Pezzoli, M. Passoni, A. W. Kleyn, P. A. Zeijlmans van Emmichoven. Deuterium retention and surface modifications of nanocrystalline tungsten films exposed to high-flux plasma. *Journal of Nuclear Materials*, 463:989-992, 2015.
- D. Dellasega, S. M. Pietralunga, A. Pezzoli, V. Russo, L. Nasi, C. Conti, M. J. Vahid, A. Tagliaferri, M. Passoni. Tungsten oxide nanowires grown on amorphous-like tungsten films. *Nanotechnology*, 26(36):365601, 2015.
- E. Besozzi, D. Dellasega, A. Pezzoli, C. Conti, M. Passoni, M. G. Beghi. Amorphous, ultra-nano- and nano-crystalline tungsten-based

coatings grown by Pulsed Laser Deposition: mechanical characterization by Surface Brillouin Spectroscopy. *Materials & Design*, 106:14-21, 2016.

The results of this Ph.D thesis were presented at several International Conferences, Workshops, Schools and Meetings, listed below:

- A. Pezzoli, D. Dellasega, V. Russo, A. Gallo, P. A. van Emmichoven, M. Passoni. *Tungsten coatings and tungsten compounds exposed to divertor-like plasmas: retention and structural properties.* 21st International Conference on Plasma Surface Interactions in Controlled Fusion Devices Conference (PSI-21). Kanazawa (Japan), May 2014. Poster presentation.

- A. Pezzoli. *Study of the properties of tungsten and tungsten compound coatings for magnetic fusion research: damage, hydrogen retention and permeation.* 4th Ph.D. FuseNet Event. Lisbon (Portugal), November 2014. Attendance and poster presentation.

- A. Pezzoli, D. Dellasega, S. Möller, B. Unterberg, M. Passoni. *Deuterium retention dynamics in tungsten compound layers.* 15th International Conference on Plasma-Facing Materials and Components for Fusion Applications (PFMC-15). Aix-en-Provence (France), May 2015. Poster presentation.

- A. Pezzoli. *Study of the properties of tungsten and tungsten compound coatings for magnetic fusion research: damage, hydrogen retention and permeation.* 56th course on Atoms and Plasma in Super-Intense Laser fields. Erice (Italy), July 2015. Attendance, poster presentation and best poster award.

- A. Pezzoli, D. Dellasega, V. Russo, C. Conti, M. Passoni. *Pulsed Laser Deposition of tailored Tungsten and Tungsten Oxide films.* 13thth International Conference on Laser Ablation, Cairns (Australia), September 2015. Oral presentation.

- A. Pezzoli. *Study of the properties of tungsten and tungsten compound coatings for magnetic fusion research: damage, hydrogen retention and permeation.* 5th Ph.D. FuseNet Event. Prague (Czech Republic), November 2015. Attendance and poster presentation.

- A. Pezzoli, D. Dellasega, S. Möller, A. Gallo, M. H. J. 't Hoen, P. A. Zeijlmans van Emmichoven, B. Unterberg, M. Passoni. *Production of tungsten coatings with controlled morphology and gas inclusion for* *deuterium retention studies.* 13th International Workshop on Hydrogen Isotopes in Fusion Reactor Materials (IWHIFR-2016), Milano (Italy), June 2016. Oral presentation.

- D. Dellasega, A. Pezzoli, V. Russo, A. Gallo, P. A. Zeijlmans van Emmichoven, Matteo Passoni. *Amorphous tungsten oxide layers exposed to Magnum-PSI divertor-like plasma: retention, morphology and structural properties.* 28st Symposium on Fusion Technology (SOFT-2014). San Sebastian (Spain), September 2014. Poster presentation. (presented by D. Dellasega)
- D. Dellasega, A. Pezzoli, S. Möller, B. Unterberg, M. Passoni. *Deuterium retention of nanostructured tungsten coatings exposed to divertor-like D plasmas.* 22st International Conference on Plasma Surface Interactions in Controlled Fusion Devices Conference (PSI-22). Rome (Italy), May 2016. Poster presentation. (presented by D. Dellasega)

1

Nuclear fusion

In this chapter the main topics regarding nuclear fusion are reviewed. In section 1.1 the basic principles of nuclear fusion will be introduced. In section 1.2, the most studied nuclear fusion reactions in the field of power production will be illustrated. In order to produce energy from nuclear reactions it is necessary to meet strict requirements (e.g temperature, density, power balance) that are described in section 1.3. If these conditions are fulfilled, the system state reaches the so-called *thermonuclear plasma*, which must be confined. One possible solution is offered by devices named *tokamaks*, described generally in section 1.5, with a particular focus on these topics: confinement solution, heating system, diagnostics and *Plasma Facing Components* (PFCs).

1.1 Basic principles

The energy balance of a nuclear reaction is given by Einstein's relation:

$$\mathrm{E} = \Delta \mathrm{M} \mathrm{c}^2 \tag{1.1}$$

where c is the light speed and ΔM is the mass defect, i.e. the difference between the rest mass of reactants and products. If E is positive, a certain amount of energy has been produced during the reaction; vice versa, if E is negative, the reaction requires energy in order to happen.

From the binding energy curve, reported in figure 1.1, it is possible to observe that the most stable nuclei have a mass number (A) of about 56. For nuclei with $\mathrm{A} < 56$ the binding energy increases with A, while for nuclei with $\mathrm{A} > 56$ it decreases with A. Due to this behavior, it is

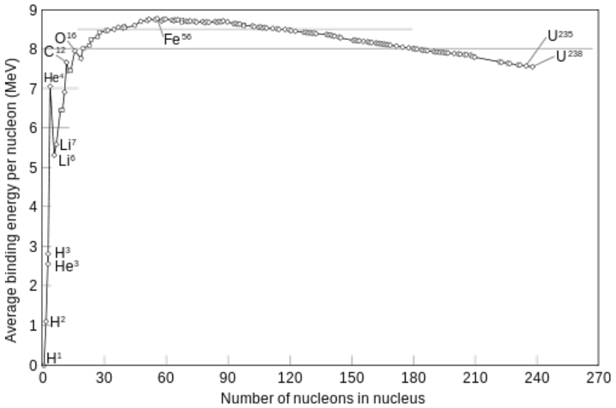

Figure 1.1: *Binding energy per nucleon (MeV) versus mass number (A).*

possible to obtain exothermic nuclear fission reactions for A > 56 and exothermic nuclear fusion reactions for A < 56. As a source of energy, the fusion approach has several advantages compared to the fission approach: nuclear fusion fuels mainly consists of light nuclei, which are abundant and available in nature, the released energy per nucleon is about 5-6 MeV compared to 0.8 MeV for the conventional fission reaction of ^{235}U and the reaction products are nonradioactive nuclei. Nevertheless, fusion reactions have some drawbacks: fusion reactions involve strong nuclear force, which has a typical range of $\approx 10^{-15}$ m, and, for this reason, the nuclei must be within this distance to react. To reach this reaction distance, reactant nuclei must overcome the Coulomb barrier that represents the activation energy for the fusion reaction, e.g. using a classical electrostatic approach, the activation energy for the deuterium-tritium (D-T) fusion reaction is about 0.1 MeV while, when the tunneling phenomena are also taken into account, this value is reduced to $\approx$ 10 keV [1].

This amount of energy can be provided to reactants by heating them. Remembering that the mean kinetic energy of an ideal gas can be written as $\mathrm{E_K} = \frac{3}{2}\mathrm{k_B T}$, this means that to overcome a barrier of $\approx$ 10 keV a T of $\approx 10^8$ K is necessary. At this temperature regime, the matter is in the state of plasma, i.e. the atoms and molecules are separated into nuclei and unbound electrons. The hot plasma made of nuclear fuels is also called *thermonuclear plasma*, and this way of obtaining fusion power by using high temperatures is called *thermonuclear fusion*.

Fusion reaction research was widely developed after the Second World War, mainly due to its potential use for military purposes (hydrogen bomb, 1952). However, the scientific community understood the potential of this technology and various research programs with different approaches were begun in order to develop a full-scale electricity-producing fusion reactor plan [2].

1.2 Fusion reactions

The Coulomb barrier is proportional to the square power of the atomic number, so heavier nuclides require higher temperatures to react. For energetic purposes, the reactions with lighter nuclides (D, T and ^{3}He) are considered more feasible:

$$\begin{aligned} &\mathrm{D} + \mathrm{D} \rightarrow \begin{cases} ^3\mathrm{He} + \mathrm{n} + 3,27\ \mathrm{MeV} & \mathrm{p}{=}50\% \\ \mathrm{T} + \mathrm{H} + 4,03\ \mathrm{MeV} & \mathrm{p}{=}50\% \end{cases} \\ &\mathrm{D} + {}^3\mathrm{He} \rightarrow {}^4\mathrm{He} + \mathrm{H} + 18,3\ \mathrm{MeV} \\ &\mathrm{D} + \mathrm{T} \rightarrow \mathrm{n} + {}^4\mathrm{He} + 17,6\ \mathrm{MeV} \end{aligned}$$

In order to highlight the most important parameters for a nuclear fusion reaction, consider a system made by two different populations, *i* and *j*. The volumetric rate of reactions can be written as:

$$\mathrm{r_{i,j}} = \mathrm{n_i n_j} \left\langle \sigma \mathrm{v} \right\rangle_{\mathrm{i,j}} \tag{1.2}$$

where $\mathrm{n_i}$ and $\mathrm{n_j}$ are the volumetric particles densities, σ is microscopic reaction cross-section at relative velocity v and $\left\langle \sigma \mathrm{v} \right\rangle_{\mathrm{i,j}}$ denotes the average operation on velocity distribution. Remembering the equations 1.1 and 1.2, the power per unit volume obtained from the nuclear process is:

$$\mathrm{P_{F,ij}} = \mathrm{E_{i,j} n_i n_j} \left\langle \sigma \mathrm{v} \right\rangle_{\mathrm{i,j}} \tag{1.3}$$

This expression highlights two figures of merit to evaluate the feasibility of a fusion nuclear reaction: the energy released by reaction $\mathrm{E_{i,j}}$ and the reaction rate $\left\langle \sigma \mathrm{v} \right\rangle_{\mathrm{i,j}}$. In particular, the $\left\langle \sigma \mathrm{v} \right\rangle_{\mathrm{i,j}}$ for the reaction reported above, hypothesizing a Maxwell velocity distribution, is shown in figure 1.2 as a function of temperature.

The **D-D reaction** is interesting because it involves only D as nuclear fuel. D is stable, with an isotopic concentration of ≈ 0.02 % and it can be extracted by exploiting the isotopic separation of water and then the electrolysis of the obtained heavy water. On the contrary, these reactions have the lowest reaction rate and released energy compared to the other candidate fusion reactions. For these reasons, the construction of a nuclear power plant based on D-D reaction turns out to be extremely complex, e.g plasma conditions are severe.

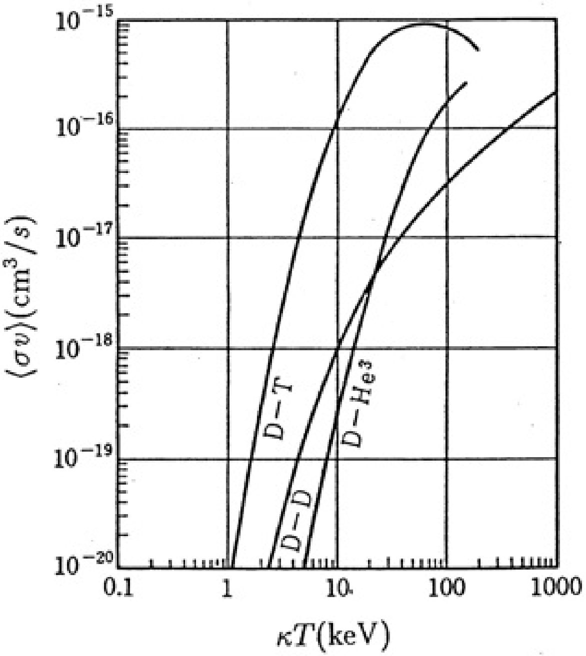

Figure 1.2: *$\langle\sigma v\rangle$ averaged on a Maxwell velocity distribution, as a function of temperature T, for the nuclear fusion reactions D-D, D-T and ^{3}He-D.*

The ^{3}**He-D reaction** exhibits some useful features: the released energy is the highest in the candidate fusion reactions, the reactants and products are nonradioactive and there is no production of neutrons. This means that there is no activation and neutron damaging of reactor materials. However, the ^{3}He-D reaction has a relatively low reaction rate and ^{3}He is quite rare in nature (isotopic abundance ≈ 0.000137 %).

The **D-T reaction** is the most promising for use in power production. It has the highest reaction rate and the lowest activation energy ($\approx 10^8$ K) with a relatively high released energy (17.6 MeV). This energy is shared between the ^{4}He (3.5 MeV) and the neutron (14.1 MeV). This fast neutron flux, interacting with reactor materials, induces severe damage and activation phenomena. Moreover, T is radioactive ($T_{\frac{1}{2}} = 12.33$ years) and must be artificially produced. A possible solution, developed to produce T, is to use the same neutron flux to trigger these reactions with lithium:

$$^6\mathrm{Li} + \mathrm{n} \rightarrow {}^4\mathrm{He} + \mathrm{T} + 4,8\mathrm{MeV}$$
$$^7\mathrm{Li} + \mathrm{n} \rightarrow {}^4\mathrm{He} + \mathrm{T} + \mathrm{n}' - 2,5\mathrm{MeV}$$

^{6}Li and ^{7}Li have a 7.5 % and 92.5 % isotopic concentration, respectively.

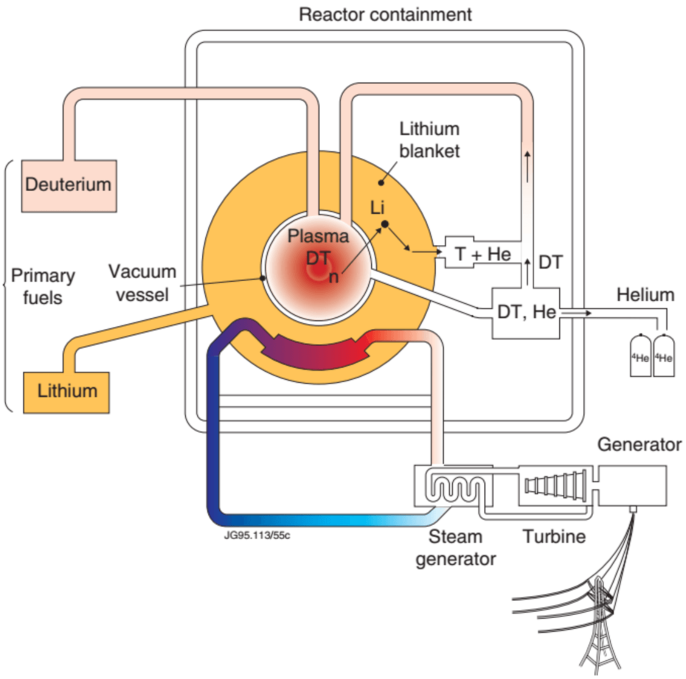

Figure 1.3: *Schematic design of a D-T nuclear power plant.*

Both reactions can happen: the first is exothermic and the second is endothermic. Thanks to its unique features, molten Li compound can be used with triple function, i.e. T breeder, neutron moderator and primarily coolant, as happens in generation IV fission power plants.

As stated before, due to its favorable physical properties, the first generation of a nuclear fusion power plant should operate with D-T as the fuel mixture. A simplified design scheme of a D-T nuclear power plant is reported in figure 1.3. The knowledge acquired during the construction and the operation of these power plants could bring about the development of a D-D power plant: although, as said before, the D-D reaction shows a lower value of $\langle \sigma v \rangle_{i,j}$ and $E_{i,j}$ and despite the drawbacks highlighted earlier it looks very attractive, because, when running a fusion power plant with a D-D fuel mixture, it is possible to drastically reduce radiological problems.

1.3 Energy balance in a thermonuclear plasma

For energetic purposes, thermonuclear plasma has to satisfy some requirements. Considering a steady state plasma made up by a mixture of D-T, the following power per unit volume balance must be verified:

$$\mathrm{P_{ext}} + \mathrm{P}_\alpha = \mathrm{P_R} + \mathrm{P_Q} \tag{1.4}$$

where the left-hand side is the power gained by the plasma and the right-hand side the power lost by the plasma. $\mathrm{P_{ext}}$ is the power per unit volume provided to the plasma by external sources (if there are any) and P_α is the fusion power associated with α particles generated during the D-T fusion reaction and that stays in the plasma. Neutrons, due to their neutral charge, can easily escape from the plasma: for this reason the power transported by neutrons can easily escape from the plasma towards the heat transfer system. P_α in a D-T plasma is given by:

$$\mathrm{P}_\alpha = \frac{\mathrm{n}^2}{4} \langle\sigma \mathrm{v}\rangle_{\mathrm{D,T}} \, \mathrm{E}_\alpha \tag{1.5}$$

where n is plasma density and $\langle\sigma \mathrm{v}\rangle_{\mathrm{D,T}}$ is the reaction rate of the D-T reaction and $\mathrm{E}_\alpha = 3.5$ MeV. In the left-hand side of equation 1.4, $\mathrm{P_R}$ and $\mathrm{P_Q}$ account radiative losses and diffusive thermal losses, respectively. $\mathrm{P_R}$ is mainly due to Bremsstrahlung X-rays induced by electron-ion scattering phenomena and it is given by:

$$\mathrm{P_R} = \mathrm{c_B} \, \mathrm{Z_{eff}^2} \, \mathrm{n}^2 \, \mathrm{T}^{0.5} \tag{1.6}$$

where $\mathrm{c_B}$ is a constant ($\approx 10^{-34}$ W cm^{-2}), $\mathrm{Z_{eff}^2}$ is the effective atomic number of the plasma: a pure D-T mixture has a $\mathrm{Z_{eff}} = 1$, while, when there are some heavier impurities in the plasma, this value can increase, dramatically increasing radiative losses induced by Bremsstrahlung. Therefore, controlling plasma pollution and choosing appropriate main chamber materials is mandatory in a fusion power plant in order to minimize these losses. In the approximation of steady state plasma, and neglecting the expansion works of the plasma, the term $\mathrm{P_Q}$ can be written as:

$$\mathrm{P_Q} = \frac{3\mathrm{n} \, \mathrm{k_B} \, \mathrm{T}}{\tau_{\mathrm{E}}} \tag{1.7}$$

where τ_{E} is the confinement time of plasma and describes the plasma confinement quality.

Considering equation 1.4, it is possible to produce some relevant requirements for a steady state fusion reaction. $\mathrm{P}_\alpha > \mathrm{P_R}$ is a necessary condition to have a self-sustained chain D-T reaction, not taking into account thermal and radiative losses. Using equations 1.5 and 1.6, it is possible to define:

$$\frac{\langle\sigma \mathrm{v}\rangle_{\mathrm{D,T}}}{\mathrm{T}^{0.5}} > \frac{4\mathrm{c_B}\ \mathrm{Z}_{\mathrm{eff}}^2}{\mathrm{E}_\alpha} \tag{1.8}$$

and it is possible to define the ideal ignition temperature, as:

$$\mathrm{T_{id}} = \frac{\langle\sigma \mathrm{v}\rangle_{\mathrm{D,T}}^2\ \mathrm{E}_\alpha}{4\mathrm{c_B}} \tag{1.9}$$

For the D-T reaction, the $\mathrm{T_{id}}$ is equal to 4.4 keV. For completeness, in the case of the D-D reaction $\mathrm{T_{id}} = 32$ keV, which is a more severe condition compared to the D-T reaction. In order to have a more realistic parameter, $\mathrm{P_Q}$ and $\mathrm{P_R}$ should be included. To estimate the performance of a fusion power plant, the *gain factor* Q must be introduced, defined as:

$$\mathrm{Q} = \frac{\text{nuclear fusion power}}{\text{input power}} \tag{1.10}$$

When the nuclear fusion power is equal to the external input power, $\mathrm{Q} = 1$ and the system reaches the so-called *break even* condition. At the same time, having $\mathrm{Q} > 5$ means that heat power produced by the plasma itself and which remains in plasma is higher than the heat power provided by external sources. If the power produced by plasma can compensate all power losses, theoretically $\mathrm{Pext} \rightarrow 0$ and consequently $\mathrm{Q} \rightarrow \infty$, and in this condition the thermonuclear plasma achieves *ignition.* Taking equation 1.4, the ignition condition can be expressed as:

$$\mathrm{P}_\alpha \geq \mathrm{P_R} + \mathrm{P_Q} \tag{1.11}$$

Substituting equation 1.5, 1.6 and 1.7 in this equation, it is possible to obtain this inequality:

$$\mathrm{n}\tau_{\mathrm{E}} \geq \frac{12\mathrm{k_B}\,\mathrm{T}}{\mathrm{E}_\alpha\langle\sigma \mathrm{v}\rangle - 4\mathrm{c_B}\ \mathrm{Z}_{\mathrm{eff}}^2\,\mathrm{T}^{\frac{1}{2}}} \tag{1.12}$$

For a specific fusion reaction, the left-hand side of equation 1.12 is a function of temperature with a minimum. For the D-T reaction this minimum is found to be $\mathrm{T} \approx 25$ keV, substituting and considering realistic assumption [3], one finds:

$$\mathrm{n}\tau_{\mathrm{E}} \geq 2 \times 10^{14}\ \mathrm{s\ cm^{-3}} \tag{1.13}$$

well known as the *Lawson criterion*, described by engineer and physicist J. D. Lawson in 1955 [3]. The Lawson criterion establishes a constraint on the product of two quantities τ_{E} and n, leaving one degree of freedom. For instance, it is possible to achieve this condition both with a dense plasma (n high) confined for a short time (τ_{E} little), or vice versa. The most widely studied strategies to obtain a fusion reaction with a thermonuclear plasma pursue the approaches described above:

- **inertial confinement** foresees very high particle density ($n \approx 10^{24}$ cm^{-3}) obtained by compressing a solid fuel pellet with high energy lasers or particles beams. In this configuration the confinement time is very short ($\tau_{\mathrm{E}} \approx 10^{-9}$ s). Nowadays, the most advanced facility that conducts investigations into inertial confinement fusion is the *National Ignition Facility* (NIF) located at the Lawrence Livermore National Laboratory (USA). In February 2014, NIF scientists announced the achievement of a gain factor($Q \approx 1.2$) in laser driven fusion experiments, crossing the symbolic break-even point [4]. It is important to note that inertial confinement research projects are strictly connected with military interests, represented today in particular by the technologies of high power lasers; for this reason all investigations in this field are carried out by military institutions.
- **magnetic confinement** takes advantage of the electrically charged state of plasma. Plasma interacts with magnetic and electric fields. By exploiting a proper configuration of magnetic fields it is possible to confine plasma in different configurations. In these schemes plasma has low density ($n \approx 10^{14}$ cm^{-3}) with confinement times of seconds.

This doctoral thesis was developed around the framework of magnetic fusion research: in the following sections, the main characteristics of magnetic fusion devices, in particular, those called *tokamaks*, will be described.

1.4 Magnetic confinement

As previously mentioned, a plasma can interact with electric and magnetic fields. In the case of a plasma in spatially uniform magnetic fields, e.g. that produced by an ideal solenoid, the plasma ions and the electrons move along helicoidal trajectories (Larmor motion) around the magnetic field lines, as illustrated in figure 1.4. By exploiting this approach, it is possible to achieve transverse confinement compared to magnetic field direction and not the axial confinement. To achieve axial confinement two different approaches were developed during magnetic fusion research. The first foresees increasing the magnetic field at the edges of the linear system.

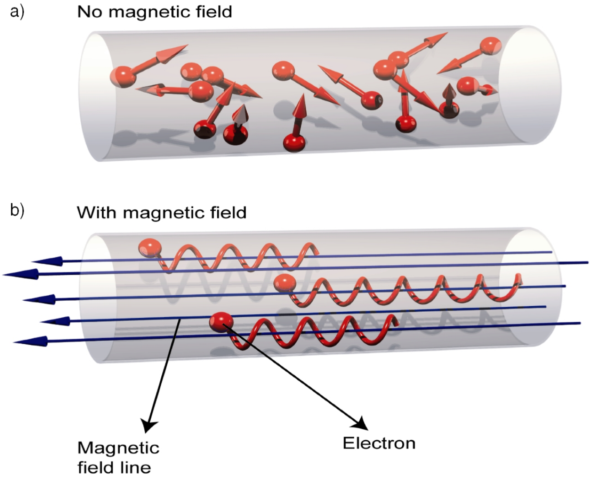

Figure 1.4: *Schematic model of free charged particle (a) and with uniform magnetic field (b).*

So, due to the conservation of particle energy and magnetic dipole, some plasma particles are forced to invert their motion when they reach the edge of the device. This is the so-called mirror phenomenon and the devices that use this to confine plasma are named *mirror machines*. This type of device has some drawbacks, i.e. incomplete particle confinement and complex edge magnetic field configuration to avoid instability. The second strategy results in closing the solenoid, creating a torus-shaped solenoid. In this case the plasma is subjected to a *toroidal magnetic field* (B_T) generated by external coils. That induces a poloidal current (I_P) along the plasma. In this configuration, B_T is not uniform and particle motion is the composition of their usual Larmor motion plus a transverse drift phenomena due to the gradients ($\mathbf{B} \times \nabla B$) and charge separation electrical fields ($\mathbf{E} \times \mathbf{B}$) that bring about particles loss. To overcome this problem, it is necessary to introduce a *poloidal magnetic field* (B_P) that makes it possible to twist the magnetic field lines and to give rise to the so-called magnetic surfaces. A smart way to produce B_P is to induce a toroidal current (I_T) into the plasma itself. The device that exploits this idea is called a *tokamak* (see figure 1.5 (a)). Another solution is to use external coils to create B_P too: this is accomplished in the so-called *stellarator* (see figure 1.5 (b)). Both designs were conceived in the early ’50s: the first in the Soviet Union and the second in USA. In figure 1.5 both schematic designs are reported. Due to Cold War tensions, the Eastern and Western blocs remained unaware of each other’s designs. This situation changed during

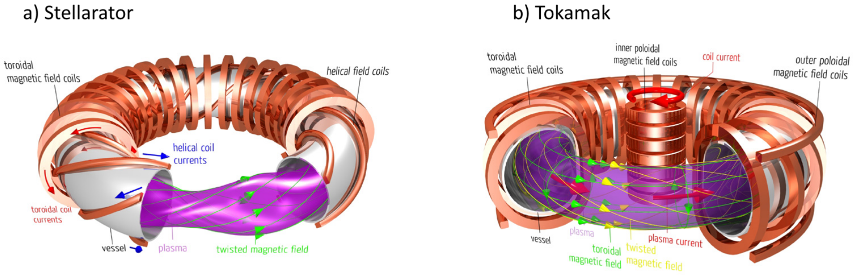

Figure 1.5: *Schematic design of (a) tokamak and (b) stellarator.*

the famous *Atoms for Peace* conference held in Geneva (1958). However, a milestone in magnetic fusion research programs was the IAEA conference in Novosibirsk (1968). During this conference, Lev Artsimovich, the head of the Soviet fusion program, disclosed that the temperature reached in the T-3 tokamak was about 1 keV. This result was received with remarkable suspicion, due also to the indirect methods used at the time to estimate plasma temperature. In the same period, thanks to the invention of the laser, British scientists were developing a more direct way to measure plasma temperature, exploiting the scattering between photons and plasma electrons (*Thomson Scattering*). A delegation of British scientists was invited to measure with their Thomson scattering diagnostic the T-3 plasma temperature. The measurements were in agreement with the ones made by the Soviet scientists. The paper published the following year in *Nature* [5] is now famous, and tokamak configuration has since been considered a better confinement with a simpler design. Beginning in the early '70s, the construction of tokamak machines also began in Western counties: AlCaTor A in 1973 (then AlCaTor C and AlCaTor C-mod at MIT, USA), FT in 1977 (then FTU in Frascati, Italy), TEXTOR in 1978 (Jülich, Germany). A new generation of tokamaks followed in the '80s: T-15 (in Moscow, USSR), JET (in Culham, UK), TFTR (in Princeton, USA), JT-60 (in Naka, Japan), Tore Supra (in Cadarache, France), ASDEX (then ASDEX-Upgrade in Garching, Germany). In particular JET (*Joint European Torus*) is the world's largest operational tokamak. In 1997, this device, with a fuel mixture of D-T, achieved a fusion power of 16 MW ($Q \approx 0.7$), still the world fusion power generation record for a tokamak device [6].

Today, tokamak configuration is regarded as a reference design for magnetic fusion power plants. Indeed, the most advanced experiment in the field of magnetic confinement and one of the most challenging projects in the world today is the tokamak ITER (*the way* in Latin), that is being built in Cadarache (France) [7]. It should demonstrate fusion power production feasibility. The machine has been designed [7] to:

- produce 500 MW with 1000 s plasma discharge, achieving gain factor Q ≈ 10, e.g as mentioned above, the present gain factor record was established in the JET tokamak in 1997 with Q ≈ 0.7 [6];
- demonstrate the integrated operation of fusion power plant technologies;
- achieve self-sustained D-T plasma;
- test the feasibility of in-vessel T generation;
- show the safety characteristics of a fusion device.

The ITER project is a global collaboration involving 7 partners (China, the European Union, India, Japan, South Korea, Russia and the USA), which share the cost of the project, about €15 billion [7]. The ITER Agreement between the parteners was signed on 21 November 2006 at the Élysée Palace, in Paris after more than 15 years of negotiations and design studies. The work on the ITER site, which is at Cadarache (France), started officially on January 2007. It is expected to have the first H plasma by the end of 2025 and full D-T operation by 2027 [7].

1.5 The tokamak in a nutshell

In this section, a synthetic overview of a tokamak scheme is given, with the goal of distinguishing the main systems required to confine, heat and monitor thermonuclear plasma. Magnetic fields are used to confine thermonuclear plasma; in section 1.5.1, coil configuration is discussed. To reach and maintain plasma state, it is necessary to heat the system with different strategies, as discussed in section 1.5.2 and to monitor in time and space the plasma properties with different systems (section 1.5.3). This part is preliminary in order to introduce, in section 1.5.4, the tokamak components directly faced toward plasma: the so-called Plasma Facing Components (PFCs). The materials chosen to make PFCs and their interaction with thermonuclear plasma will be discussed extensively in chapter 2. A more complete description of tokamak configuration can be found in [8].

1.5.1 Plasma confinement in tokamaks

As briefly discussed in section 1.4, to properly confine plasma in a toroidal configuration it is necessary to have both poloidal ($\mathrm{B_P}$) and toroidal magnetic fields $\mathrm{B_P}$. The external coils can be made out of either an ordinary metal material (e.g. copper) or with superconductive alloys (e.g. $\mathrm{Nb_3Sn}$, NbTi). For a future fusion power plant the superconductive choice is mandatory because superconductive magnetic coils have several advantages: they help to avoid excessive power losses and to have a higher magnetic field with less power consumption. However, there are also drawbacks: they can be easily damaged by the radiation field and the superconductor technology is much more complex, e.g. they must be cooled down to liquid helium temperature. The confinement in ITER is provided by *superconducting magnetic coils* made by the $\mathrm{Nb_3Sn}$ alloy. It is typical in a tokamak design that $\mathrm{B_P}$ is directly generated by $\mathrm{I_T}$ that flows along the confined plasma itself. To induce this $\mathrm{I_T}$, tokamak technology uses a system of transformers. The toroidal chamber and thermonuclear plasma concatenated with the magnetic flux produced by the primary transformer winding (typically, a solenoid in the center of the torus). The magnetic flux variation in time induces a current in the plasma that acts as a secondary transformer winding. Due to this time dependence of $\mathrm{B_P}$, tokamaks are typically pulsed regime machines. Since this solution is not admissible in a fusion reactor plant, non-inductive methods to produce $\mathrm{I_T}$ are being studied. Typically, $\mathrm{B_T}$ can be of an order of several Tesla (up to 12-13 Tesla) and $\mathrm{B_P} \approx 0.1\ \mathrm{B_T}$. To control plasma shape and position, tokamak design foresees extra coils for finely tuning $\mathrm{B_P}$. Despite the fact that the first tokamaks were characterized by a circular poloidal section, theoretical studies and experimental tests highlighted that D-shaped plasmas are more stable [8]. In figure 1.6 the schematic configuration of coils present in JET is reported.

1.5.2 Plasma heating system

As mentioned in 1.1, in order to make nuclear fusion reactions possible, it is necessary to heat plasma to very high temperatures. In all tokamaks, the first heating is provided by $\mathrm{I_T}$: $\mathrm{I_T}$, flowing along plasma $\mathrm{I_T}$ produces the so-called *ohmic heating* due to the Joule effect. At low temperatures, this ohmic heating is very strong, but, because the resistance of the plasma varies with temperature as $\mathrm{T}^{-\frac{3}{2}}$, it is less effective at high temperatures. Nevertheless, in a low temperature regime, ohmic heating makes it possible to reach temperatures of a few keV. It is mandatory to

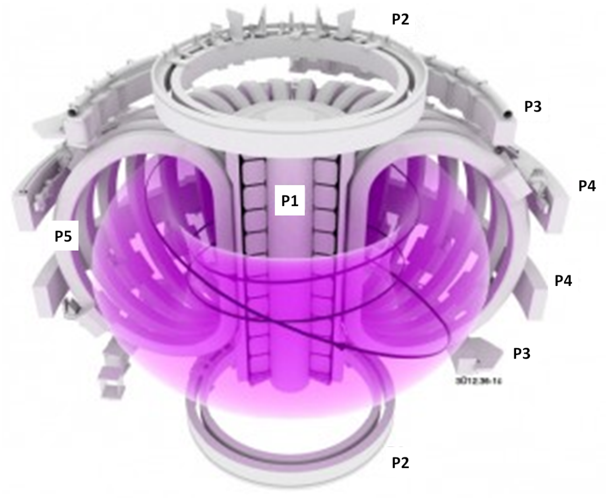

Figure 1.6: *The electromagnetic coil arrangement at JET. The poloidal central solenoid P1 provides the plasma current, while P2, P3 and P4 are the shaping magnets. The toroidal magnets are represented by P5.*

have other heating systems to reach high enough temperatures to favor fusion reactions. Typically, these are *neutral beam injection* [9] systems and *radio-frequency heating* systems [10]. The first foresees injecting into plasma neutral ions with high kinetic energy that then can be transferred by collision to plasma, heating the plasma [8]. Radio-frequency heating involves electromagnetic waves produced by some antennas and then launched into the plasma. By properly selecting the wave frequency it is possible to couple these waves with plasma typical frequencies around ion cyclotron plasma resonance (*ICR heating*, tens of MHz) or around electron cyclotron plasma resonance (*ECR heating*, hundreds of GHz), transferring energy to plasma [8].

1.5.3 Tokamak diagnostics

The objective of all plasma diagnostics is to obtain information about the state of the plasma. Diagnostic systems have the role of monitoring and controlling tokamak operations in different scenarios in order to prevent events that can damage the whole machine. There are different types of diagnostic systems, listed below. A more complete discussion of the principles of plasma diagnostics can be found in [11]

- **Electric and magnetic diagnostics**, used by introducing electrodes or coils of wire in the plasma region, make it possible to determine many plasma properties: plasma current, loop voltage, plasma position and shape, stored plasma energy and current distribution.

- **Neutron diagnostics** reveal neutron flux coming from the fusion reactions. These diagnostics are fundamental for monitoring both properties of thermonuclear plasma and for estimating the neutron flux that interacts with the machines materials.
- **Optical systems** are used to monitor temperature and density of plasma, both in the core and in the peripheral plasma regions (i.e. Thomson scattering, interferometry).
- **Bolometric systems** give information about the spatial distribution of radiated power onto the main chamber.
- **Spectroscopic systems** make it possible to obtain a lot of information on plasma parameters (e.g. impurities, particle fluxes, ion temperature, etc.).
- **Materials diagnostics** with the aim of monitoring the status of material directly facing plasma. Many of these aspects are works in progress.

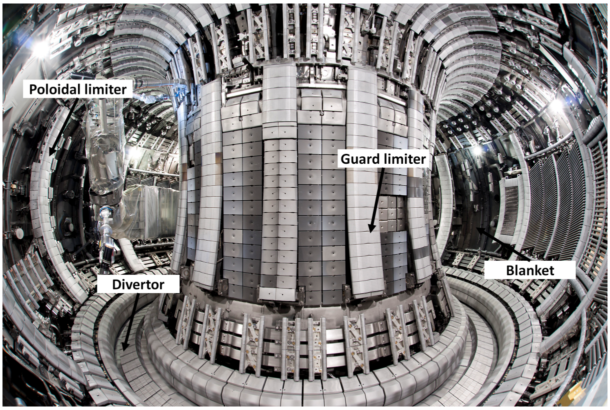

Figure 1.7: *The inner view of JET tokamak with the main PFC highlighted.*

1.5.4 First wall and Plasma Facing Components

The PFCs are those systems directly facing thermonuclear plasma: they are generally said to constitute the so-called *first wall*. They must operate in a very harsh environment while maintaining their functional properties.

It is possible to define the following main components:

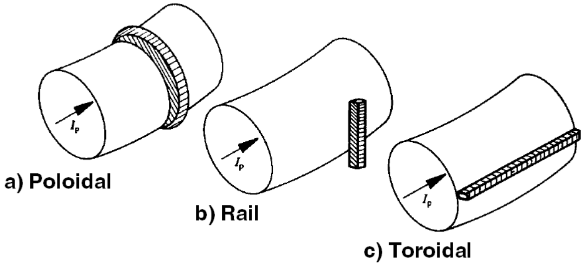

Figure 1.8: *Schematic representation of different types of limiters [8].*

Limiter (figure 1.7): is one of the candidate structures for sustaining the Plasma Material Interaction (PMI) together with the divertor (described properly below). A limiter is a solid surface that protrudes from the blanket toward the plasma region. It can run along the vacuum vessel (*toroidal limiter*) or along the poloidal section (*poloidal limiter*) or be localized in a precise area of the vacuum vessel (*rail limiter*). Schematic examples of possible limiter configurations are reported in figure 1.8. In the case of limiter configuration, the Last Closed Flux Surface (LCFS) corresponds to the limiter solid surface and consequently impurities generated by the limiter are injected directly into the plasma region.

Divertor solution is used to solve this problem in the limiter case. In divertor configuration the outer poloidal field lines are open and directed towards toroidally symmetric regions named divertor target plates (as reported in figure 1.9). This solution performs better than the limiter op-

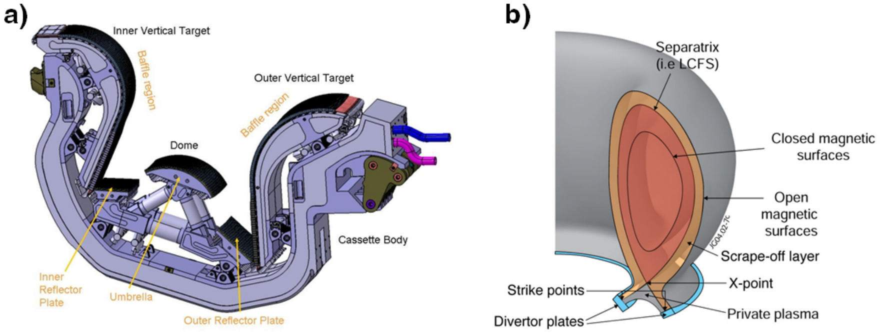

Figure 1.9: *(a) ITER divertor design [7]. (b) Geometry of a toroidal magnetic field with divertor [12].*

tion and, in particular, makes it possible to have high confinement plasma regime (H-mode) [8]. The divertor system must withstand the highest thermal loads and particle fluxes in the tokamak and for these reasons its design and the choice of materials are fundamental for guaranteeing that the tokamak will work properly. Nevertheless, it is crucial to note that it is possible to protect the divertor form these phenomena if the plasma is detached. This means that plasma has high density and low temperature in the divertor region.
Blanket (figure 1.7): has the fundamental role of protecting the tokamak's structure and coils from thermonuclear plasma (e.g. thermal loads, neutron flux, particles flux, etc.).

In the next chapter the topic of PFCs and the materials chosen to work in the tokamak environment will be investigated in more detail, paying particular attention to material modification induced by thermonuclear plasma.

2

Tungsten in magnetic fusion systems

This chapter is focused on the topic of the Plasma Facing Materials (PFMs), in particular tungsten (W). The first wall is essential in a nuclear fusion reactor since it faces directly to thermonuclear plasma. Initially, the PWIs are described in section 2.1, with particular attention paid to the thermal loads (section 2.1.1), the neutrons and particles fluxes (section 2.1.2), materials migration processes (section 2.1.3) and fuel retention and permeation into materials (section 2.1.4). In order to minimize the effects of PWIs, different materials choices were explored during nuclear fusion research. A very concise overview of relevant materials used as PFMs is given in section 2.2. In current and future tokamaks, W is widely employed as first wall material (see section 2.3). In particular, in section 2.3.1 the chosen first wall materials and design for the ITER project are discussed. To support ITER design, the ITER PFMs and concepts are tested in present-day tokamaks (section 2.3.2). In these tokamaks, it is possible to observe the W erosion, mixing and deposition process (section 2.3.3). In section 2.3.4 hydrogen (H) isotope retention in W is discussed. And, finally, in section 2.3.5, the laboratory approach in fusion research is presented.

2.1 Plasma Wall Interaction

As mentioned in section 1.5.4, PFCs have to operate in a very harsh environment. Due to the interaction between thermonuclear plasma and first wall materials, a very broad spectrum of phenomena, schematically reported in figure 2.1, can modify the pristine status of first wall materials, e.g. high thermal loads, neutron and particle fluxes, sputtering processes, element transmutation, erosion phenomena and re/co-deposition processes (see figure 2.3). Referring to figure 2.1, the simultaneous presence of thermonuclear plasma and first wall materials deeply modifies both plasma (red) and material (blue) behaviors. Furthermore, mutual effects (green) can occur. In general, these phenomena have very broad time and space scales: the length-scale can be defined from pm up to m, while the time-scale can be defined from ps to years. In the following section and in general in this thesis, the focus is on the materials.

2.1.1 Thermal loads

The power produced in a thermonuclear plasma reaches the tokamak first wall with both radiative and transport phenomena. Radiation power is uniformly deposited on total inner device surfaces. The transport, which mainly happens along magnetic fields lines, results in localized power deposition in systems designated to receive this power, i.e. the limiters and the divertor. However, particles can travel across the magnetic field lines via drift and diffusion and this leads to spreading of the heat and particle fluxes on all first wall components. In a high power tokamak, divertor and limiter materials are chosen to guarantee their functional properties in normal-operation scenarios. The behavior of materials under extremely high thermal loads strongly depends on material properties. It is important to note that the expected steady-state heat loads on the most stressed components in ITER will be about 20 MW m^{-2}. The transient edge localized modes (ELMs) can release power fluxes ≈ 1 GW m^{-2} in about 0.5 ms. Off-normal events (e.g. vertical displacement events, disruptions) are more severe, generating heat loads of up to ≈ 10 GW m^{-2}. Under such high thermal fluxes the surface temperature may exceed the melting or sublimation temperature of materials. Typically, when metals reach such extreme temperatures, they exhibit melting phenomena and in addition, before melting, surface morphology and crystal structure start to change and the surfaces become locally damaged. The molten metal can either be ejected into the plasma in the form of small droplets, that can propagate, or recrystallize, producing an area with new physical properties. On the other hand, carbon (C), which is a very important non-metal material in nuclear fusion research - as described in depth in 2.2 - sublimates instantaneously above its threshold heat load. Increasing the heat power further, it is possible to observe so-called *brittle destruction*, followed by the ejection of millimeter-size dust particles into plasma. Moreover, as discussed in section 1.5.1, tokamaks are pulsed-regime machines and, for this reason, the understanding of materials fatigue behavior must be investigated.

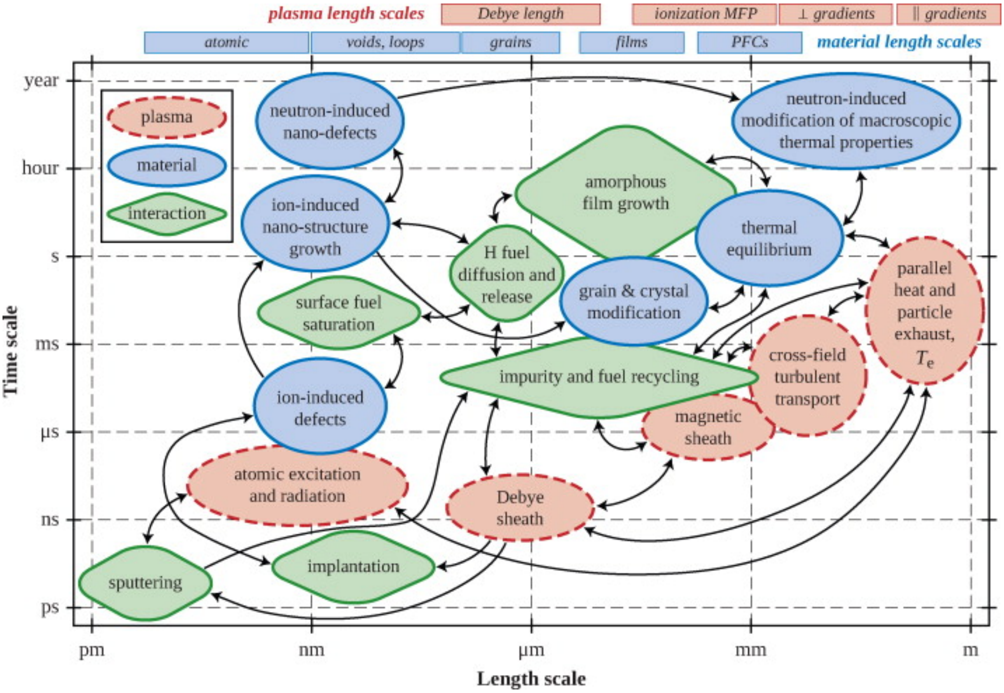

Figure 2.1: *The PMIs phase space (length and time scale) shows the processes that impact on the plasma, materials and their interaction in a magnetic fusion device [13].*

2.1.2 Neutron and particle fluxes

Working with a D-T fuel mixture, a thermonuclear fusion power plant like ITER is able to produce extremely energetic neutrons and ion fluxes, which modify materials deeply, inducing lattice defects - i.e. vacancies, interstitials, dislocations and vacancy clusters - and nuclear transmutations. In particular, an impinging neutron or ion can release part of its kinetic energy to a lattice atom, the so-called primary knock-out atom (PKA), which can cause further collisions, generating the so-called collisional cascade [14] and transmutation event [15] only if the impinging particle is a neutron. A certain number of lattice atoms, depending on neutron or ion energy, interaction geometry and other parameters, are removed from their lattice position, generating point defects (i.e. interstitials and vacancy). It is usual to measure damage induced by neutron or ion fluxes as *displacement per atom* (dpa), which statistically displays how many times one atom is knocked out from its lattice position. The foreseen neutron fluxes in ITER are approximately 10^{14} cm^{-2} s^{-1} with an energy of 14.1 MeV [16]. The neutron-induced point defects (e.g. vancancies, interstitials) can lead to various effects on the materials side, listed below:

- thermal conductivity and mechanical property losses due to crystal lattice degeneration [17];
- swelling phenomena with the creation of voids and bubbles within the material;
- nuclear transmutation of the first wall induced by neutron activation that can lead both to undesirable long-life nuclear waste and changes in the features of pristine materials [18].

The qualification of nuclear fusion grade materials requires an intense neutron source with the proper energy spectrum, which is not yet available. The *International Fusion Materials Irradiation Facility* (IFMIF) is a joint European-Japanese collaboration with the aim of creating this neutron source in order to test materials that will be used in ITER [19].

In the tokamak environment, in addition to the effects produced on materials by neutrons, there are also those produced by charged and neutral particle fluxes. In an ideal situation in which there are no other effects, the foreseen ion and neutral flux impinging on ITER divertor will be $\approx 10^{24}$ m^{-2} s^{-1} and the plasma temperature ≈ 3 eV [20] which corresponds to a D^+ impact energy of ≈ 15 eV due to the acceleration in plasma sheath potential. The estimate of blanket fluxes is more uncertain: modeling results [21] indicate that D neutral flux is in the range of $10^{19} - 10^{21}$ m^{-2} s^{-1} with typical energies $\approx 8 - 300$ eV. In these cases, the damaging effects generated by charged and neutral particles fluxes are not relevant. However, taking into account PWIs, e.g. plasma pollution, the picture drawn above can be modified deeply. In this sense, *charge exchange reactions* can happen, generating neutral particles that can penetrate deeply into the confined plasma region, where the ion temperature is high. Thus, this process transforms a fraction of neutrals with the energy of few eV into very energetic particles (up to tens of keV) that can lead to implantation processes. These energetic fluxes enhance *sputtering processes* of the first wall. Sputtering is the removal of atoms from the surface of a solid due to the impact of ions or atoms. In general it is possible to distinguish between physical and chemical sputtering.

In the case of **physical sputtering**, similarly to what happens with neutrons, these particles can generate a collision cascade within the materials.

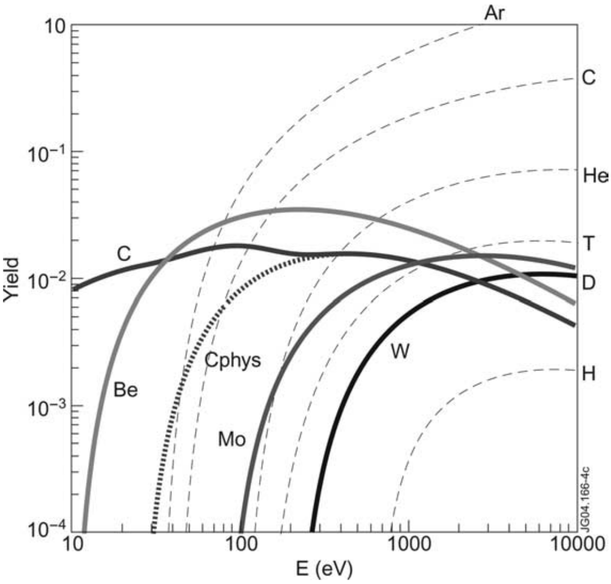

Figure 2.2: *Sputtering yields for various fusion relevant materials bombarded with D. In the case of W, physical sputtering yields for different incident ions are plotted [22].*

Physical sputtered atom is injected into plasma when the energy released to a surface atom is sufficient to overcome the surface binding energy. In this sense, the sputtering yield is proportional to the energy deposited within a nearby surface layer. Physical sputtering is thus a threshold process. As reported in figure 2.2, above threshold energy, the sputtering yield increases, reaching a maximum and then decreases at high energy because in this case the collision cascade takes place deeper into material. Other parameters influence physical sputtering, e.g. incidence angle, surface roughness and crystallographic structure.
On the other hand, **chemical sputtering** is not a threshold process (see figure 2.2), it mainly depends on chemical affinity between the species involved and it is particularly significant for low-Z materials (e.g. C and Be). The sputtering species break the material chemical bonds and induce chemical reactions that form new chemical species, e.g. the bombardment with C, oxygen (O) or nitrogen (N) of various metals induces the formation of carbides, oxides or nitrides, respectively.

2.1.3 Material migration: erosion, mixing and re/co-deposition

The processes, described above, can deeply embrittle, modify and remove material from PFCs. In particular, the embrittlement induced by neutron and ion fluxes combined with transient and cyclic thermal loads leads to both very intense sputtering phenomena, when compared with those that happen to non-damaged materials, and the ejection of melted particles in plasma.

Since tokamaks are closed systems, all eroded or ejected materials have to re/co-deposit somewhere else: this constitutes material migration and transport processes. The re-deposition may happen close to the erosion point or at remote areas. Material migration is dependent on tokamak geometry, plasma configuration, material status (ions or neutrals), etc.
In limiter configuration, as described in section 1.5, the limiters are the main sources of impurities. Due their proximity to edge plasma, limiter surfaces are deeply subjected to re-deposition processes.
In divertor configuration, material migrates from the blanket and limiters to the divertor. The atoms sputtered from the divertor plate are ionized and a large fraction is promptly re-deposited (up to 90% at the outer divertor). The remaining fraction is transported by either strong flows in the scape-off layer through the main chamber or by drifts and flows through the private flux region towards the inner divertor. Typically, it has been observed that net erosion occurs at the outer divertor, while net redeposition occurs on the inner divertor [23, 24].

The formation of deposits changes the chemical and physical properties of the surface. Typically, fuel atoms and impurities are co-deposited together with eroded wall species, forming new compounds, e.g interacting with gas contaminants (e.g. O, N), they deposit in the form of oxides and nitrides [25]. The co-deposition process is enhanced if different plasma facing materials are employed, leading to the formation of complex - and often undesirable - composition co-deposited layers. The formation of these layers on PFCs deeply modifies PMIs and the macroscopic thermo-mechanical properties of PFCs.

2.1.4 Fuel retention and permeation

As mentioned before, D and T nuclei are the fuel mixture used in fusion reactions. While D is stable and available on Earth, T is radioactive and not available naturally on Earth. For this reason, a future fusion power plant has to breed as much T as it consumes. In addition, T radioactivity is a serious nuclear hazard where T is accumulated in large quantities. For example, ITER nuclear regulations limit the total in-vessel T to 700 grams [20]. Thus, fuel retention and permeation is a challenge that must be faced in future D-T tokamaks. The first contribution to fuel retention

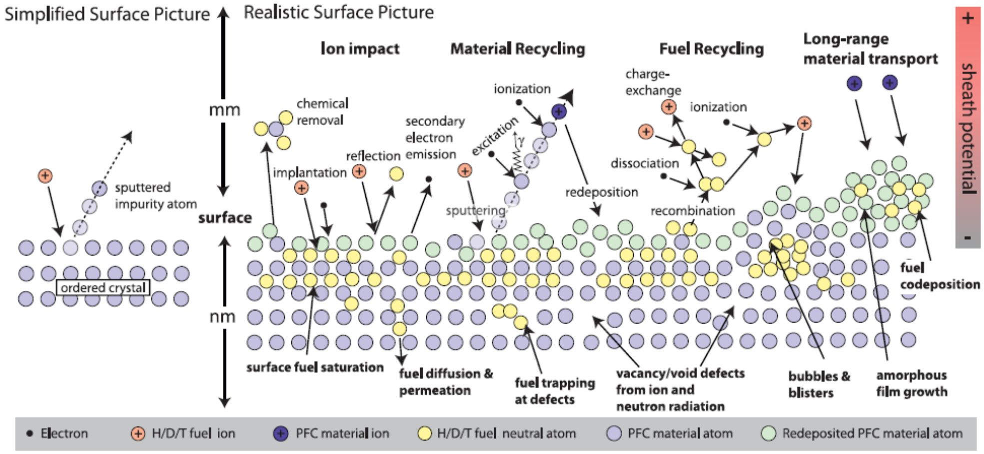

Figure 2.3: *An illustration of erosion and re/co-deposition phenomena that can occur due to PMI. The eroded PFC superficial materials (top left) can be promptly redeposited (center top) or remotely re-deposited (top right). A wide range of mechanisms that cause fuel retention is pictured in the bottom part of figure [26]*

is the energetic bombardment of fuel particles coming from plasma and their subsequent implantation in PFCs. As discussed in section 2.1.2, these particles can spread their energies from few eV up to tens of keV. After entering in PFCs, they first thermalize and then neutralize into material defects. PFCs undergo high plasma flux $\approx 10^{24}$ m^{-2} s^{-1} which results in high cumulated fluences that lead to the first mono-layers being completely saturated in D and T [27]. Once implanted, the retained fuel can permeate the materials due to thermally activated diffusion: for H and its isotopes this process starts at room temperature [28]. However, as discussed better in the following sections, the H isotope retention in co/re-deposits is much more significant than the implantation in the bulk material.

2.2 Choice of materials for the first wall

In light of what has been shown up to this point, ideal first wall materials should meet the following requirements:

- able to minimize plasma pollution and radiative power losses;
- non-reactive with plasma species to avoid chemical sputtering and the generation of volatile products;

- excellent thermo-mechanical properties (e.g good thermal conductivity, resistant to thermal shocks, etc.);
- resistant to erosion phenomena;
- low activation and short-life products when exposed to neutron irradiation;
- low retention levels of fuels.

Such a material does not exist. In magnetic fusion research, different materials have been studied. A possible classification is:

- low Z materials (C and beryllium) to minimize plasma pollution;
- high Z materials (in particular W) to minimize sputtering yields.

Carbon shows excellent thermo-mechanical properties (i.e high sublimation temperature, 3915 K, high thermal conductivity, ≈ 200 W m^{-1} K^{-1}). In particular *Carbon Fiber Composites* (CFCs) were used as the first wall material in JET and ASDEX tokamaks due their good thermal shock resistance. The main drawbacks of using C as the first wall material are the worsening of thermo-mechanical properties induced by radiation fields, the high sputtering yield, mainly due to chemical sputtering processes, and the high quantities of D and T easily retained in re/co-deposits, in the CFC porosity and in neutron induced defects [20, 29]. Despite C and CFCs being widely employed in magnetic fusion research, due to the drawbacks highlighted above, the possibility of using this material in a future magnetic fusion device has been almost entirely excluded.

Beryllium (Be) has the lowest Z=4, good thermal conductivity (≈ 190 W m^{-1} K^{-1}) and a relatively low melting temperature (1560 K) that must be taken into account during the first wall design phase. It also features lower fuel retention in comparison to C and it works as an O getter. The main drawbacks are the low melting temperature and its chemical toxicity, which makes device maintenance extremely complex (e.g. to overcome the problem in ITER a remote handling system to operate in-vessel is foreseen [30]). Despite its appealing properties, it was employed as the blanket for the first time just recently in the JET-ILW tokamak to verify that Be could really be feasible in ITER [31].

Tungsten is a high Z number material ($Z = 74$) and its crystallographic structure can be either body centered cubic (α phase, stable) or A15 cubic (β phase, metastable) [32]. It exhibits a high melting temperature (3695 K), relatively high thermal conductivity (≈ 140 W m^{-1} K^{-1}) with fragile behavior at low temperatures (420 K < T < 670 K) - low ductile-brittle transition temperature (DBTT). The W cons are high physical sputtering energy threshold - low sputtering yield - and low H isotope retention and permeation: it must be noted that, under neutron irradiation, these features can be modified significantly. For these reasons W was used in tokamaks like JET-ILW (divertor region) and ASDEX-AUG (full W machine).

2.3 Tungsten as a first wall material in tokamaks

As already mentioned in the previous sections, W has been investigated in depth as a first wall material, mainly due to its attractive properties: it has a high melting temperature, good thermal conductivity, low erosion yield and low H isotope retention and permeation. In section 2.3.1, some aspects of the first wall materials chosen for ITER, and their design, are presented. In section 2.3.2 some examples of tokamaks where PFCs are made in W are reported, with a particular focus on European supporting-ITER tokamaks as well as an overview of future supporting experiments for commercial fusion reactors. Despite its unique features, PMIs can significantly modify attractive properties of W: thermal loads can melt W or induce re-crystallization processes, ion and neutron fluxes induce defects, etc. Due to these modifications, W erosion yield increases and, thus, the eroded material can migrate and deposit on PFCs with features that differ markedly from pristine W. In particular, in section 2.3.3, some peculiar deposits, found in AUG and JET-ILW, are reported. Typically these re/co-deposited layers and particles show high levels of H isotope retention, mainly due to their complex structure, elemental composition and morphology. Furthermore, neutron fluxes dramatically increase the defect concentration in W. This high defect concentration leads to a high number of available sites where H and its isotopes can be retained. Both damaging and re/co-deposition phenomena alter pristine W H isotope retention properties, which are briefly discussed in section 2.3.4. It is evident that all these events are strictly correlated with each other. Moreover, the results coming from present-day tokamaks could be not so similar to those obtained with ITER operation conditions. For these reasons, it is fundamental to exploit the laboratory approach both to investigate systems that can mimic those that could be found in ITER and to simplify the problems decoupling the various effects. In the last section 2.3.5, an overview of research related to the H isotope retention topic in lab-scale experiments is reported.

2.3.1 ITER project and beyond

Since ITER exploits a diverted tokamak configuration, its first wall is made up by the blanket and divertor.
Blanket modules cover the inner walls of the vacuum vessel to protect structural materials and superconducting coils from the heat loads and high-energy neutrons. The neutrons are slowed down, converting their kinetic energy into heat that is removed by a water cooling system. 440 blanket modules are foreseen, and each of them is made up by a detachable first wall directly facing to the plasma and a neutron shield block. The material chosen for the first panel is Be.
Divertor; situated in the bottom part of the vacuum vessel, it minimizes plasma pollution and extracts heat through an active cooling system. It is worth noting that in the first stage design concept, the inner and outer divertor targets were made of CFCs. For cost-cutting reasons, in November 2013, the ITER Organization decided to switch to a full W divertor, already foreseen for the D-T ITER phase.
Since the first wall materials selected for ITER have never been tested in a tokamak environment, in 2011 [31] the first wall of JET - made of CFCs - was fully converted into an *Iter-Like Wall*, with Be tiles in the blanket region and a W coated divertor (see section 2.3.2 for further details).
Because ITER was designed to verify the fusion power production feasibility, it works at a low duty cycle for a limited number of years. If feasibility is proven, other machines will be built as *DEMOnstrative fusion power plants* (DEMO) linked to the electric grid [33, 34]. In table 2.1 the main tokamak parameters of the JET-ILW, ITER and European DEMO design are reported.

2.3.2 AUG, JET-ILW, WEST and DTT

Despite W being the chosen material for the ITER divertor, the first attempts to use W in a tokamak divertor were made quite recently in the ASDEX UpGrade in 1996 [36], in the JET Iter-Like Wall (JET-ILW) in 2011 [31] and this will be attempted in the Tungsten Environment in Steady-state Tokamak (WEST) in 2017 [37].
Chronologically, the first partial attempt to use a partially W coated divertor was performed in the **ASDEX UpGrade** (AUG) [36]. The results of this experiment were promising [38] and in the next year the machine

	JET-ILW	ITER	DEMO
Total Fusion Power [MW]	16.1	500	3600
Plasma major radius [m]	2.96	6.2	8.6
Toroidal Field [T]	3.45	5.3	6.9
Plasma current [MA]	4.8	15	28
Plasma Facing Materials	Be\W	Be\W	W
T breeding blanket	No	Test	$LiSiO_4$
Auxiliar heating power [MW]	38	73	270
Gain factor Q	0.7	10	13.5
Net electric power [MW]	0	0	1332

Table 2.1: *Main tokamak parameters for JET-ILW [35], ITER [7] and European DEMO design [33]*

was further upgraded, totally covering the original fine-grained graphite tiles with W coatings [39], made with different deposition techniques (see figure 2.4). Various Vapor Plasma Spray (VPS), Physical Vapor Deposition (PVD) and Chemical Vapor Deposition (CVD) techniques have been developed to produce W coatings on C-based materials with good thermo-mechanical properties. In particular, the first investigation into this topic [40] found that the best deposition technique to make W coatings for fusion applications was VPS. The first W-coated tiles installed in AUG were made with this technique but, after some plasma campaigns, crack formation on all tiles was observed [41]. For this reason, alternative

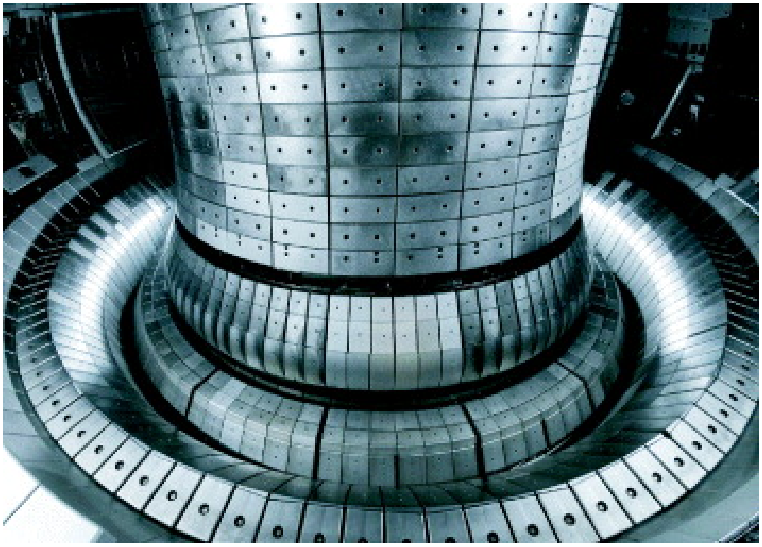

Figure 2.4: *View into fully coated W AUG [39].*

PVD and CVD techniques have been studied [42–44]. In these investigations, the Combined Magnetron Sputtering Ion Implantation (CMSII) technique has proven to be the most promising for coating C-based materials for fusion applications [45–47]. A typical cross-section view of W coating made by CMSII is reported in figure 2.5. It is possible to note that a molybdenum interlayer has been placed between the C substrate and the W film in order to accommodate mechanical stresses. As reported in 2.3.1, the ITER divertor will be built completely in actively cooled W monoblocks. In 2014, to test the performance of the solid W design, the coated W outer divertor of AUG was replaced with a solid W one that is not actively cooled [48].

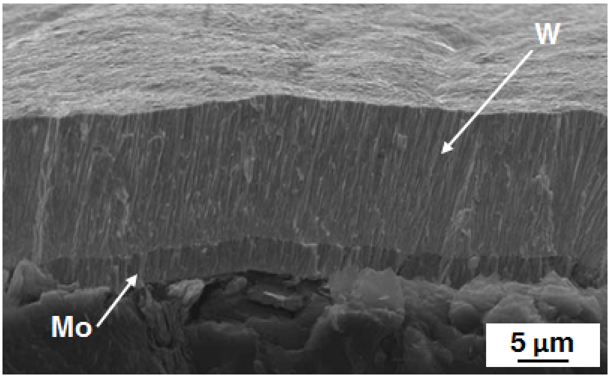

Figure 2.5: *Cross-section view of a W coating made with CMSII deposited onto the C substrate [47].*

Since the PFMs selected for ITER have never been tested in tokamak environments, in 2011 [31] the first wall of the largest European tokamak, **JET**, which was made using CFC, was fully converted into an *Iter-Like Wall*, with Be tiles in the blanket region and a full W divertor. In particular, JET-ILW goals can be synthesized as follows:

- to demonstrate that a Be and W first wall has sufficiently low retention compared with a full-C first wall [20];
- to analyze the material migration and possible alloying processes and their influences on plasma performances;
- to test the Be first wall performance when subjected to transient events (e.g. ELMS, disruptions).

The inner view of the JET-ILW is reported in figure 2.6. The divertor employs both bulk W (Load Bearing Septum Replacement Plate, LBSRP)

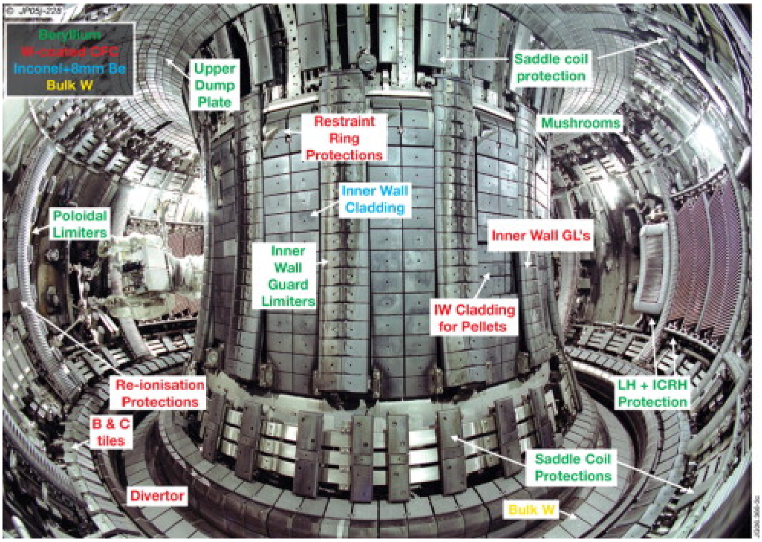

Figure 2.6: *View into JET-ILW [31].*

and W-coated CFC tiles that are also used in other tokamak regions (e.g. inner wall limiters), characterized by high heat loads. The blanket is made of both solid Be and Be-coated Inconel tiles. Thanks to the coating developments undertaken to cover AUG, CSMII was selected as the deposition technique to coat CFC tiles [49, 50]. The results, coming from the first JET-ILW campaign (2011-2012), are quite promising for future ITER operations and highlight that:

- long-term D retained in JET-ILW is ≈ 18 times lower than the D accumulated in JET-C during the 2007-2009 campaign [51, 52];
- the main mechanism for long-term retention is implantation and co-deposition of D with Be [53];
- the total deposition rate in the divertor decreased by a factor of 4-9 compared to the deposition rate in JET-C. These deposits consist mainly of Be with contaminations of C and O (5-20 at. %). The top part of the inner divertor experienced the most evident deposition processes, while the bottom part experienced the most erosion [24].

Despite what has been mentioned, AUG and JET-ILW divertors present evident differences compared to the ITER divertor.
First of all, ITER will generate the magnetic field with superconductor magnets that make it possible to achieve a quasi-steady state regime. In this regime it is possible to reach very high heat fluxes (HHFs) on PFCs.

For this reason, the ITER first wall is actively cooled. In AUG and JET-ILW, since they operate with conventional magnets, it is impossible to have a quasi-steady state regime with HHFs. In order to study this topic to support ITER, in 2013 the **WEST** Project was launched, upgrading the Tore Supra tokamak. The original divertor of the Tore Supra will be substituted with an actively cooled W divertor, with an ITER-like monoblocks design, while the other PFCs will be coated with W [54], as reported in figure 2.7. Tore Supra was selected for this project because it was a superconducting tokamak and, nowadays, it holds the record for the plasma confined in a tokamak configuration for the longest time (6.5 minutes). By exploiting this feature, it will be possible to test an ITER-like divertor in a quasi-steady state regime with HHFs. This experiment will provide indications regarding system resistance when subjected to HHFs in a tokamak environment.

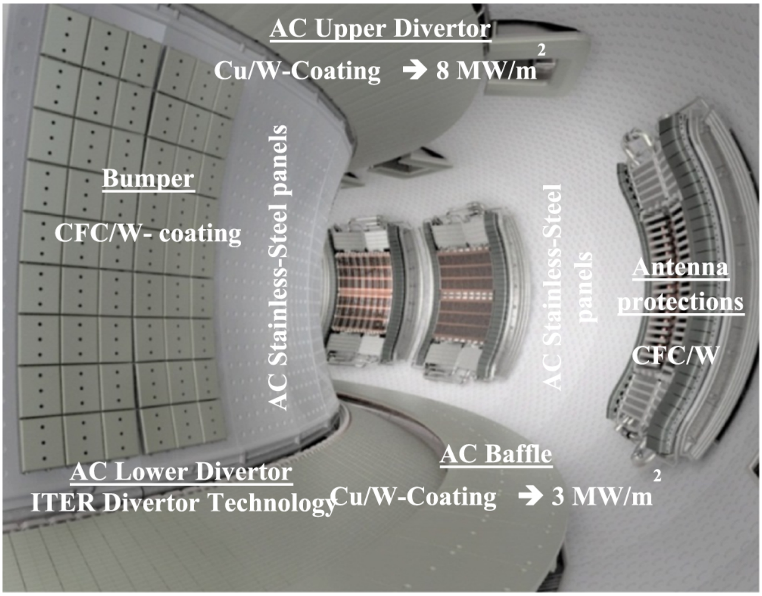

Figure 2.7: *Schematic view of the PFCs of the WEST Project. It is possible to note the active cooled (AC) system foreseen in WEST [54].*

If the fusion power production feasibility is proven by the ITER experiment, future reactors based on the DEMO design will be created. In general, DEMO will produce more power than ITER, so the 'standard' power exhaust systems used in ITER, in particular the divertor configuration, are not suitable for extrapolation to DEMO. For this reason, a specific project has been launched, to define and design a *Divertor Tokamak Test* (DTT). This tokamak should make it possible to test different divertor configurations and other possible solutions to overcome the power exhaust problems foreseen for DEMO.

2.3.3 Re/co-deposited layers in tokamaks

As mentioned in 2.1.3, the harsh tokamak environment can induce first wall erosion and, due to materials' migration and mixing phenomena, re/co-deposited layers can be found on PFMs and their presence dramatically changes materials' properties and behaviors. This is one of the most important issues in fusion devices. Despite the mechanism and condition of their formation not having been fully described and understood yet, a great deal of effort is put into the post-mortem characterization of first wall materials coming from present-day tokamaks. Thanks to these studies, it has been possible to increase what is known about the structure and elemental composition of these layers. In particular, re/co-deposited layer surveys have been carried out regularly at several tokamaks [55]. In JET-ILW, very complex layers, made up of very different materials, have been found both on divertor plates [51, 56] and on first mirrors [57]. In [56], there is a particular emphasis on the formation, the elemental composition and the structure of layers enriched in W and Be. Typically, Be deposits in the form of flakes, small spheres related to melting events and, in particular, thick Be-O-C layers around the top horizontal corner of the inner divertor that enhance the D retention diffusely. These structures also exhibit the presence of other elements, i.e. C, W, O and aluminum (figure 2.8). Figure 2.9 shows the cross-section view of a W re/co-deposited layer; it is possible to note the simultaneous presence of W crystalline and amorphous phases, the molybdenum interlayer and CFC.

The AUG machine is characterized by a full W fist wall. The collection and analysis of re/co-deposited materials in the divertor region highlights the formation of both spherical and irregularly shaped particles [58], the generation of multi-layered structures and the more common formation of thick layers [59]. Here, we focus on the discussion of the particle formation. In the AUG machine, the first wall is usually conditioned with boron (B) coatings before plasma shots: so, some B contamination was found in these particles. An example of a W spherical particle is reported in figure 2.10 with its elemental composition that, in addition to the B presence, also highlights the presence of O and iron. An example of a W irregular-shaped particle is reported in figure 2.11. To conclude, the results, obtained from

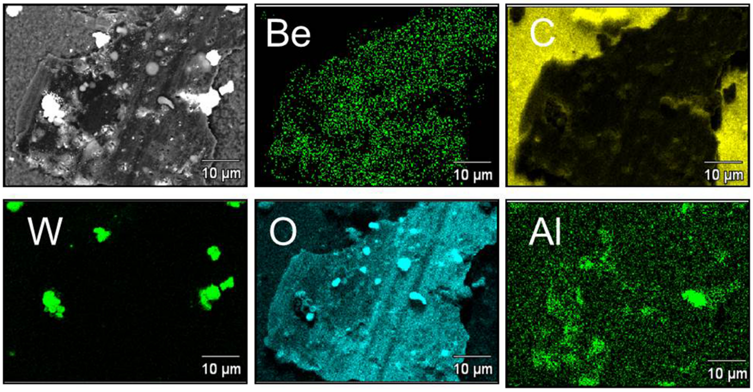

Figure 2.8: *Elemental composition of a Be flake collected after first JET-ILW campaign [56].*

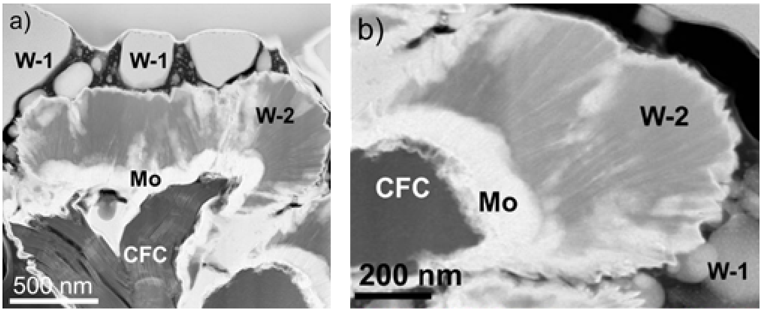

Figure 2.9: *Structure and elemental composition of W particles collected after first JET-ILW campaign. The amorphous phase of W is named W-1 while the crystalline is called phase W-2 [56].*

the test of ITER-like first mirrors in the AUG divertor region [57, 60], shows the formation of W oxides, mainly due to the O contamination present in the tokamak vacuum chamber. It is important to remember that ITER operative conditions have never been achieved in a present-day tokamak and this means that material modifications could be more severe. For this reason, all of the results obtained by analyzing the re/co-deposited layer in present-day tokamaks, can only give an estimate of the real layers that will be found in ITER.

2.3.4 Hydrogen isotope retention in W

As mentioned in section 2.1.4, the retained amount of H isotopes is directly linked with material defect density, which is $\approx 10^{-4}$ at. % for bulk W and

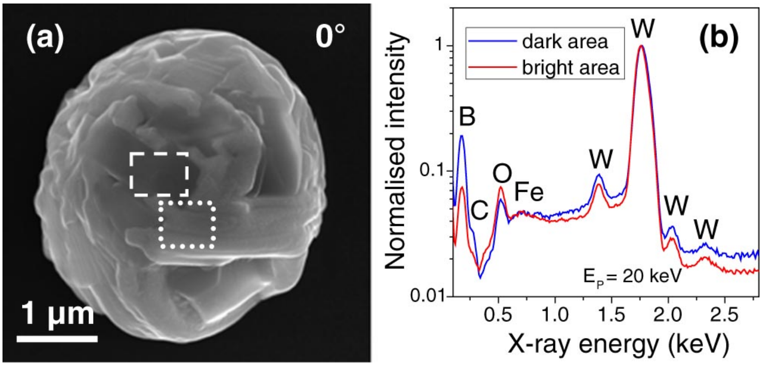

Figure 2.10: *(a) Top view SEM image of W spherical particle. (b) EDX spectra of the two marked areas. [58].*

Defect type	Trapping Energy (eV)
Trapping energy of D in W defect	
Dislocations	0.85
Grain boundary	0.85
Vacancy	1.45
Vacancy cluster	1.9-2.3
Trapping energy of D_2 *in W defect*	
Vacancy cluster	1.45

Table 2.2: *Trapping energies of D in W*

is also influenced by material morphology, structure and elemental composition. As reported in section 2.1.2, neutron and ion fluxes modify material properties and compositions, inducing lattice defects - i.e. vacancies, interstitials, dislocations and vacancy clusters - and nuclear transmutations. It is foreseen that the maximum damage achievable in the ITER divertor will be 1 dpa. Due to low interaction cross-section of neutrons generated by D-T reactions with PFMs, the induced point defects will be homogeneously distributed throughout the entire thickness of the W components. In general, vacancies and interstitials can join each other, forming vacancy clusters and dislocations. Both transmutations and damaging processes deeply alter W properties; in particular neutron-induced defects enhance H isotope retention [61]. Typically, H isotopes are trapped in vacancies, dislocations, grain boundaries and vacancy clusters or voids. Each defect type has a typical trap energy, as reported in figure 2.12 and in table 2.2. Moreover, as shown in section 2.3.3, the PMIs lead to the formation of

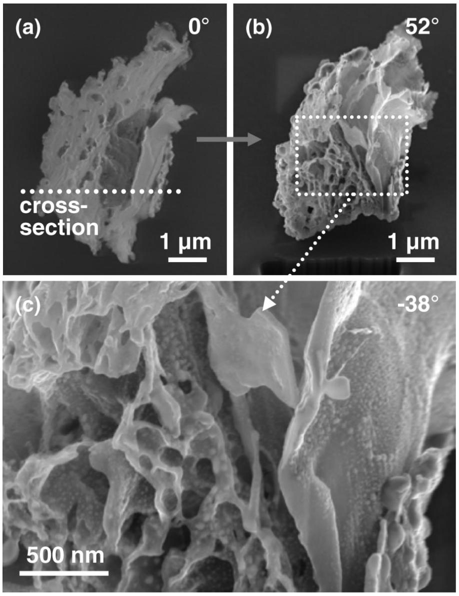

Figure 2.11: *(a) Top view SEM image of irregular-shaped W particle, (b) after cross section and (c) cross section SEM view. [58].*

re/co-deposited layers with totally different features compared with those of the pristine materials and for these reasons their retention and permeation properties could be extremely different. Therefore, it is fundamental to test ITER-like materials, both modified by PWI phenomena and re/co-deposited layers, in dedicated facilities able to reproduce ITER conditions (see section 2.3.5).

2.3.5 Lab-scale experiments

Since a 14.1 MeV neutron source is not available (see section 2.1.2), material neutron irradiation with current facilities (e.g. High Flux Isotope Reactor, U.S.A.) is time-consuming [62] and the neutron irradiation produces activated materials, protons, electrons and heavy ions can be used to introduce defects into the materials lattice [63]. Since electrons and protons have small damage rates, typically heavy ions have been used widely as a solution [27, 64–66]. Nevertheless, the damage produced by neutrons and ions remains quite different. The PKA energy is quite different: in the case of a 14.1 MeV neutron flux on W, the average PKA energy is ≈ 152 keV, while 12.3 MeV W^{+4} flux produces PKA energy ≈ 17 keV. Moreover, since neutrons have no-charge, they can penetrate deeper into W, while the damaged-layer depth generated by heavy ions is a few microns ($\approx 3\ \mu$m). For these reasons, there are a good number of projects where the different D retention behaviors in heavy ions and neutron-damaged W is investigated [67,68].

In order to assess their capability to retain D, these damaged-W samples are directly faced toward D plasmas or in the tokamak vacuum chamber during D plasma shots or linear plasma machines able to simulate a tokamak-relevant D plasma. It is worth noting that, to study H isotope retention, D is used as a model system to evaluate T retention because of T radioactivity. Then, the concentration of D is assessed either with thermal methods (e.g. *Thermal Desorption Spectroscopy*, TDS) or with nuclear analysis (e.g. *Nuclear Reaction Ananlysis*, NRA). In the previously cited works, it was shown that D retained in 1 dpa damaged W is up to 100 times higher than in the pristine W and strongly depends on W temperature during D plasma exposure.

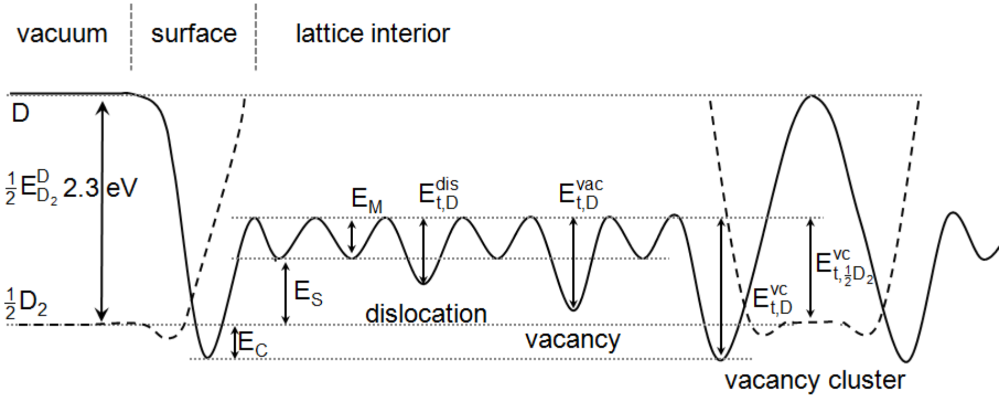

Figure 2.12: *Energy diagram of D in W. The dissociation energy of* D_2 *is reported as* $\frac{1}{2}E^{D}_{D_2}$*. Moreover, chemisorption energy (*E_C*), the enthalpy of solution (*E_S*), the migration barrier (*E_M*) and trapping energy (*E_t*) indicated*

As described in detail in section 2.3.3, re/co-deposited layers have totally different properties compared with bulk materials (e.g. mass density, structure, morphology, roughness, elemental composition, etc.). These materials have extremely high concentrations of defects that lead to a high amount of D being retained. Their structure, morphology and roughness are more complex and, moreover, they can have different elemental compositions, mainly due to mixing processes with other elements present in the tokamak environment or their interaction with reactive species (e.g. O, N). In general, the study of these systems is quite difficult because they are directly produced in the tokamak environment. At the end of each plasma campaign, the tokamak vacuum chamber is opened to collect these deposits with the aim of studying them with ex-situ techniques [56, 58]. Another time-saving approach is to mimic tokamak layers on a laboratory scale with a proper deposition technique and/or thermal annealing treatments. By using this procedure, it is possible to finely control film properties [69, 70], to theoretically have an infinite number of identical samples to use as reference samples (qualification of Laser Induced Breakdown Spectroscopy foreseen in EUROfusion Work Plans) and to create the required system to study. Some examples of this method can be found in [71–73]. As already discussed in the previous paragraph, these tokamak-proxy systems can be faced toward D plasma and then the D retained can be quantified. It was shown that in case of very disordered layers the concentration of retained D can be 20 times higher compared to that found for damaged-W [71].

Since ITER will operate in conditions never achieved before in a tokamak, the co/re-deposited layers could be different compared to those observed in present-day tokamaks. For this reason, testing as many different W and W compound films as possible is a hot topic in nuclear fusion materials science to increase knowledge about the relationship between film features and amount of D retained.

This thesis wants to provide an experimental investigation, at the laboratory-scale, mainly focused on mimicking the tokamak's deposits with a proper deposition technique and on the quantification of D retained in these layers after their exposure to a D plasma. The work methodology and the specific goals pursued in this thesis will be discussed in detail in chapter 3. Once the thesis aims have been defined, the structure will be described.

3

Thesis goals and methods

THIS chapter presents the specific goals of this thesis and illustrates the research methodology used to achieve them. The plasma-facing materials modifications induced by thermonuclear plasma are manifold and extremely complex, as explained in chapter 2. Typically, these layers exhibit properties (i.e. morphology, structure, elemental composition and stoichiometry) very different from the those of first wall pristine materials. Nowadays, due to the limited number of present-day working tokamaks, tokamak layers that are available to be studied are not sufficient in order to properly comprehend the behavior of these modified materials. Moreover, these layers are produced in machines where the operational conditions could be very different form ITER working conditions. To overcome these issues and to further support this topic, which is of great interest and timely, it is fundamental to employ lab-scale approaches both to increase the number of tokamak-like layers tested in tokamak-relevant conditions and to produce 'new-design' layers that could be present on the first wall of ITER. In section 3.1, the goals of this thesis and the experimental strategies adopted to achieve them are presented. To have fine film property control, the Pulsed Laser Deposition (PLD) technique is employed to produce these proxy-tokamak layers. Methodological and technical details regarding PLD are given in section 3.2.1. The characterization techniques are presented in section 3.3. Linear divertor-like plasma generators are exploited in this thesis to test materials in tokamak-relevant conditions (see section 3.4), while the techniques used to assess H isotope retention are explained in section 3.5.

3.1 Specific goals of the thesis

As described in chapter 1, tokamak is the reference design to achieve fusion energy production by exploiting the magnetic confinement of thermonuclear plasma. In such complex machines, as reported in chapter 2, PMIs deeply modify both plasma status and first wall material properties. In particular, PFMs have to face a very extreme environment. Under these conditions, different phenomena can be observed, e.g.material damage, erosion, re/co-deposition events (see 2.1). Since ITER should prove the feasibility of nuclear fusion energy production, it reaches operative conditions never achieved in present-day tokamaks. For this reason, the re/co-deposited layers, which could form on PFMs in ITER, are little-known and unpredictable. Typically, re/co-deposited materials exhibit very different behaviors: in particular, their resistance when faced toward tokamak plasma is lower and H isotope retention is enhanced. The main goal of this thesis is to study the properties of non-conventional W-based layers and their behaviors when faced toward tokamak-like plasma (i.e. plasma resistance and H isotope retention capability). In particular, to achieve these aims, a widespread experimental campaign has been developed. The block diagram, reported in figure 3.1, schematically describes the con-

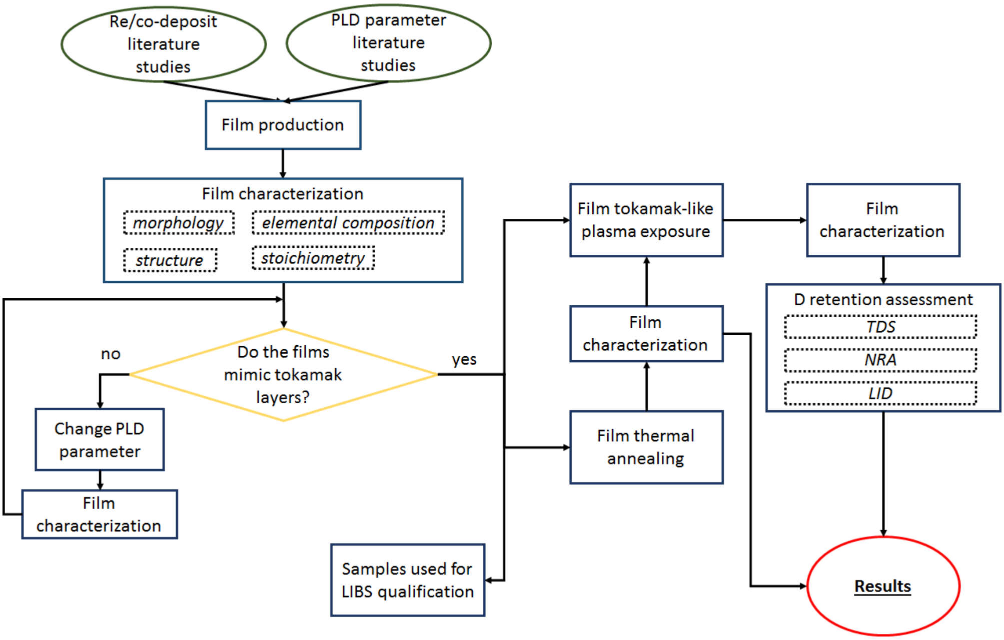

Figure 3.1: *Block diagram of activities developed during this project*

ceptual scheme adopted throughout this project. It was fundamental to study the literature regarding re/co-deposited layers in present-day tokamaks and the methodologies to control films properties via PLD. Then, the produced films were fully characterized, addressing their morphology, elemental composition, structure and stoichiometry to understand if they could mimic tokamak layers. The deposition parameters were changed until the desired film properties were found. These tokamak-like layers were used for different purposes: some films were provided as reference samples for Laser Induced Breakdown Spectroscopy (LIBS). Nowadays, LIBS is being investigated in depth to determine if it could be employed in future tokamaks for on-line monitoring of PFM status during operations [74]. Moreover, the more fusion-relevant coatings produced by PLD have been thermally annealed in vacuum at different temperatures to understand the modifications induced by possible thermal loads in this metastable system. Both thermally annealed and as-deposited films have been exposed to different divertor-like plasmas to investigate the modifications induced by plasma and the amount of H isotopes (in particular D) retained in these films. To conclude, the main actives carried out during this thesis can be summarized as follow:

- production by proper tunable deposition technique and thermal annealing treatments, on a laboratory-scale, of W- and W compound-relevant coatings that could resemble bulk W after damage in the harsh tokamak environment and of W and W compound layers that could be formed after co/re-deposition phenomena;
- characterization of these proxy systems via suitable analysis techniques, addressing morphology, structure and elemental composition;
- exposure of these tailored films to divertor-like relevant plasmas in order to understand the relationship between coating properties (structure, morphology, elemental composition and stoichiometry), H isotope permeation and retention processes and the modifications induced by plasma itself.

The first and the second tasks have mainly been done at the Micro- and Nanostructured Materials Lab (NanoLab) of the Politecnico di Milano. The film production is carried out by exploiting the great versatility and the unique features of PLD (for an extensive description see section 3.2.1), which makes it possible to produce various material films with precise control over their structure, morphology and stoichiometry by varying the main process parameters like laser fluence, background gases and their pressure and target composition. By finely tuning these parameters it is possible to produce films with the desired properties at the nanoscale. Moreover, to better mimic tokamak layers, some post-deposition treatments are performed (e.g. thermal annealing treatments, see section 3.2.2) both to simulate typical divertor temperatures to which these layers can be subjected and to have an extra degree of freedom to control film properties. Coatings structure, morphology, elemental composition and stoichiometry have been characterized by different analysis techniques, described in detail in section 3.3. It is important to note that some of these films have been used as reference samples to qualify LIBS within the EUROfusion work plans.

The third task was completed thanks to the various international collaborations, that were also developed in the framework of EUROfusion work plans (Work Package Plasma Facing Components, WP-PFC). In particular, W and W compound films are tested in different ITER-relevant linear plasma generators (see section 3.4) under different plasma scenarios in order to understand films' D retention properties and their post-exposure modifications. In particular, two collaborations were widely exploited: the first with the *DIFFER* institute (the Netherlands) and the second with the *Forschungszentrum Jülich* (Germany). Post-exposure modifications were investigated at NanoLab. On the other hand, D retention measurements were assessed by using the international collaborations. In particular, in this thesis, Nuclear Reaction Analysis and Thermal Desorption Spectroscopy were used (see sections 3.5.1 and 3.5.2).

3.2 Film production

As already mentioned, film production was carried out by controlling PLD process parameters. PLD is described in section 3.2.1. In section 3.2.2, the thermal annealing apparatus used to better control film properties is presented.

3.2.1 Pulsed Laser Deposition

PLD is a Physical Vapour Deposition (PVD) technique, where the materials to be deposited are brought into the vapor phase by means of a physical process, in the case of PLD, laser ablation. As reported in figure 3.2, the typical PLD scheme foresees a solid target hit by laser pulses inside a vacuum chamber. After the interaction with a laser pulse, the target surface can be non-thermally ablated. The ablated materials

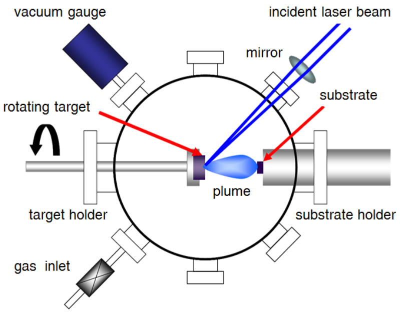

Figure 3.2: *PLD scheme.*

(molecules, atoms, ions, electrons and small aggregates) expand in the vacuum chamber, assuming the typical *plume* shape. After their expansion, the ablated materials are collected onto a proper substrate. The plume expansion can occur either in vacuum or in the presence of a background gas atmosphere, which can be chemically inert (e.g. He, Ar) or reactive (e.g. N_2, O_2). Laser-target interaction involves complex thermal and non-thermal processes, each characterized by a particular time scale. The excited populations relax towards equilibrium via electron-electron (1-100 fs) and electron-phonon (few ps) collisions. The laser used in this work has a ns pulse duration. In this regime, electron-lattice relaxation is so fast that the system can be described well with a single temperature distribution. The laser pulse penetration $\mathrm{l_a}$ in a material is:

$$\mathrm{l_a} = \frac{1}{\mu} \tag{3.1}$$

where μ is the material absorption coefficient that depends on the laser wavelength. The characteristic heat diffusion length $\mathrm{l_t}$ for a homogeneous and isotropic material is:

$$\mathrm{l_t} = \sqrt{\mathrm{D}\,\tau_\mathrm{L}} \tag{3.2}$$

where, D is the diffusion coefficient and τ_L is the pulse duration. If $\mathrm{l_a} > \mathrm{l_t}$, only the layer of thickness $\mathrm{l_a}$ experiences laser heating. Otherwise, if $\mathrm{l_a} < \mathrm{l_t}$, the absorbed energy is transported over $\mathrm{l_t}$ by heat diffusion mechanisms.

If the temperature rise due to laser heating is sufficient, laser ablation happens. Therefore, it is possible to define a threshold areal energy density (known as *fluence*) above which ablation occurs, depending on target properties and laser parameters. Since the complex mechanisms in laser-target interaction, different regions of target can reach different temperature - e.g. if in a region, the temperature ranges between the melting and

vaporization temperature, liquid droplets can be ejected due to the recoil pressure. Typically, the droplet production decreases film quality and is one of the major drawbacks of the PLD technique.
The ablated material is a weakly ionized plasma. The plasma plume is highly oriented perpendicular to the target, and its shape and expansion dynamic are strongly influenced by the presence of a background gas. Plume species lose their energy due to the collision with background gas particles. Then, as the gas pressure increases, plume species are slowed down more efficiently. A pictorial view of different plume confinement regimes, as a function of the background pressure, is reported in figure 3.3. Three different pressure regimes are detachable, each of which is characterized by a specific plume behavior [75]:

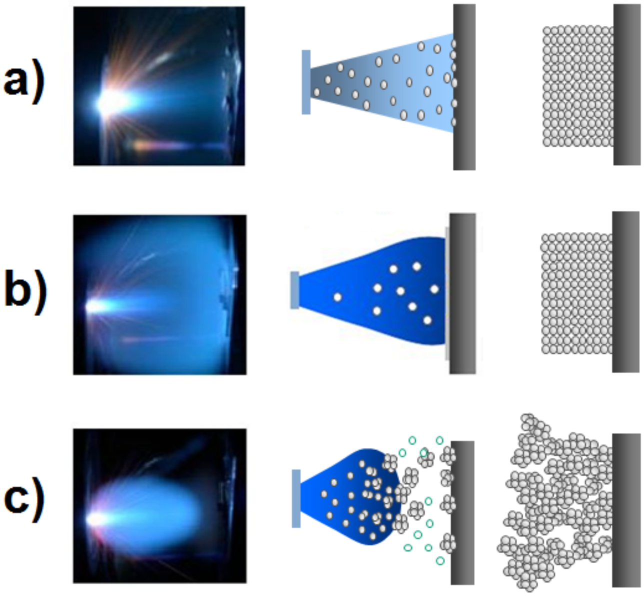

Figure 3.3: *Ablation plumes of W in vacuum (a), at low He pressure (b) and at high He pressure (c).*

a) a low pressure regime without plume confinement (figure 3.3a);

b) a transition regime with the formation of a shock-wave front (figure 3.3b);

c) a high pressure regime in which the plume is clearly confined (figure 3.3c).

In addition to confinement effects, chemically reactive gases (e.g O_2, N_2) can be used to induce chemical reactions within the ablated material. Film morphology is strongly correlated with plume confinement and collisional processes. In the case of low deposition pressure, an atom-by-atom growth mechanism is favored, which leads to compact films. On the other hand, plume confinement enhances cluster formation. Calibrating cluster dimensions and their kinetic energy, it is possible to obtain different film morphologies, from hierarchical to porous.

As reported preliminarily, film properties depend on laser parameters, like wavelength and fluence. Shorter wavelengths give shorter l_a, bringing the system to a higher temperature. Higher fluence regimes lead to higher ablation rates and particle kinetic energies, but also more ejection of particulate. The properties of the deposited films depend not only on background gas and laser fluence, but also on other process parameters: laser pulse duration and spot size, repetition rate, chemical composition and structure of target and substrate, target to substrate distance, substrate temperature and geometry.

Having the possibility to control such a large number of parameters makes it possible to have good film property control. On the other hand, the optimization of all these parameters is time-consuming and for this reason PLD is mainly employed in the field of scientific research. Nevertheless, if compared with other deposition techniques, PLD is attractive because it makes it possible to finely tailor film properties at the micro- and nanoscale.

The literature about PLD is vast and covers different specific topics; therefore the brief overview given here is not exhaustive. The reader is referred to the many dedicated textbooks (for example [76, 77]) for a complete discussion about this topic. The PLD apparatus used in this thesis is presented in the following section.

PLD @ Nanolab for fusion research

PLDs of films that can be proxies of co/re-deposited layers, found in tokamak environments, is a novel topic developed by Nanolab beginning in 2011. It was demonstrated that by properly selecting process parameters it is possible to finely control film features [69].

In particular, the PLD equipment used in this thesis consists of a solid state laser, optics to direct the laser beam to the target, a high vacuum chamber, a pumping system and a set of remote-controlled motors for the motion of the target and the substrate (see figure 3.4).

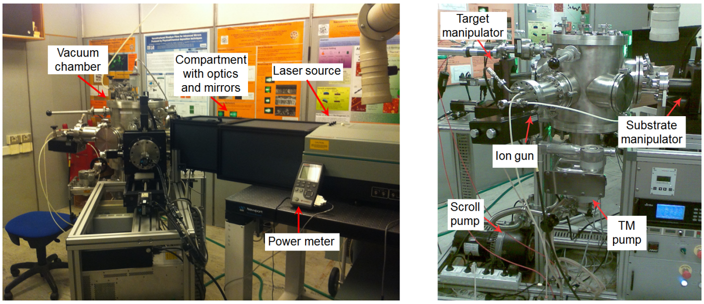

Figure 3.4: *Photographs of PLD apparature at Nanolab.*

The laser source is a Q-switched Nd:YAG (Neodymium-doped Yttrium Aluminum Garnet) Continuum Powerlite II 8010 laser, which generates ns pulses (7 ns) at the fundamental wavelength $\lambda = 1064$ nm (IR). The maximum repetition rate is 10 Hz. Pulse energy is measured by an external power meter. Modifying the delay time between pulse generation and the maximum efficiency of the amplification module, it is possible to range pulse energy between 350 mJ and 1800 mJ. Non-linear crystals make it possible to frequency-double and frequency-quadruple the fundamental wavelength. Then, it is possible to obtain pulse wavelengths $\lambda = 532$ nm (Visible, Vis; maximum energy 800 mJ) and $\lambda = 266$ nm (Ultra Violet, UV; maximum energy 160 mJ). As generated, the laser beam spot has a circular profile with a diameter of 9 mm. The laser beam impinges on the target at an angle of 45°, so its projection is elliptical. The beam can be focused by plano-convex lenses. The fluence onto target is the ratio between pulse energy and laser spot area onto target.

The high vacuum chamber is a stainless steel cylinder. It is equipped with different components: a pumping system, laser window, target and substrate holder, diagnostic instruments, a gas inlet and other equipment (e.g ion gun). Viton o-rings are used to guarantee the vacuum seal. The pumping system is made up of a primary scroll pump and a TurboMolecular Pump (TMP). The scroll pump works in a viscous flow regime and makes it possible to reach a pressure of about 10 Pa. TMP works in molecular flow conditions and can bring the system to the nominal pressure of 10^{-4} Pa. Pressure is measured by a capacitance gauge (operational range $10^{-1} - 10^{3}$ Pa) and by a full range gauge (Pirani and Bayard-Alpert sensor combination, operational range $10^{-4} - 10^{5}$ Pa). The gas inlet is controlled by a mass-flow meters system. A PID controller is able to regulate the gas mass flow in order to maintain the desired pressure (from 10^{-1} up to 10^{2} Pa). The target and substrate holder are reported in figure 3.5. The locked

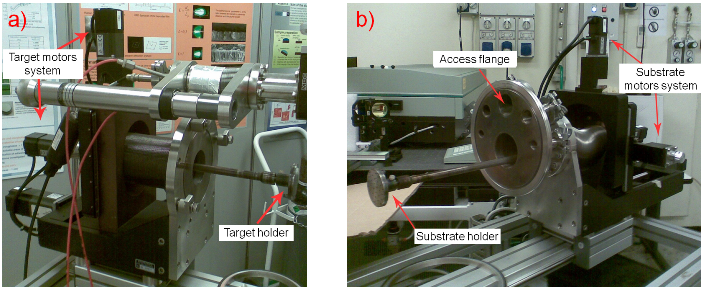

Figure 3.5: *Photographs of the target (a) and substrate (b) manipulators.*

manipulators make it possible to translate both in vertical and horizontal directions and to rotate around their axis. These motions are commanded by software-controlled stepper motors. Dedicated software makes it possible to control target and substrate motion during the deposition process: in particular, target movement makes it possible to obtain a spiral-like motion of the laser beam that ensures uniform ablation. The substrate manipulator makes it possible to manually shift the substrate holder in the horizontal direction. Combining the substrate holder shift with its rotation, it is possible to achieve film planarity over areas of several cm^2.

3.2.2 Thermal annealing apparatus

The thermal annealing apparatus consists of a high vacuum chamber, a heater stage and a pumping system.

The high vacuum chamber is a stainless steel sphere and it is equipped with different components: a pumping system, view ports, diagnostic instruments and a gas inlet. Copper o-rings are used to guarantee the vacuum seal. The pumping system is made up of a primary rotative pump and a TMP. The achievable nominal pressure is about 10^{-6} Pa. The pressure is measured by a capacitance gauge (operational range $10^2 - 10^5$ Pa) and by a Bayard-Alpert gauge (operational range $10^{-2} - 10^{-8}$ Pa). The gas inlet ensures that it is possible to force a gas flow during annealing procedures both to have the desired atmosphere and to coerce the cooling processes.

The heater stage, its power supply and its controller are provided by Tectra, and the heater stage is reported in figure 3.6a. The heating element, commercially called BORALECTRIIC® (see figure 3.6b) is made of pyrolytic Boron Nitride (pBN, the dielectric ceramic material) and pyrolytic graphite (pG, the electrical conductor). By flowing an electrical current in graphite contact and exploiting the Joule effect, it is possible to bring the system to the desired temperature, measured by a C thermocouple, using a proper controlling system. The controlling system consists of a standard PID controller. The molybdenum shield installed around the heating element makes it possible to reduce the power that is radiated, keeping the other components safe and ensuring a uniform temperature distribution. This system can reach extremely high temperatures, of about 2000 K, with heating ramps up to 100 K s^{-1}.

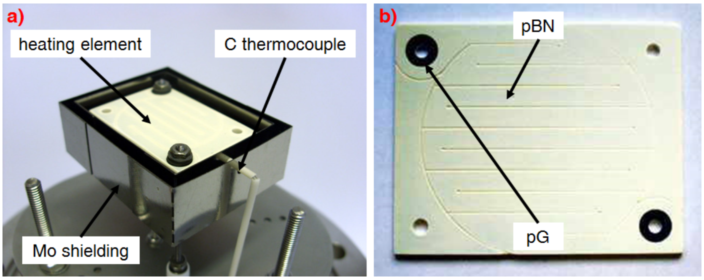

Figure 3.6: *Photographs of the heater stage (a) and the heating element (b).*

3.3 Material characterization techniques

To satisfactorily pursue the aims described in section 3.1, it is mandatory to study and characterize the materials employed. It is possible to assess these properties by exploiting different characterization techniques. The most important material properties, as far as the aims of this work are concerned, are reported below, together with the characterization techniques used:

- morphology (SEM);
- composition (EDXS);
- chemical nature (Raman spectroscopy, EDXS);
- crystalline structure (XRD and Raman spectroscopy, electrical resistivity measurements).

The characterization techniques, that are used extensively in this thesis, are described in the following sections. Scanning Electron Microscopy (SEM) makes it possible to obtain information about sample morphology at the micro- and nano-scale (see section 3.3.1). Section 3.3.1 also describes the Energy-Dispersive X-ray Spectroscopy (EDXS) technique that enables the quantification of samples' elemental composition. Raman spectroscopy (section 3.3.2) has been used to determine chemical and structural properties of the deposited materials. X-Ray Diffraction spectroscopy (XRD) has been employed to study the crystalline structure of samples (see section 3.3.3). Electrical resistivity measurements (section 3.3.4) have been used to study the structural modifications induced by thermal annealing of samples.

3.3.1 Scanning Electron Microscopy and Energy-Dispersive X-ray Spectroscopy

In SEM, an electron beam is focused on a fine probe that scans the surface of the samples that are to be analyzed. The interaction between the the specimen and the electron probe (*primary electrons*) produces *backscatterd electrons* (BSE), *secondary electrons* (SE) and X-rays. BSE and SE provide information about sample morphology, while X-rays provide information about sample composition.

BSE are produced by elastic scattering events between primary electrons and atomic nuclei. Due to the big difference between electrons and nuclei masses, electrons lose little energy in these events. Since backscattering cross section is proportional to Z^2, the higher the specimen atomic number is, the more BSE are produced. For this reason, BSE can also provide qualitative information about samples composition.

Primary electrons can interact with specimens, generating inelastic collisions with electrons bounds in atoms. If the energy transferred is sufficient, the SE are kicked out. Generally, SE have a kinetic energy that is less than 50 eV and to escape the samples and reach the detector they must have energy higher than the material work function. For this reason, typically, only the SE generated in first nm of material can be detected.

After inelastic scattering, atoms are in excited states. Typically, they relax by emitting either an Auger electron or a characteristic X-ray. In EDXS, the X-rays emitted are collected and analyzed thanks to a proper detector, identifying the spectral lines corresponding to the elements that are present in the probed region. Thanks to dedicated software, it is possible to perform quantitative composition analysis of the sample. The primary electrons can travel deep into the sample before exciting X-ray emission. This distance is a function of the accelerating potential given to the primary electron beam and the material properties (e.g. Z, mass density).

The SEM used to do this work is a high resolution Field Emission-SEM Zeiss Supra 40 based on the Gemini column, equipped with an Oxford EDXS spectrometer. The accelerating voltage ranges from 1 kV up to 30 kV. The sample holder is connected with five software-controlled motors (x, y, x, rotation and tilt). The EDXS detector is a solid-state silicon lithium detector protected by a Be window with an energy resolution of about 10 eV. Quantitative composition analysis is automatically done with *INCA Analysis* software, but not taking into account possible alterations due to the surface roughness and morphology. All EDXS measurements hereby reported were repeated 3 times on each measurement point in order to have a better statistics.

3.3.2 Raman spectroscopy

Raman scattering is the inelastic scattering of a monochromatic light (coming from a visible laser source) due to the excitation of vibrational modes in crystal or molecules. Due to the inelastic scattering, the energy of the laser photons varies: the energy shift gives information about vibrational modes active in material analyzed.

In a Raman spectroscopy set-up, a sample is illuminated with a laser beam. The light coming from the illuminated spot is sent through a monochromator. The scatter radiation that has not changed its wavelength is filtered out, while the rest of the collected light is spectroscopically analyzed. A Raman spectrum consists of a plot of the scattered light intensity versus the Raman shift, defined as the difference between the scattered radiation wavenumber (cm^{-1}) and the laser source wavenumber.

The presence of a peak is related to a certain lattice vibration mode that is coupled with the electromagnetic field generated by the laser source. Not all the vibrational modes can couple with the electromagnetic field: selection rules indicate which modes are Raman-active. Generally, pure metals do not have any Raman-active modes. Therefore, Raman spectroscopy provides information about the crystalline structure of a specimen and its impurities or oxidation degree.

Here, a Renishaw In-Via Raman spectrometer has been used. The laser source wavelength is 514.5 nm. Spectra have been acquired by a 1800 greeds/mm grating, a super-notch filter (cutoff at 100 cm^{-1}) and a Peltier-cooled CCD camera, allowing a spectral resolution of about 3 cm^{-1}. Laser power was set below 1 mW to avoid thermal modifications of the sample.

3.3.3 X-Ray Diffraction spectroscopy

XRD is a powerful non-destructive technique that enables the identification of the different phases present in the analyzed specimen, as well as, its structural properties (e.g. crystallite size, preferential growth orientation). The X-rays are diffracted by the crystalline planes of the material. Constructive interference occurs when the path length difference between X-ray beams scattered from successive crystal planes is an integer of the incident radiation wavelength λ. This is the statement of Bragg's law:

$$\mathrm{n}\lambda = 2\mathrm{d}_{\mathrm{hkl}} \sin\theta_{\mathrm{hkl}} \tag{3.3}$$

where $\mathrm{d}_{\mathrm{hkl}}$ is the distance between crystal planes with Miller indexes (hkl) and θ_{hkl} is the angle between these planes and the incident X-ray beam. Bragg's law is reported in figure 3.7. From equation 3.3 it is clear that the detector of the difracted X-rays must be placed at $2\theta_{\mathrm{hkl}}$ with regard to the direction of the incident beam.

Here, XRD spectra have been acquired by a Panalytical X'Pert Pro X-ray diffractometer. This instrument uses monchromatic copper Kα radiation ($\lambda = 1.54$ Å) and works in the Bragg-Bretano $\theta/2\theta$ configuration. In this system, the X-ray source and the detector rotate with the same velocity in opposite directions and the analyzed specimen is fixed onto a holder. In this way, Bragg's law is always satisfied and the investigation of different inter-planar distances is therefore possible by changing θ.

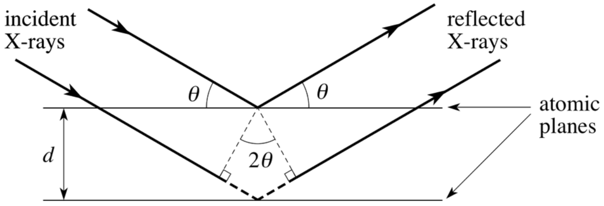

Figure 3.7: *Schematic view of Bragg's law.*

3.3.4 Electrical resistivity measurements

Micro- and nanostructured materials have properties that are strongly dependent on their morphology, structure and composition. Moreover, these materials can be in a metastable state that can easily be changed by applying little perturbations (e.g thermal loads).

In general, electrical resistivity ρ is a good means for monitoring these possible changes, e.g. if material crystalline order gets worse or impurities within the films increase, the ρ rises and vice versa. Therefore, it is evident that ρ could be a good probe in order to have a general idea about the overall state of the system.

In particular, in this thesis, in-plane electrical properties are measured in 4-point probe (for resistivities up to 100 Ω cm) configuration with a Keithley K2400 Source/Measure Unit as a current generator (form 100 nA up to 10 mA) and an Agilent 34970A voltage meter (6 $\frac{1}{2}$ digits, sensitivity 1 nV) using the so-called *van der Pauw method* [78]. A homemade analog commutator is used to exchange the current-carrying and voltage-measuring electrodes, which are constituted of spring-loaded gold pogo pins mounted on an Ecopia PCB board.

3.4 Linear Plasma Generators

In order to test how micro- and nanostructured materials with different features behave when faced to a tokamak-relevant plasma, some selected samples with the desired properties have been exposed to linear plasma generators able to produce plasma conditions similar to those expected in tokamaks like ITER. In general, samples were exposed to D plasma. In this project, three different linear plasma generators were used: Pilot-PSI [79] and MAGNUM-PSI [80] at FOM-DIFFER, and PSI-2 [81] at Jülich.

Pilot-PSI is characterized by high density ($\approx 10^{24}$ m^{-3}) and low temperature ($\approx$ 1 eV) H-based plasmas. Figure 3.8 shows the experimental setup of Pilot-PSI with the location of the diagnostics to measure the surface samples' temperature (infra-red camera) and the local plasma conditions (Thomson scattering).

The plasma is produced with an arc cascade source and then expands out of the high pressure source into a cylindrical vacuum vessel. The vacuum chamber is surrounded by oil-cooled coils that produce an axial magnetic field of 0.4-1.7 T. Due to the cooling requirement of the coils, Pilot-PSI works in a pulsed regime. The target is installed perpendicular to the plasma beam and is clamped onto a copper heat sink that is water-cooled. To maximize the thermal contact, a grafoil sheet is added between the sample and the heat sink. The targets' potential can be floating, grounded or controlled by an external power supply. Pilot-PSI was originally made as the forerunner experiment to MAGNUM-PSI.

In its original design, MAGNUM-PSI is equipped with superconducting coils to perform continuous exposures. Then, the plasma in MAGNUM-

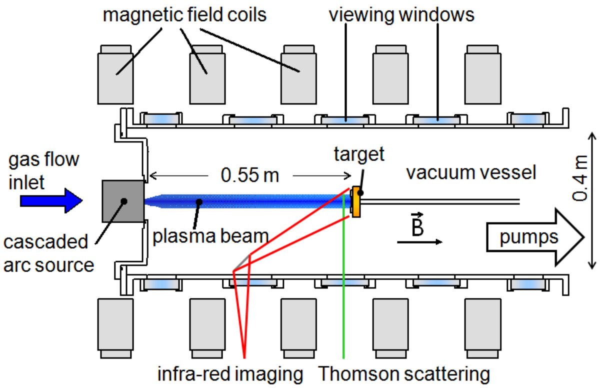

Figure 3.8: *Schematic drawing of Pilot-PSI plasma generator.*

PSI is magnetized, steady-state (B = 3T) and characterized by high particle flux ($\approx 10^{25}$ m^{-2} s^{-1}). Unfortunately, due to technical problems, during exposures performed in this thesis, super-magnetic coils were not available and the experimental plasma conditions obtained were similar to those of Pilot-PSI.

The linear plasma generator PSI-2 operates in a steady-state regime. The stationary plasma is produced between a cylindrical, heated cathode made from LaB_6 and a hollow anode made from Mo. The plasma that is generated can expand in a proper vacuum chamber and is confined by an axial magnetic field of 0.1 T produced by copper coils. The particle flux density can reach up to $\approx 10^{23}$ m^{-2} s^{-1}, which is 10 times lower than the flux expected in the ITER divertor region. Nevertheless, by exploiting its continuous operation mode, it is possible to achieve ITER-relevant fluence on the samples exposed. Moreover, the target is heatable up to temperatures above 1000°C and the temperature is constant during the entire exposure-time. Figure 3.9 reports a photograph of PSI-2. To conclude, Pilot-PSI and MAGNUM-PSI are quite similar devices that produce plasma shots with a duration of a few seconds and high fluxes ($\approx 10^{24}$ m^{-2} s^{-1}). Originally, as mentioned above, MAGNUM-PSI should have been equipped with super-conductive magnets that would have allowed it to work at high plasma flux in a steady state. However, due to technical problems, in these experiments MAGNUM-PSI was used in a configuration that is similar to that of PILOT. On the other hand, PSI-2 regularly works in steady state, generating lower plasma flux compared to MAGNUM-PSI and Pilot-PSI but with similar properties (e.g. low temperature plasma, plasma fluence, sample temperature during exposure). By exploiting this difference, it has been possible to study the

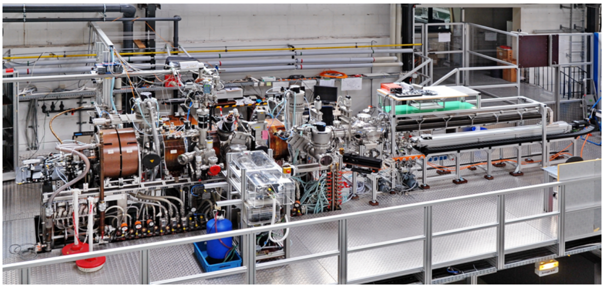

Figure 3.9: *Photograph of PSI-2 plasma generator.*

role of plasma flux, keeping the other parameters constant. Moreover, PSI-2 is a more flexible device, which has made it possible to also perform in-situ measurements regarding the prompt out-gassing properties of the tested coatings.

3.5 Deuterium retention analysis techniques

Once exposed to the D plasma, all samples were fully characterized: morphological, structural and compositional changes were assessed with the material characterization techniques described in section 3.3. Moreover, as already discussed in section 2.3.4, materials can retain a certain amount of D after their exposures. In order to understand the connection between materials' properties and D retention phenomena, it is mandatory to be able to measure the total D amount loaded in samples. Two different techniques have been used in this thesis to asses the total D retained: Thermal Desorption Spectroscopy (TDS, see section 3.5.1) and Nuclear Reaction Analysis (NRA), see section 3.5.2):

3.5.1 Thermal Desorption Spectroscopy

TDS, also known as temperature programmed desorption, measures the desorption of molecules from a material during a heating cycle. The basics of this method are reported in [82]. Summarizing, a sample is placed in a vacuum chamber and heated with a linear temperature ramp. When the internal thermal energy increases, the D atoms can overcome their trap energies and diffuse to the surface, where they recombine and finally desorb as molecules. The released rate is monitored by a mass spectrometer to construct a thermal desorption spectrum. This technique requires calibrations to extract the number of molecules released from the current mass spectrometer signal: in particular, calibrated D_2 and H_2 leaks are used to determine instrument sensitivity. TDS makes it possible to obtain data about the total amount of D retained in the exposed specimen without depth resolution: it is not possible to discriminate the D released by the coating and by the substrate. Nevertheless, this technique provides information about the trap energies where D is retained. Theoretically, if opportunely calibrated, TDS is able to record all gases released by the sample with extremely high resolution (depending on mass quadrupole resolution); however, this technique is quite sensitive and can be affected by different error sources, e.g. leakage in the vacuum chamber, imperfect linearity of the temperature ramp, problems with the calibration of some compounds (e.g heavy waters).

3.5.2 Nuclear Reaction Analysis

NRA is a non-destructive method for determining light elements in a heavy material. The local deuterium concentration was measured using the nuclear reaction $\mathrm{D}(^3\mathrm{He},\mathrm{p})^4\mathrm{He}$.

The sample is placed in a vacuum chamber and is exposed to a ^{3}He beam with fixed kinetic energy. The intensity of the resulting emitted radiation is recorded by two different detectors placed in precise positions in the chamber: the former can energetically resolve the back-scattered ^{3}He ions producing the so-called Rutherford Back-Scattering (RBS) spectrum; the latter can energetically resolve the protons spectrum that is related to the D concentration. The RBS spectrum is used both to obtain information about film depth and composition and to have estimated data to use in NRA spectra evaluation. In this analysis the incoming beam energy was set to 3.5 MeV in order to have an overall depth D concentration. The SIMNRA software [83] was used to interpret the spectra acquired. NRA makes it possible to achieve depth resolution of the elemental composition of the samples by calibrating the impinging ion energy. Moreover, this is a punctual technique that extracts information about elemental composition from a limited region of samples. Finally, this technique is less affected by errors even though spectra interpretation is more complex and requires precise cross-section reaction database of elements for a correct interpretation.

4

Production and characterization of nanostructured W-based films for fusion-relevant investigations

This chapter aims to report on W-based coatings produced by Pulsed Laser Deposition and used for fusion-relevant studies. As mentioned in section 3.2.1, PLD makes it possible to finely tune a wide range of parameters, such as laser pulse energy, laser spot area, laser wavelength, distance between target and substrate ($\mathrm{d_{t-s}}$), gas atmosphere and its pressure. In this Ph.D. thesis, all these parameters have been varied, primarily to optimize the deposition process and then to find the correct conditions to produce layers suitable for supporting fusion-relevant studies by means of plasma exposures performed in fusion relevant conditions and gas (e.g. He and D) implantation processes. In section 4.1, the production of W films is presented. In particular, it was possible to deposit different film types by changing deposition conditions opportunely: in particular, it was possible to produce metallic films and to control their morphologies and structures (see section 4.1.1). In addition, by using more reactive background gas (i.e. O_2, N_2), it was possible both to tailor W film morphology and structure, to deposit films with the desired amount of background gas trapped within the material matrix, and to obtain films that are completely oxidized or that exhibit some nitride phases (see section 4.1.2 and 4.1.3). In particular, the adopted deposition conditions and their connection with the films' properties, studied by using the analysis technique reported in section 3.3, is discussed. Some relevant films, which will be identified in the following sections, were also thermally annealed in vacuum conditions at different ITER-foreseen temperatures to study their modifications. In section 4.2 these results are reported: in particular, in section 4.2.1 the morphological, structural, stoichiometric and elemental composition changes are assessed. In section 4.2.2, electrical resistivity measurements, exploited to monitor the overall modification of samples, are discussed. During these thermal annealing procedures, mainly due to the samples' metastable state, it has been possible to highlight the possibility of nucleating nanowires of W oxide at a relative low temperature compared with conditions normally used to produce these interesting systems (see section 4.2.3).

4.1 Production and characterization of relevant W-based films

PLD films are produced in order to create deposits whose properties may usefully simulate those of the layers found on PFMs in tokamaks and expected in fusion reactors like ITER and DEMO.

The main results, coming from tile exposures in JET-ILW and AUG, have already been presented in section 2.3.3. In general, the composition of these layers reflects that of the first wall, with the addition of D/T, O and N. Since the aim of this thesis is to provide an experimental investigation about the behavior of non-conventional W-based films in the harsh tokamak environment, the films' production focused on the creation of different W and W compound films, not taking into account the whole possible alloying phenomena that can happen in the case of different first wall materials presence. The features of the AUG and JET-ILW re/co-deposited layers - such as morphology, micro- and nano-structure, thickness - strongly depend on where they build up. The morphology is strictly correlated with the eroded species energy: low energy can lead to the formation of porous depositions, characterized by the presence of voids and low mass density, while high energy eroded species lead to more compact systems. It was possible to control PLD film morphology by varying the background gas type and its pressure. It is possible to modify species energy in the PLD process by changing $\mathrm{d_{t-s}}$. There is a direct connection between the gas pressure, the $\mathrm{d_{t-s}}$ and species' energy: in general, the higher the pressure and the larger $\mathrm{d_{t-s}}$, the lower the energy of the species that impinge onto substrate, leading to more porous film production. Typically, inert noble gas (argon, Ar, and helium, He), oxygen (O_2) and nitrogen (N_2) were employed to control both morphology and, in the case of O_2 and N_2, also the elemental composition and the stoichiometry of the films. The H_2 atmosphere, although of interest, was not investigated because of technical concerns related to its reactivity.

The thickness of re/co-deposited layers can range from a few nanometers up to several microns. Hence, depending on their purpose, PLD W-based film thickness, used in this work, can vary from tens of nanometers up to a few micrometers.

Details about film production and characterization are given in the next section. In particular the produced films have been categorized as follows:

- the samples produced in inert noble gas atmosphere, formally named metallic-W samples (see section 4.1.1);
- the samples produced in O_2 atmosphere, defined as W-O films (see section 4.1.2);
- the samples produced in N_2 atmosphere, defined as W-N films (see section 4.1.3).

In general, preliminary depositions needed to find the process parameters to achieve the desired film properties. In particular, these exploratory depositions made it possible to find the desired laser wavelength, laser pulse energy and fluence, d_{t-s} and substrate holder shift. The laser wavelength was set at $\lambda = 532$ nm. Depending on the focus lens position and laser pulse energy, it was possible to investigate different laser fluence regimes: from about 8 J cm^{-2} up to 16 J cm^{-2}. Since it was fundamental to deposit planar films to have samples with uniform properties, substrate holder shift was finely regulated to find film planarity; moreover, to make it easier to get the right substrate holder shift, different d_{t-s} were explored and it was found that 7 cm was a good value. Typically, these preliminary depositions were performed on silicon (Si) substrate, which is easily available and easy to characterize. Sample morphology was assessed with SEM microscopy and the film thickness ranged between 500-1000 nm. The elemental composition was achieved with EDXS, while Raman spectroscopy, where necessary, was performed to study the chemical and structural properties of samples. Even XRD was used to investigate the nanostructure of the films.

4.1.1 Metallic W films

Metallic W films were obtained using a 99,9 % pure W target ablated by laser pulses having $\lambda = 532$ nm and laser pulse energy of either 700 mJ or 800 mJ. In general, the laser pulse energy was measured outside the PLD system; however, a dedicated investigation showed that the laser pulse energy loss was less than 10% inside the PLD chamber and then negligible in this pulse energy regime. The laser beam spot area on the target was 4.8 cm^2 and the resulting laser fluence was about 15 $\mathrm{J\ cm}^{-2}$ and 16.5 $\mathrm{J\ cm}^{-2}$, respectively. Target to substrate distance was set at 7 cm. These samples were deposited both in vacuum conditions and in a background inert gas atmosphere to assess the effect of gas background pressure on film properties. In particular, the species energy decreases proportionally with background pressure: the ablated material, which can expand in vacuum conditions, reaches the substrate with a higher energy than in the case of plume expansion in background gas, as reported in [69]. In order to increase species energy during vacuum deposition further, the laser spot energy was set at 800 mJ, while in the case of depositions in the presence of background gases the pulse laser energy was set at 700 mJ. In particular, two different inert noble gases, at different pressures, were used: He and Ar.

He pressure ranged between 10 Pa and 200 Pa. In figure 4.1, different sample morphologies, achieved by varying background He pressure, are reported. All samples were characterized with XRD and EDXS (accelerating voltage 15 kV).

XRD spectra are reported in figure 4.2a: the sample deposited in vacuum conditions exhibits preferential growth in the (110) direction. Increasing the deposition pressure, the (110) XRD peak becomes broader and less sharp: it is evident that, for pressure above 10 Pa of He, the ablated species energy is not sufficient to form crystallite domains, leading to extremely disordered films being deposited. By analyzing the (110) peak of these spectra by Scherrer formula, it was possible to obtain the evolution of crystallite dimensions with regard to the He deposition pressure. This trend is reported in figure 4.2b: below 10 Pa of He the crystallite dimension is about 13 nm, while above 30 Pa, d is almost constant and is approximately 1 nm.

Hence, the vacuum condition makes it possible to deposit compact W films characterized by a columnar morphology (appreciable in figure 4.1a) with preferential growth, confirmed by XRD analysis, in the crystallographic (110) direction and with mean crystallite dimensions of about 13 nm. This particular sample was named columnar-W (c-W) and it was investigated in depth in this work. For higher deposition pressures, above 10 Pa, the film structure becomes more disordered with crystallite dimensions of up to about 1 nm: this means that the samples, made in these condi-

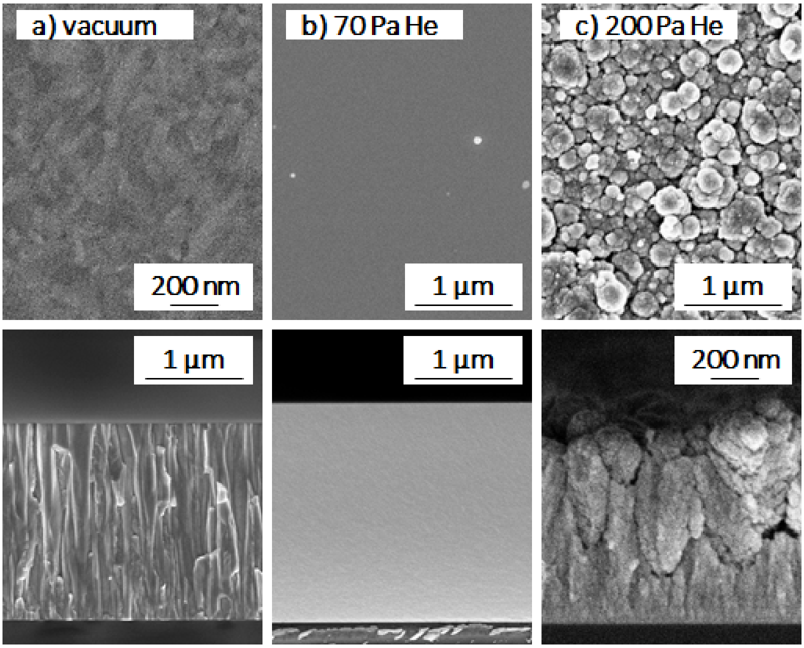

Figure 4.1: *SEM plane view (top) and cross section (bottom) of W films deposited in different background conditions: a) vacuum (0,001 Pa), b) 70 Pa of He and c) 200 Pa of He.*

tions, do not exhibit a long range order. In this deposition regime background pressure does not modify film structure but it makes it possible to finely control film morphology. Indeed, for He pressure between 30 Pa and 100 Pa, the films are compact and with a small number of growth defects. A very representative example of these peculiar films is reported in figure 4.1b: this sample, studied in depth here, was named nanostructured-W (n-W). On the contrary, after increasing the deposition pressure by much more, the ablated species are more efficiently slowed down and this results in having films that exhibit open morphology, porous and with a high concentration of growth defects (the so-called cauliflower growth) as reported in figure 4.1c.

Due to the high affinity of W with O, the elemental composition of these films was monitored using EDXS: the results are reported in figure 4.3. The film deposited in the vacuum condition does not show any O contamination. As reported above, high deposition pressure leads to having a more disordered structure and the morphology is more open. Due to these modifications in film structure and morphology, the O content grows because the available number of sites, where the O can be trapped, in-

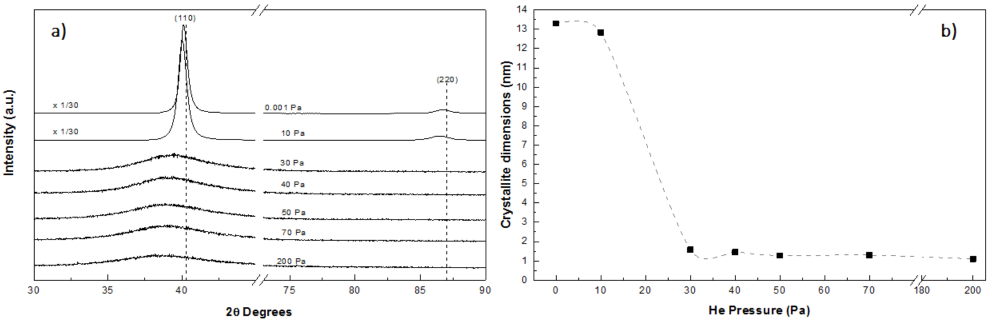

Figure 4.2: *a)XRD spectra of films deposited in different background pressure conditions. b) Variation of crystallite dimension of films respect the deposition pressure.*

creases. In particular, from the graph reported in figure 4.3, it is possible to distinguish three different O content regimes. In particular, the films made between 20 Pa and 40 Pa of He have a mean O concentration of about 5 atomic % with a trend of increasing a little. Those deposited between 50 Pa and 100 Pa show an O content of about 20 atomic %, while, for the highest He pressure investigated, the film exhibits an O concentration of about 60 atomic %. These different amounts of O are strictly correlated with film structure and morphology. In particular, the films made in the 20-40 Pa regime show intermediate features between c-W and n-W. The pressure regime, that makes it possible to obtain n-W film, leads to having a typical O concentration of 20 atomic % independently of deposition pressure; this can be due to the high affinity between W and O that is present as a contamination during the deposition process. The film made in 200 Pa of He has a porous structure that leads to having an extremely high O atomic concentration up to even having partial superficial oxidation (this data was confirmed by Raman analysis not reported here).

Given the higher mass number, Ar is more efficient for confining plasma plume; for this reason, the Ar pressures explored ranged between 5 Pa and 100 Pa. In figure 4.4, some morphologies achieved with different Ar pressures are reported. It is evident that the confinement effect obtained using Ar atmosphere is completely different from that of He. Even at a relatively low Ar pressure (20 Pa), the film is already characterized by a porous morphology (see figure 4.4a). This type of growth is almost constant up to 100 Pa. As a matter of fact, the three films reported in figure 4.4 exhibit the same features and, even though their deposition time is the same, film thickness increases proportionally with deposition pressure. This means

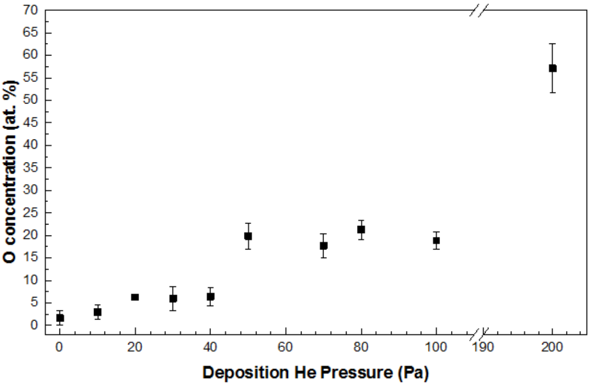

Figure 4.3: *O content in films deposited varying deposition pressure from vacuum (0.001 Pa) up to 200 Pa of He.*

that the morphology becomes more open and the films are accordingly more porous. The properties of these films were investigated using XRD and EDXS (accelerating voltage 15 kV).

Elaborating XRD spectra, like in the case of films deposited in He atmosphere, it was possible to extrapolate, thanks to the Scherrer formula, the mean crystallite size dimension: the evolution of d compared with the Ar deposition pressure is reported in figure 4.5a. Similarly to the He case, the sample made at low pressure (5 Pa) has crystallite dimensions that are almost comparable with those of c-W. For higher pressure, the crystallite dimension drops off, reaching, almost instantaneously, values of about 1 nm for samples deposited in 20 Pa and 30 Pa of Ar. The sample produced in 50 Pa of Ar exhibits a peculiar behavior: in this case, probably due to a coupling effect between plasma plume and background atmosphere, the mean crystallite dimension grows up to 7 nm, even though the morphology is porous. This probably means that the formation of these bigger crystallites happens during the plume expansion and the confinement phase. Due to this feature, the study of these sample properties was developed during this project: the 50 Pa Ar sample was named porous-W (p-W). Apart from this peculiar pressure regime, the sample made at 100 Pa shows a crystallite dimension of about 1 nm.

Since the films made in Ar atmosphere have a porous morphology, it was fundamental to monitor their O content. These results, obtained using the EDXS technique, are reported in figure 4.5b. It is evident that, by increasing the deposition pressure, the O content in films increases proportionally. The Ar films behave differently compared with those deposited in the He atmosphere: in particular, it is not possible to identify O content

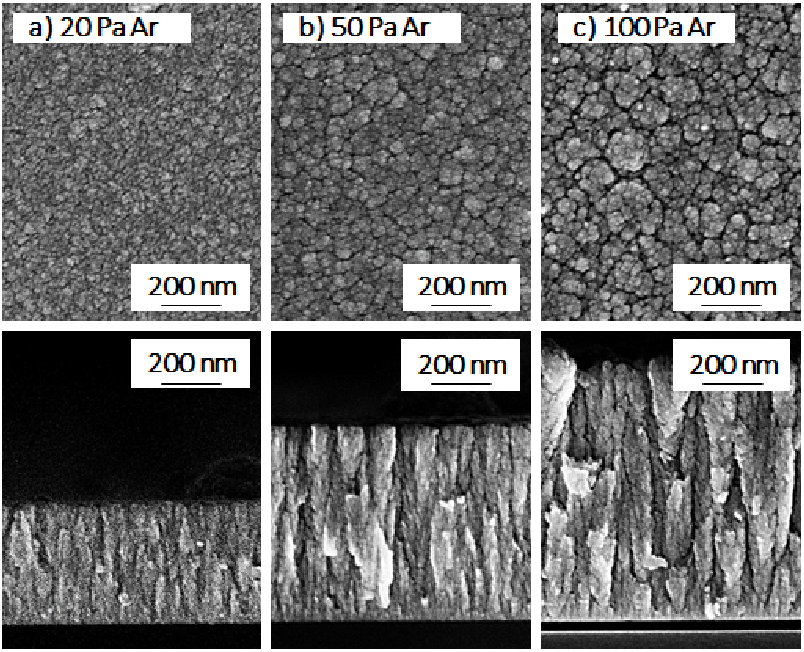

Figure 4.4: *SEM plane view (top) and cross section (bottom) of W films deposited in different background conditions: a) 20 Pa of Ar, b) 40 Pa of Ar and c) 100 Pa of Ar.*

regimes depending on deposition pressure, but only an increasing trend in O content. This result is strictly correlated with the morphology of films made in the Ar atmosphere, which, as anticipated above, is porous. As a matter of fact, by calibrating He pressure opportunely, it is possible to deposit compact films without long range order, while in the case of Ar this option is not feasible. Hence, the higher films' porosity makes it possible to have a high number of sites where the O can be trapped and, if the morphology is extremely porous, like in the case of the deposition in 200 Pa of He, this can cause a little partial superficial oxidation of films.

To conclude, by using PLD capabilities, it was possible to deposit very interesting metallic films with different properties that are summarized in table 4.1:

- **c-W film** (deposited in vacuum conditions with high laser fluence = 16.5 J cm^{-2}) exhibits compact columnar morphology with a preferential growth in the (110) crystallographic direction. The mean crystallite size is about 13 nm and the O content is negligible; as reported in sections 5.1 and 5.3, c-W films were exposed both to D and He-D plasmas.

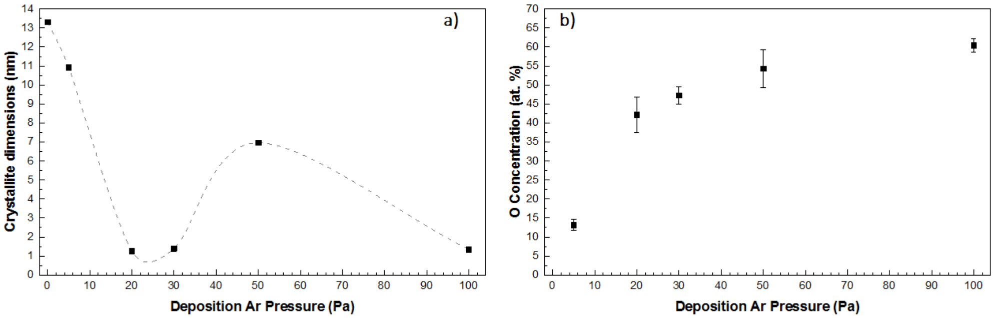

Figure 4.5: *a) Variation of mean crystallite dimension compared to the Ar deposition pressure. b) O content in films deposited in different deposition pressures, from vacuum (0.001 Pa) up to 100 Pa of Ar.*

	Deposition pressure (Pa)	**Background gas**	**Crystallite dimension (nm)**	**Oxygen content (at. %)**
columnar-W	0.001	vacuum	≈ 14	≈ 0
nanostructured-W	70	He	≈ 2	≈ 20
porous-W	50	Ar	≈ 7	≈ 55

Table 4.1: *Main properties of the main W metal film deposit in vacuum, Ar and He atmosphere.*

- **n-W film** (deposited in 70 Pa of He with high laser fluence = 15.0 J cm^{-2}) shows amorphous-like compact featureless morphology. There is no long range order and the mean crystallite size is about 1 nm. Due to the high defects concentration the O content is about 20 atomic %; as reported in sections 5.3 and 5.3, n-W films were exposed both to D and He-D plasmas.

- **p-W film** (deposited in 50 Pa of Ar with high laser fluence = 15.0 J cm^{-2}) has a porous and open morphology. The mean crystallite size is about 7 nm, probably due to strong interaction between plume and background gas. The oxygen content is about 55 atomic % and a partial superficial oxidation driven by porous morphology is present; as reported in sections 5.1 and 5.3, p-W films were exposed both to D and He-D plasmas.

4.1.2 W-O films

Oxide W films were obtained using a 99,9 % pure W target ablated by laser pulses having $\lambda = 532$ nm and laser pulse energy of 700 mJ. The laser beam spot area on target was 4.8 cm^2 and the resulting laser fluence was about 15 J cm^{-2}. Target to substrate distance was set at 6 cm. These samples were deposited in a reactive O_2 gas atmosphere to assess the role of gas pressure on film properties (i.e. morphology, stoichiometry and elemental composition). As already described, the species energy decreased proportionate to the background pressure; moreover, O_2 is a reactive gas that reacts chemically with ablated species during plume expansion, thereby enabling the formation of oxide films. The O_2 pressure was varied between 5 Pa and 100 Pa. In figure 4.6, different sample morphologies achieved with varying O_2 background pressures are reported. All samples were characterized by Raman spectroscopy and EDXS (accelerating voltage 15 kV).

SEM analysis highlighted that background pressure deeply affects the films' morphology: in particular, samples produced below 30 Pa of O_2 exhibit a compact morphology, while, for higher pressure, the samples are

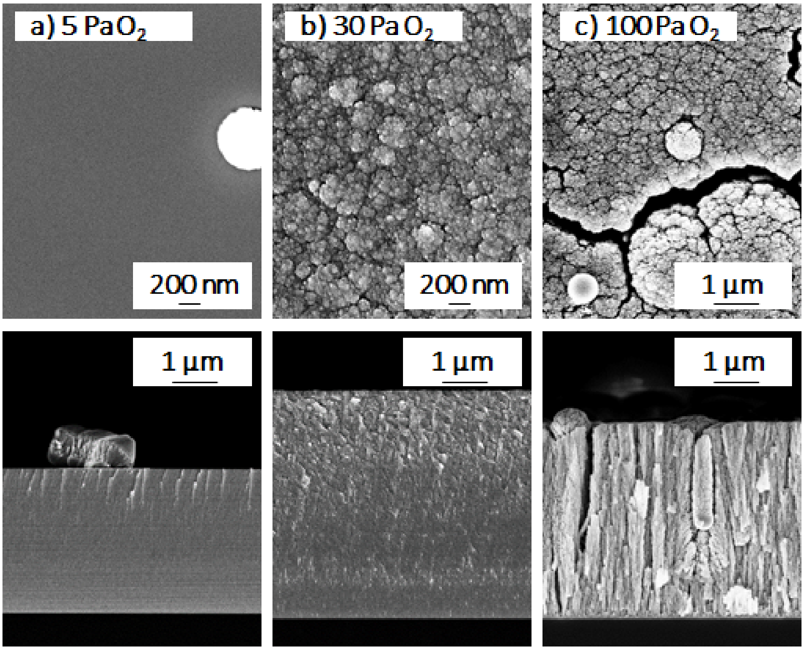

Figure 4.6: *SEM plane view (top) and cross section (bottom) of W films deposited in different background* O_2 *pressure: a) 5 Pa of* O_2*, b) 30 Pa of* O_2 *and c) 100 Pa of* O_2*.*

porous with an open morphology. In figure 4.7, the results obtained from EDXS investigation are reported. In particular, it is possible to note that, when the O_2 deposition pressure is increased, the O/W ratio grows. The most common W oxide is tungsten trioxide (WO_3) and its O/W is equal to 3. Raising O_2 background pressure up to 30 Pa the O/W ratio in the deposited films increases up to 3, which corresponds to WO_3 stoichiometry. Over 30 Pa, the ratio remains constant, also raising pressure up to 100 Pa. To support these results, Raman spectroscopy was performed to study sample oxidation and stoichiometry. For films deposited in an O_2 atmosphere below 30 Pa no Raman signal is detected, revealing their metallic nature. Above 30 Pa of O_2, Raman spectra show a low frequency band in the range of 100-500 cm^{-1}, associated with O-W-O bending modes, a band in the 600-900 cm^{-1} range, associated with W-O stretching modes and a band at about 960 cm^{-1} attributed to W=O stretching modes at grain boundaries, therefore related to the presence of nano-grains [84]: this typical broad band feature in Raman spectra implies that the deposited oxide films are nearly stoichiometric amorphous tungsten oxide (a-WO_3) [84]. In these spectra a narrow peak at 521 cm^{-1} due to the first order scattering from silicon substrate is also evident: this confirms the optical transparency properties of these films due to their oxide nature.

Thanks to the great PLD flexibility, it was also possible to deposit multi-layer systems, reported in figure 4.8, and O loaded n-W films. In particular, figures 4.8a and c report multilayer films where, respectively, compact a-WO_3 (made in 30 Pa of O_2) and porous a-WO_3 (made in 100 Pa of O_2) are embedded between two thin layers of c-W. In figure 4.8b a thin layer of compact a-WO_3 is deposited on a thicker c-W layer.

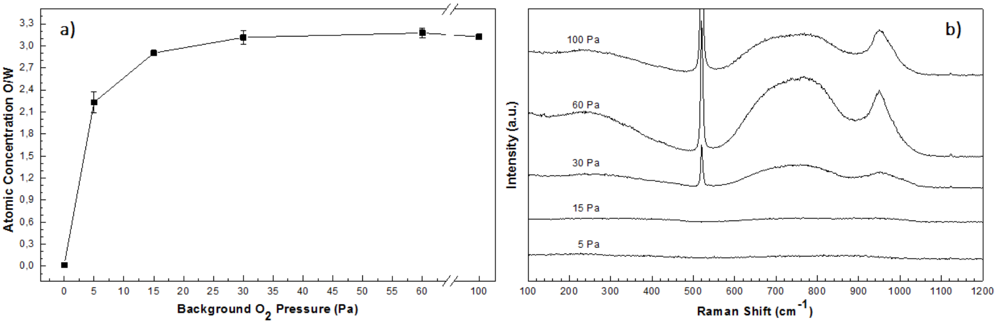

Figure 4.7: *a) O/W variation respect the* O_2 *deposition pressure. b) Raman Spectra of films deposited at different* O_2 *pressure.*

Oxygen-loaded n-W were obtained by depositing these films in a mixed

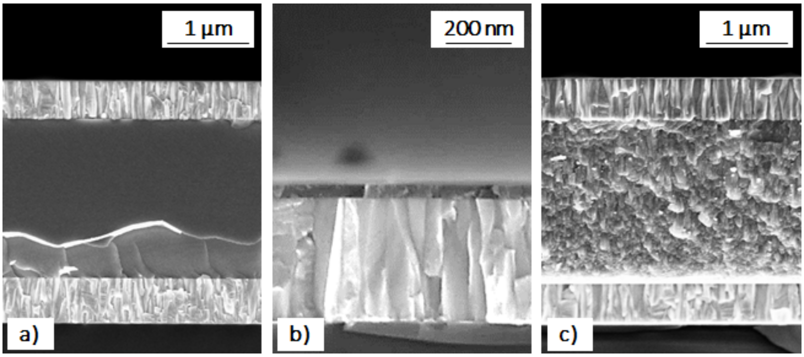

Figure 4.8: *SEM cross section views of the most relevant W and W oxides multilayer systems produced by PLD: a) compact a-*WO_3 *(30 Pa of* O_2*) layer embedded between two thin layers of c-W, b) thin layer of compact a-*WO_3 *deposited on thick layer of c-W and c) porous a-*WO_3 *(100 Pa of* O_2*) layer embedded between two thin layers of c-W.*

atmosphere of He with little and controlled contamination of O_2, keeping the total pressure constant. The main result is that, by exploiting this trick, it is possible to have films with the same compact featureless morphology but different oxygen content. In particular, during the deposition process, the O_2 flow was set at 1, 2.5, 5 and 10 flux % compared to that of He. The EDXS results and Raman spectra are reported in figures 4.9a and b respectively. It is possible to appreciate that by increasing the O_2 contamination, the O amount in film increases, even if the oxidation of the deposit is almost negligible in all cases (see Raman spectra reported in figure 4.9b).

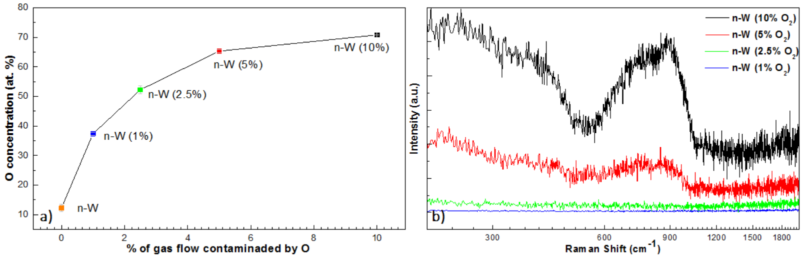

Figure 4.9: *a) O concentration in films with regard to different gas flow contamination. b) Raman spectra of samples made with different* O_2 *contaminations.*

To conclude, different types of W and WO_3 coatings, with high property control, were produced by using PLD; their main features are reported below with an overview of their purposes in fusion-relevant plasma exposure(see chapter 5):

- metallic W films with a controlled amount of non-bonded O were made both below a threshold pure O_2 background pressure (30 Pa) and by using depositions in mixed He-O_2 atmospheres. In particular, these films (named **modified O-loaded n-W**) were exposed to pure D plasma in the PSI-2 machine to assess the role of O trapped in films with regard to D amounts retained by film itself (see section5.2.1);

- a-WO_3 was produced by depositing films above the background pressure of 30 Pa of pure O_2; moreover, it was possible to control film morphology, from compact to porous, by tuning deposition pressure. In particular, 30 Pa O_2 atmosphere was selected as a reference pressure to produce **compact amorphous nearly stoichiometric tungsten trioxide** (compact a-WO_3), which was studied after its exposure to MAGNUM-PSI D plasma (see section 5.2.2);

- by exploiting the great PLD versatility, it was possible to make **multi-layer structures** where compact a-WO_3 can be deposited either above a c-W film or between two c-W layers. The former system was exposed to D plasma generated by MAGNUM-PSI to simulate a thin oxide layer above PFCs and its behavior when facing fusion-relevant plasma (see section 5.2.2).

4.1.3 W-N films

This investigation was developed following precise indications given by EUROFUSION Work Plans and it is a work in progress. In particular, a great effort is being made to produce samples with porous morphology with precise concentrations both of O and N trapped in the film matrix.

W-N films were obtained using a 99,9 % pure W target ablated by laser pulses having $\lambda = 532$ nm and laser pulses energy of 700 mJ. The laser beam spot area on target was 4.8 cm^2 and the resulting laser fluence was about 15 J cm^{-2}. Target to substrate distance was set at 7 cm. These samples were deposited in a reactive N_2 gas atmosphere to assess the role of gas pressure in film properties (i.e. morphology, stoichiometry and elemental composition). As already described, the species energy decreases proportionally with background pressure; moreover, N_2 is a reactive gas that can chemically react with ablated species during plume expansion, making it possible to form partial nitride films. The N_2 pressure was varied between 2.5 Pa up to 20 Pa. In figure 4.10, different sample morphologies achieved with varying N_2 background pressure are reported. All samples were characterized with XRD and EDXS (accelerating voltage 15 kV).

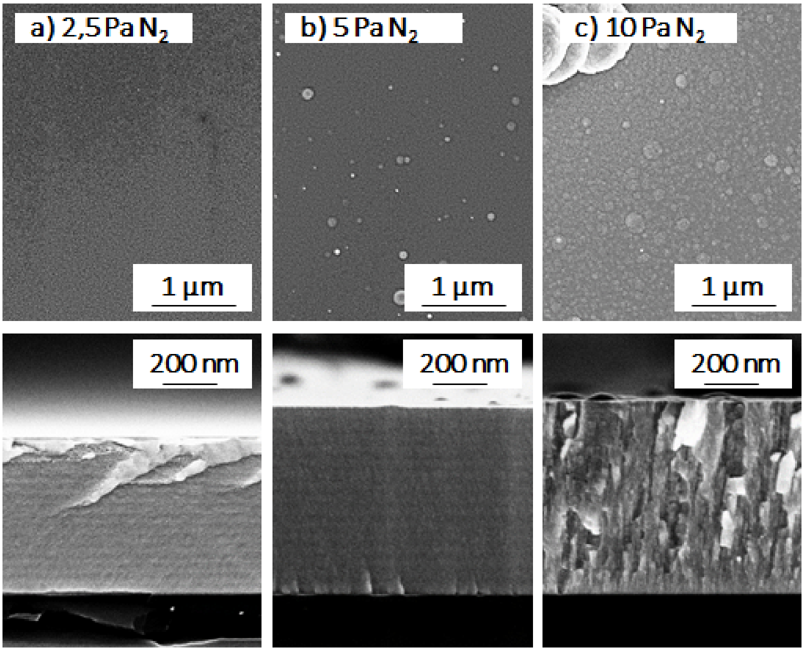

Figure 4.10: *SEM plane view (top) and cross section (bottom) of W films deposited in different background* $\mathrm{N_2}$ *pressure: a) 2.5 Pa of* $\mathrm{N_2}$*, b) 5 Pa of* $\mathrm{N_2}$ *and c) 10 Pa of* $\mathrm{N_2}$*.*

As already highlighted in the previous sections, the main effect of raising deposition pressure results in going from a compact morphology (figure 4.10a) to a porous morphology (figure 4.10c). Moreover, different deposition pressures lead to having both different crystallographic structures and elemental compositions in the deposited films. These differences were confirmed by XRD and EDXS analysis, reported in figures 4.7a and b, respectively.

In figure 4.11a, the XRD spectra of films made in different $\mathrm{N_2}$ are reported; the blue dashed line reports the X-ray diffraction from the crystallographic plane (110) of bulk W. n-W, due to its amorphous-like structure, exhibits a right shift of this XRD W peak, and the exact position is indicated with a red dashed line. The green dashed lines show the positions of XRD peaks attributed to the presence of W nitride ($\mathrm{W_2N}$) in its hexagonal phase. From XRD data, it is possible to note that the sample deposited in 2.5 Pa of $\mathrm{N_2}$ shows a broad band in the same position as n-W. Raising the deposition pressure, this band shifts to the left and in the cases of depositions made in 10 Pa and 20 Pa of $\mathrm{N_2}$ the respective bands overlap with XRD peak positions of $\mathrm{W_2N}$. To support these results,

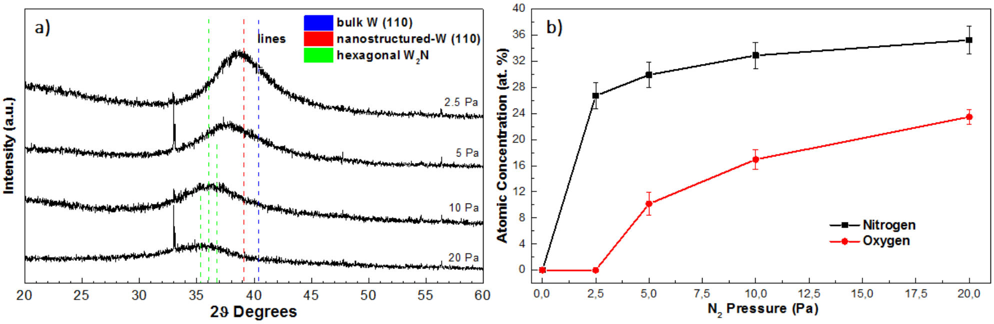

Figure 4.11: *a) XRD spectra of samples deposited in different* N_2 *pressure. b) Atomic concentration of N and O in films deposited in* N_2 *different background pressure.*

the elemental composition of samples was assessed by EDXS. The results are reported in figure 4.11b. It is possible to observe that, for the lowest N_2 deposition pressure (2.5 Pa), the N present is about 27 atomic % and there is no presence of O. Since in W_2N, the N is about the 33 atomic %, the N quantity in the film deposited in 2.5 Pa of N_2 is not sufficient to induce the formation of W nitride. This result is also confirmed by the XRD analysis discussed above. On the contrary, the samples made in higher N_2 pressure show a higher N concentration, up to 33 atomic %, combined with a raising O concentration that is mainly due to the open morphology of films. This result, combined with XRD observation, makes it possible to tentatively conclude that the sample made in 5 Pa of N_2 has intermediate properties between the samples that are mainly metallic (2.5 Pa of N_2) and those that exhibit a partial formation of nitrides (10 Pa and 20 Pa of N_2) as confirmed by XRD peak positions.
Nowadays, these investigations have been developed in depth: in particular, it has been found that, by exploiting a similar strategy to that used to produce modified O loaded n-W (see section 4.1.2), it is possible to control both film morphology and N content. In particular, these films were produced in 50 Pa Ar background atmosphere, where a controlled flux of N_2 was deliberately inserted. The main result of this investigation was that porous W films with a N content that ranges between 10-25 atomic % were produced.

To conclude, it was demonstrated that, by finely tuning the deposition pressure and its composition, both film morphology and elemental composition control were obtained. Moreover, different background N_2 pressure made it possible to deposit both mainly metallic films with a high N amount trapped in films (below 2.5 Pa of background pressure)

and nitride films (above 10 Pa of N_2 pressure during deposition) with an open morphology that consequently induces O concentration in deposited films. Finally, by depositing films in a controlled, mixed Ar-N_2 background atmosphere, an elevated film elemental composition control was achieved, keeping the morphology constant.
To summarize, it was possible:

- to control film morphology and structure by changing the N_2 deposition pressure;
- to deposit both metallic films with a high concentration of N trapped (below 10 Pa of N_2) and films with the presence of nitride phases (above 10 pa of N_2);
- to finely tune N content in films, keeping their morphology constant. This was possible by exploiting depositions in a mixed Ar-N_2 atmosphere where the N_2 presence was calibrated and the total deposition pressure was kept constant.

4.2 Thermal annealing effects on selected W-based films

In the previous sections, some relevant films were identified: the columnar-W (c-W), the nanostructured-W (n-W), the porous-W (p-W) and the compact amorphous nearly stoichiometric W trioxide (a-WO_3) films. As highlighted in section 2.1.1, first wall materials and, consequently, the re/co-deposited layers have to face severe thermal loads during fusion reactor operations. Given their complex morphology and structure, the re/co-deposited layers are deeply modified by these extreme conditions. During the steady-state regime, the divertor temperature in ITER should range between 150°C and 850°C [85], but ELMs and off-normal events can bring the materials to higher temperatures. In this temperature regime, neutron-damaged W exhibits three principal recovery defect stages [86]: at $0.15T_{\text{melt}}$ (100-450°C, known as stage III) self-interstitials start to migrate: they may either annihilate at vacancies or form interstitial clusters, or migrate to dislocations and grain boundaries. At $0.22T_{\text{melt}}$ (450-650°C, named stage IV), di-vacancies, impurities, impurity defect complexes and interstitials escape from shallow impurity traps and at $0.31T_{\text{melt}}$ (650-1000°C, known as stage VI) vacancies begin to recover and the crystal grains start to grow. However, this interpretation was revised later and, in particular, stage III was attributed to vacancy migration [87]. Based on these findings, a recent investigation [88] concluded for W, that from 250°C to 500°C single vacancies diffuse through the materials and can agglomerate to form larger defects or annihilate at sinks like grain boundaries. There was some speculation regarding this topic [27, 89]: in particular, the annealing from 150°C to 450°C may be associated with single vacancies migration, while higher temperatures (up to 900°C) may be associated with vacancy cluster migration, annihilation and coalescence. This already complex scenario is further complicated by the presence of peculiar re/co-deposited layers. Specifically, in order to understand the modifications induced exclusively by different temperature regimes and not by transient events (e.g. ELMs), the selected proxy-films, produced by PLD and reported above, were thermal annealed at different ITER-relevant temperatures in a vacuum atmosphere. Films were characterized after thermal treatments to assess the modifications of their morphology, crystalline structure, elemental composition and stoichiometry (see section 4.2.1). In complex systems, such as nanostructured films, electrical resistivity is extremely sensitive to modifications induced by thermal annealing. For this reason, c-W and n-W films' electrical properties were investigated in depth to understand the relation between thermal induced film modifications and films' electrical resistivity. These results are reported in section 4.2.2. Finally, unique features of n-W films made it possible to nucleate tungsten oxide nanowires (NWs), selecting opportunely both film properties and thermal annealing conditions [90] (see section 4.2.3).

4.2.1 Film property modification

W-based films were annealed in a vacuum atmosphere (10^{-6} Pa) varying the temperature between 100°C and 1250°C in 50°C increments. The heating rate was set at 50°C/minute. The system was left free to cool down to room temperature. The set temperature was maintained for 1 hour.

Surface morphological modifications of c-W films induced by thermal annealing are reported in figure 4.12. SEM images underline that the samples' surface morphology is stable and it does not change up to 550°C, while, when the temperature is raised, the modifications are evident; in particular, it is possible to note the beginning of grain growth process. The grain growth is confirmed by XRD spectra reported in figure 4.13a: the intensity of (110) XRD peak increases, and this means that film crystalline order improves, enlarging its grain dimensions. It is worth noting that,

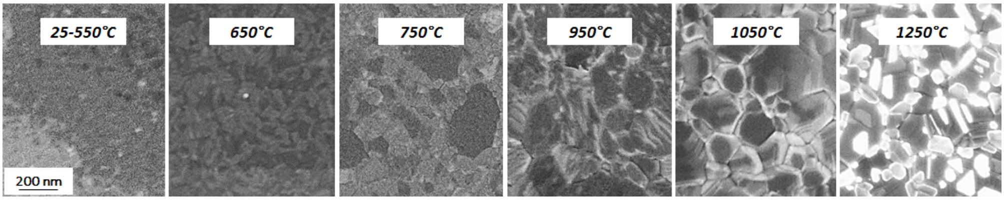

Figure 4.12: *SEM plane view of c-W films annealed at different temperatures: there are no evident morphological changes up to 550° C, while higher annealing temperatures induce evident grain growth processes.*

in spite of thermal treatment, the films maintain their crystallographic orientation along (110) (or equally along the (220) direction). In particular, elaborating this data with the Scherrer formula, it was possible to extrapolate the mean crystallite size (see figure 4.13b). It is worth noting that there are many differences between grain and crystallite dimensions. It is possible to summarize by saying that a crystallite represents the materials portion characterized by the absence of defects, while a grain is the materials portion defined by grain boundary defects and a grain can include 1D (e.g. vacancy and interstitial) and 2D (e.g. dislocation and dislocation loops) defects. Figure 4.13b reports the mean crystallite size variation compared to the annealing temperature. Partially confirming the SEM observations, the film crystallite dimension dramatically changes from 650°C. Fitting experimental points with a Boltzmann curve [1], it is possible to estimate a crystallization temperature of about 630°C that is in total accordance with the SEM observations reported above and the literature results reported in the introduction to this section.

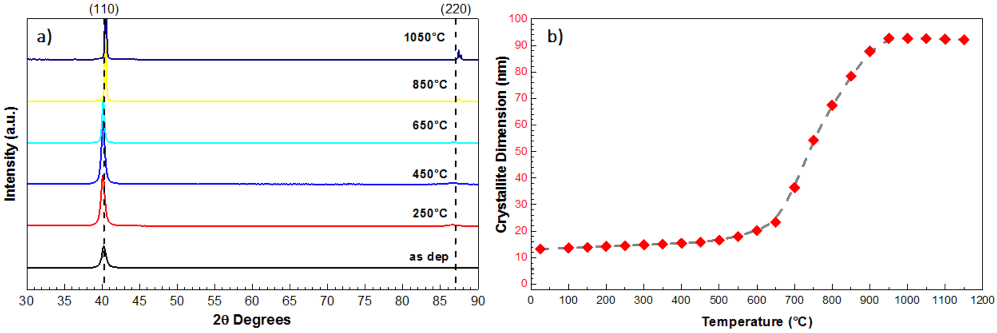

Figure 4.13: *a) XRD spectra of c-W samples annealed at different temperatures. b) Mean crystallites sizes evolution with regard to annealing temperature.*

---

[1] $d = d_{min} + \frac{d_{max} - d_{min}}{1 + e^{(T - T_0)/dt}}$

Surface morphological modifications of n-W films induced by thermal annealing are reported in figure 4.12. Like in the case of c-W, there are no evident morphological changes up to 550°C, while, when raising the temperature, the grain growth process seems to start. XRD measurements are reported in figure 4.15a. It is evident that, unlike the case of c-W, film properties start to change at a low temperature: the XRD spectrum of as deposited sample exhibits a typical broad band centered around 40°, described in section 4.1.1. Already annealing n-W at 150°C, the typical broad band of n-C changes in a sharper peak centered around the (110) reflection of W: this means that crystallites are grown. Moreover, when the annealing temperature is raised, this peak becomes more and more defined and sharp and other typical W XRD reflections appear ((112), (200) and (220), respectively). This means that films do not have a preferential grain orientation and, consequently, they have more isotropic grains orientation. By elaborating the most intense XRD peak (100) with the Scherrer formula, it was possible to quantify mean crystallite sizes of thermal annealed films (red diamond in figure 4.15b). It is evident, as qualitatively already observed from XRD spectra, that mean crystallite sizes increase starting at relatively low temperatures; this process maintains a constant slope up to about 700°C, then the crystallites grow exponentially in the temperature range between 700°C and 1000°C. For temperatures above 1000°C, the crystallite sizes rise with a little slope in relation to the chosen annealing temperature. As already discussed in section 4.1.1, the unique morphology and micro- and nanostructure of n-W lead to O inclusions in the deposited films. Evidently, thermal annealing treatments modify the amount of O trapped and, by exploiting EDXS measurements, this variation was studied. In figure 4.15, the green squares show the variation of O content with regard to the annealing temperature. It is possible to note that there is a constant reduction in amount of O up to 400°C, then there is a region where O concentration remains stable (from 400°C

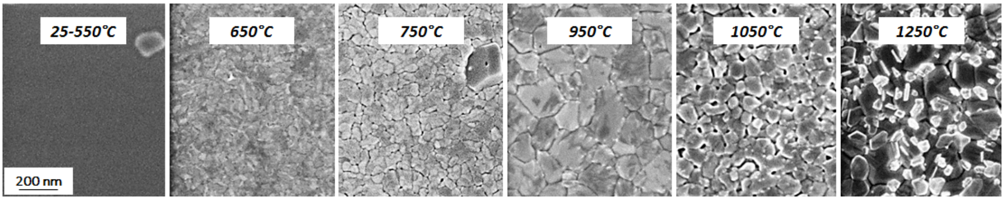

Figure 4.14: *SEM plane view of n-W films annealed at different temperatures: there are no evident morphological changes up to 550° C, while higher annealing temperatures induce evident grain growth processes.*

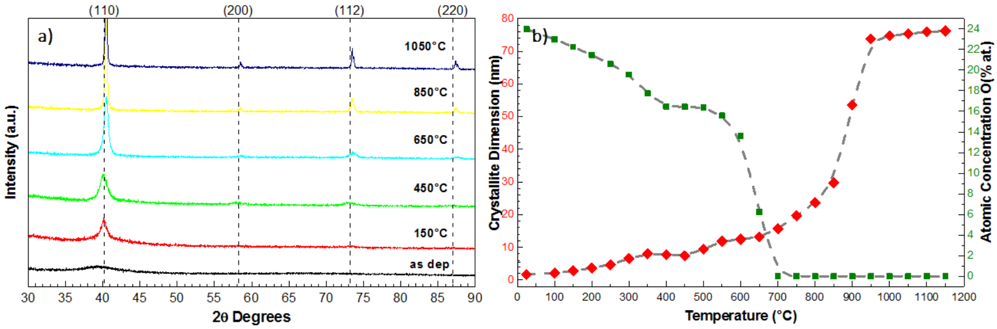

Figure 4.15: *a) XRD spectra of n-W samples annealed at different temperatures. b) Mean crystallites sizes (red diamond) and O content (green square) evolution with regard to annealing temperature.*

up to 550°C). For temperatures higher than 550°C, the O rapidly decreases up to 700°C and, from this temperature, the O content in films is negligible. It is possible to interpret this trend as follows: the first O loss stage (from room temperature up to 400°C) is mainly due to the transition from an amorphous-like structure to a more ordered one. As confirmed by XRD spectra and SEM analysis, films do not considerably change their morphology but their crystallite dimensions increase. Due to these modifications, trapped O is partially released during annealing treatments. In the 400-550°C temperature range, as better explained in section 4.2.3, tungsten oxide NWs can nucleate on film surfaces if some conditions are fulfilled: i.e. annealing temperature, annealing time and O content in films. The tungsten oxide NWs nucleation brings to have a thin partially oxidized superficial layer that influences EDXS O content evaluation, since EDXS measures are a mean element concentration in a finite analysis volume. For temperatures above 550°C, film morphological, micro- and nanostructural properties change dramatically: as a matter of fact, a drastic O reduction happens from 550°C up to 700°C, while, above 700°C, the O content is negligible.

Moreover, it is known that thermal treatments modify both film nanostructure and mechanical properties. Mechanical properties (i.e. elastic moduli) of c-W and n-W, both annealed and not, films were measured by Brillouin spectroscopy. This investigation, reported in [91], confirmed that crystallization temperature for n-W is about 650°C, as discussed above, and that the n-w film recovers up to 70 % of c-W mechanical properties when it is thermally annealed at 800°C. These results partially confirm the conclusions reported above.

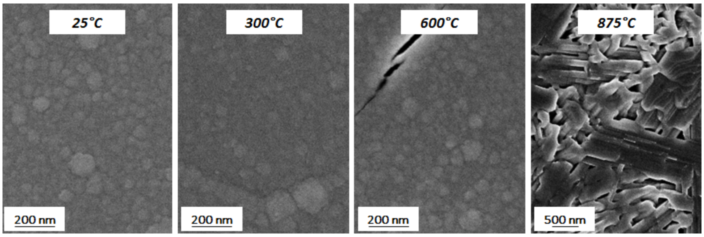

Figure 4.16: *SEM plane view of compact a-*WO_3 *films annealed at different temperatures: there are no evident morphological changes up to 300° C, while the sample annealed at 600° C exhibits the formation of cracks and the sample annealed at 875° C highlights the formation of nanosheets.*

To conclude, figure 4.16 reports surface morphological modifications of compact a-WO_3 films induced by thermal annealing in a vacuum atmosphere, while figure 4.17a shows films' Raman spectra after annealing and figure 4.17b depicts the variation in the O/W ratio. The film deposited at room temperature (25°C) and the one annealed at 300°C keep the same surface morphology (as reported in figure 4.16) and structure (see Raman spectra in figure 4.17a). These results show that,below 300°C, compact a-WO_3 is quite stable. At higher temperatures, modifications occur. Sample annealed at 600°C exhibits morphological modifications, such as cracks that interrupt film continuity. Its Raman spectrum presents narrow peaks at 135 cm^{-1}, 270 cm^{-1}, 721 cm^{-1} and 812 cm^{-1}, showing that, at this temperature, a-WO_3 crystallizes as monoclinic WO_3 [92,93]. On the contrary, film annealed at 875°C exhibits an evident morphological modification that leads to the formation of thick NWs and nanosheets on the surface of the sample. These morphological features, together with the very complex peaks pattern reported in the Raman spectrum in figure 4.17a, attest to the formation of the Magneli phase, which is a sub-stoichiometric phase of WO_3, defined as $W_{18}O_{49}$ (or $WO_{2.75}$) [92, 94]: the decrease in the O content is caused by the annealing treatment in the vacuum atmosphere. In figure 4.17b it is possible to appreciate the variation of the O/W ratio, measured by EDXS, compared with the annealing temperature: it is evident that O loss is mainly due to the reducing atmosphere where the annealing treatments are performed and it is proportional to the chosen temperature. Moreover, in spite of the Raman spectroscopy results, it is evident that EDXS measurements are generally affected by some systematic errors in revealing O, which lead to the total amount of O in films being underestimated.

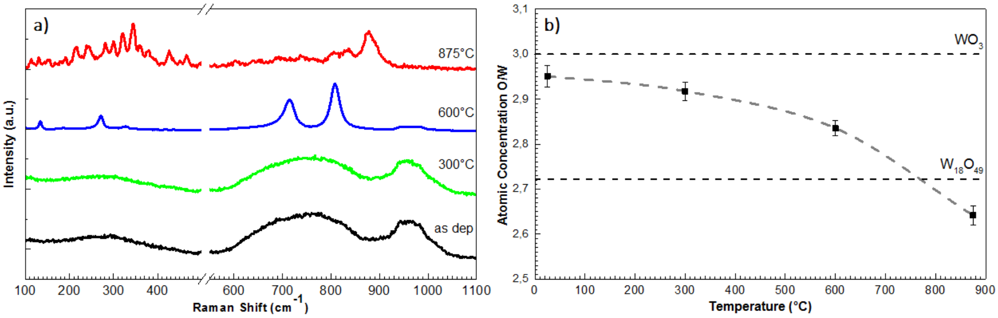

Figure 4.17: *a) Raman spectra of compact a-*WO_3 *samples annealed at different temperatures. b) O/W ratio evolution with regard to annealing temperature; the dashed horizontal lines represent the O/W ratio of* WO_3 *and* $W_{18}O_{49}$.

4.2.2 Electrical resistivity characterization

Films' electrical resistivity ρ_{film}, measured using the Van der Pauw method (see section 3.3.4), of c-W and n-W samples was evaluated after each annealing treatment described above. The results are reported in figures 4.18a and 4.18b, respectively. It is worth noting that, given the different morphology and structure of c-W and n-W, the ρ_{film} of as-deposited c-W is about 26 $\mu\Omega$ cm ($\approx$ 5 times higher than bulk W electrical resistivity $\rho_0 = 5.5\mu\Omega$ cm), while, due to its more disordered nature, ρ_{film} of as-deposited n-W is about 220 $\mu\Omega$ cm ($\approx$ 40 times higher than $\rho_0 = 5.5\mu\Omega$ cm). In the case of c-W, the ρ_{film} decreases in an almost linear manner in the range of 100-650°C; then there is a change in curve slope (650-850°C) and, finally, the ρ_{film} becomes stable independently of annealing temperature. This partially confirms observations on mean crystallite size variation made in section 4.2.1. In the n-W case, the ρ_{film} variation rapidly starts from 100°C up to 400°C, then there is a slower drop up to 750°C and, finally, the ρ_{film} becomes almost stable independently of annealing temperature. This partially confirms observations on O content variation made in section 4.2.1. In general, micro- and nanostructured films exhibit properties that depend on deposition conditions and that can easily change when post-deposition treatments are performed (e.g. thermal annealing). In particular, ρ_{film} measurements were used to probe different film properties [95–99], e.g. film morphology, defect concentrations, transition temperatures and film thickness. Moreover, electrical resistivity measurements were also employed to evaluate the modification induced by neutron fluxes on materials and the possibility of recovering neutron-induced defects by thermal treatments [86]. In general, when an electron

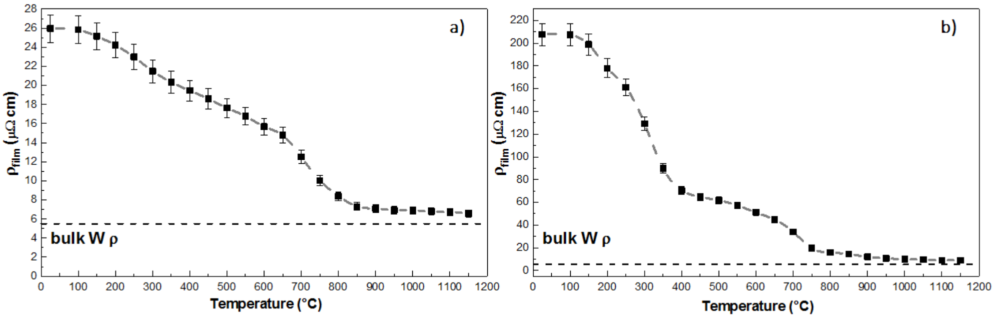

Figure 4.18: *a)* ρ_{film} *variation compared with annealing temperature for c-W samples. b)* ρ_{film} *variation with regard to annealing temperature for n-W samples.*

travels along a material, it can experience different scattering events due to the presence of material surfaces ρ_{surface}, grain boundaries ρ_{grain}, defects ρ_{defect} and impurities $\rho_{\text{impurities}}$. It is possible to separate each contribution as follows:

$$\rho_{\text{film}} = \rho_0 + \rho_{\text{surface}} + \rho_{\text{grain}} + \rho_{\text{defect}} + \rho_{\text{impurities}} \tag{4.1}$$

where ρ_0 is the material bulk electrical resistivity.

Since ρ_{defects} and $\rho_{\text{impurities}}$ are a priori unknown, if the aim is to monitor the defect and impurity concentration evolution with regard to the annealing temperature, it was demonstrated that it is partially possible to model film $\rho_{\text{surface}} + \rho_{\text{grain}}$ using the combined Fuchs-Sondheimer (FS) and Mayadas-Shatzkes (MS) method [100, 101], which takes into account the reflection of electrons at the film surface and interface (FS) and at the grain boundaries (MS). Moreover, it is possible to estimate the contribution due to the impurities ($\rho_{\text{impurities}}$), with an empirical correction factor [97].

If the electrons' free mean path (λ_0) in the films is less than film thickness (t), it is possible to write ρ_{surface} and ρ_{grain}, respectively, as follows, using FS and MS methods:

$$\rho_{\text{surface}} = \rho_0 \frac{3\lambda_0}{8\mathrm{t}}(1 - \mathrm{p}) \tag{4.2}$$

$$\rho_{\text{grain}} = \rho_0[-\frac{3\lambda_0}{2\mathrm{D}}\frac{\mathrm{R}}{1-\mathrm{R}} + 3(\frac{\lambda_0}{\mathrm{D}}\frac{\mathrm{R}}{1-\mathrm{R}})^2] \tag{4.3}$$

where p is the surface reflection coefficient, D the grain size and R the grain reflection coefficient. In general, if $\lambda_0 \ll \mathrm{t}$, the surface effect is almost negligible and it is possible to fix $\mathrm{p} = 0.5$. Vice versa, the grain scattering events lead to drastic changes in ρ_{film} and the evaluation of parameters λ_0, R, D, ρ_0 and t is crucial. For the purposes of this thesis, some assumptions and approximations have been done for W metal films:

- λ_0 is fixed equal to 19 nm [102];
- R is kept equal to 0.4 [103];
- D is approximated with crystallites mean size (d) that represents a lower limit;
- ρ_0 is set equal to 5.5 $\mu\Omega$ cm^1, as reported above;
- t is evaluated by SEM cross-section measurements.

By using this calculation it is possible to obtain the so-called $\rho_{\text{theoric}} = \rho_0 + \rho_{\text{surface}} + \rho_{\text{grain}}$ and hence, subtracting ρ_{theoric} to ρ_{film}, it is possible to estimate:

$$\rho_{\text{defect}} + \rho_{\text{impurities}} = \rho_{\text{film}} - \rho_{\text{theoric}} \tag{4.4}$$

which is reported in figures 4.19a and b, respectively, for c-W and n-W. Therefore, with this calculation, only the contributions to ρ due to defects and impurities remain: as a matter of fact, the contributions due to the film nature are removed. The c-W case is rather clear: as a matter of fact, c-W films exhibit no impurities from EDXS measurements and, hence, $\rho_{\text{film}} - \rho_{\text{theoric}} = \rho_{\text{defect}}$. So, as it is possible to appreciate from figure 4.19a, the defects concentration in c-W decreases in a linear manner up to 650°C during recovery stages III and IV, while the recovery process is more evident in stage VI. The case of n-W is more complex: as a matter

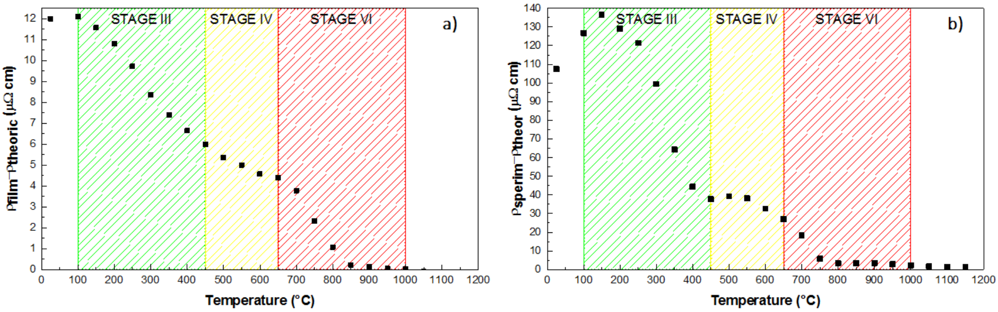

Figure 4.19: *a)* $\rho_{\text{film}} - \rho_{\text{theoric}}$ *variation with regard to annealing temperature for c-W samples. b)* $\rho_{\text{film}} - \rho_{\text{theoric}}$ *variation with regard to annealing temperature for n-W samples. To note that W recovery temperature ranges are reported in both graphs.*

of fact, EDXS analysis highlights the presence of O impurities in films and this can qualitatively explain the peculiar behavior of $\rho_{\text{film}} - \rho_{\text{theoric}}$ reported in figure 4.19b. Remembering the trend of O content in film with regard to the annealing temperature, it is possible to conclude that $\rho_{\text{film}} - \rho_{\text{theoric}}$ have a similar pattern.

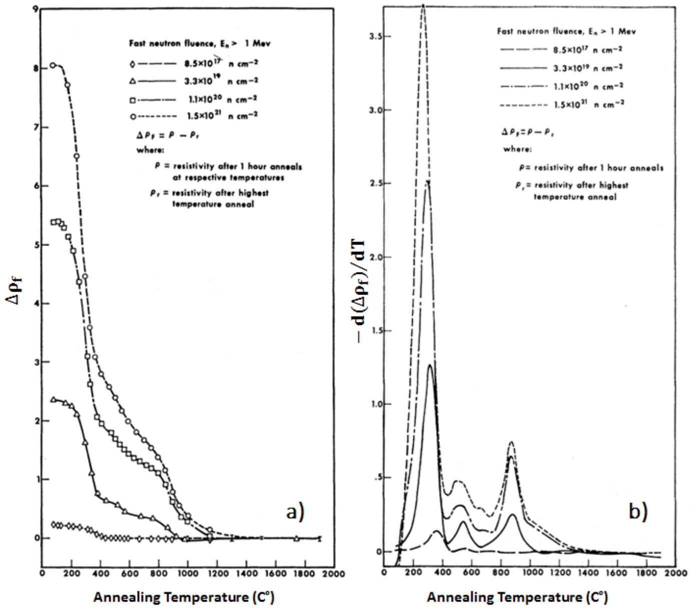

Figure 4.20: *a)* $\Delta\rho_{\text{f}} = \rho(\text{T}) - \rho(\text{T}_{\text{max}})$ *variation compared to annealing temperature for W wires exposed to different neutron fluences. b)* $-\text{d}(\Delta\rho_{\text{f}})/\text{dT}$ *variation compared to annealing temperature for W wires exposed to different neutron fluences. [86]*

Moreover, as anticipated above, the ρ_{film} data can be compared both qualitatively and quantitatively with W ρ thermal annealing results, reported in [86], obtained after having exposed some W wire specimens to a neutron flux for a long time. In [86], particular attention is given to the recovery of defects at different temperatures and some results are reported in figures 4.20a and b: the former reports the variation of $\Delta\rho_{\text{f}} = \rho(\text{T}) - \rho(\text{T}_{\text{max}})$ compared with the annealing temperatures, where $\rho(\text{T})$ is the wire electrical resistivity after 1 hour of annealing at temperature T and $\rho(\text{T}_{\text{max}})$ is the wire electrical resistivity after 1 hour of annealing at maximum temperature. The latter graph reports the variation of $-\text{d}(\Delta\rho_{\text{f}})/\text{dT}$ with regard to the annealing temperatures. It is worth noting that all electrical resistivity measurements were performed after the annealing procedure and at nitrogen liquid temperature. From these graphs it is possible to note that:

- the higher the neutron fluence, the higher $\Delta\rho_{\mathrm{f}}$ and, hence, the higher the number of neutron-induced defects in the specimens (figure 4.20a);
- by increasing the annealing temperature, $\Delta\rho_{\mathrm{f}}$ decreases with a trend similar in the whole specimens exposed to different neutron fluence (figure 4.20a);
- $-\mathrm{d}(\Delta\rho_{\mathrm{f}})/\mathrm{dT}$ exhibit the formation of precise peaks around the typical recovery temperature of W and they typically shift depending on the neutron exposure conditions (figure 4.20b).

Similarly, the electrical resistivity variation in the function of the annealing temperature of c-W and n-w were elaborated to obtain graphs similar to those reported in figures 4.20a and b. The $\Delta\rho = \rho_{\mathrm{film}}(\mathrm{T}) - \rho_{\mathrm{film}}(\mathrm{T}_{\mathrm{max}})$ versus annealing temperature graph of c-W and n-W is reported in figures 4.21a and c, respectively. The $-\mathrm{d}(\Delta\rho)/\mathrm{dT}$ versus annealing temperature graph of c-W and n-W is reported in figure 4.21b and d, respectively. By observing these graphs it is possible to deduce some qualitative conclusions. The trend of $\Delta\rho$ of both c-W and n-W is comparable with that reported in figure 4.20a: this can mean that the behavior of PLD films

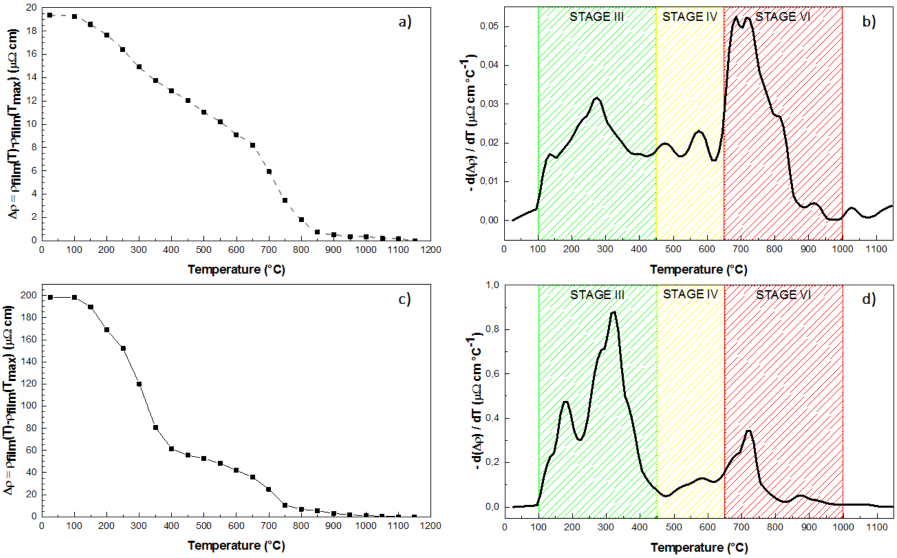

Figure 4.21: *a) $\Delta\rho_{\mathrm{f}} = \rho_{\mathrm{film}}(\mathrm{T}) - \rho_{\mathrm{films}}(\mathrm{T}_{\mathrm{max}})$ variation compared with annealing temperature for c-W. b) $-\mathrm{d}(\Delta\rho)/\mathrm{dT}$ variation compared with annealing temperature for c-W. d) $\Delta\rho_{\mathrm{f}} = \rho_{\mathrm{film}}(\mathrm{T}) - \rho_{\mathrm{films}}(\mathrm{T}_{\mathrm{max}})$ variation compared with annealing temperature for n-W. d) $-\mathrm{d}(\Delta\rho)/\mathrm{dT}$ variation compared with annealing temperature for n-W. To note that W recovery temperature ranges are reported in b) and d) graphs.*

with regard to temperature resembles qualitative similarities to that of neutron-irradiated W wires, even if careful structural analysis must be done to validate this visual hypothesis. Obviously, $\Delta\rho$ is higher for n-W because of its more disordered structure. Moreover, the graphs reported in figures 4.21b and d highlight the presence of defined peaks around relevant recovery temperatures. The relative entity of these peaks is not comparable with that reported in [86], but this can be due to different concentrations of different defect types. To conclude, it is possible to hypothesize that some defects present in c-W and n-W films are also generated by neutrons when they interact with bulk W specimens, but their relative concentration would be different. So, extra investigations in this direction must be performed to clarify this crucial point. Nevertheless, the potentiality of electrical resistivity measurements to qualify the films deposited with particular attention to their defect concentration and the recovery temperatures of these defects was demonstrated .

4.2.3 W-oxide nanowire nucleation

As briefly anticipated in section 4.2.1, the nucleation of tungsten oxide NWs was observed after annealing n-W at relatively low temperatures compared with those that are conventionally selected. Even though this is not one of the main goals of this project, this investigation is extremely interesting in the field of material science and the obtained results make it possible to publish a dedicated paper on this topic [90]. In general, tungsten oxide NWs exhibit unique electronic and electro-chromic properties that make them interesting for applications in many technological fields, such as gas and pH sensing [92], water splitting [104] and field emission [105].

The presence of an O source is essential in growing oxide NWs. In gen-

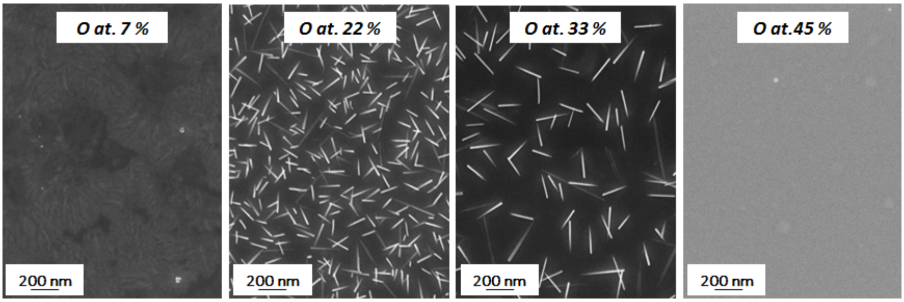

Figure 4.22: *SEM plain view of nano-like W film with different O content thermal annealed at 650° C. The O content in film is pivotal for NWs growth.*

eral, O can either be present in the vacuum chamber as residual gas [106], or it can be added intentionally as O_2 flux [107] or as H_2O steam. As discussed above, n-W can retain high amounts of interstitial O, which is incorporated in the film matrix during the deposition process, where it is present as an impurity, rather than reacting with W at the film surface because of air exposure after deposition, as confirmed by Scanning Auger Microscopy reported in [90]. As discussed in section 4.1.1, it was feasible to make films with the desired O content by calibrating the O_2 contamination opportunely during the deposition process and, moreover, it was observed that the higher the deposition pressure, the higher the O concentration in the film. The trapped O within metallic films is fundamental to making it possible to form tungsten oxide NWs and it establishes the precise temperature range where the NWs nucleation happens. By keeping the annealing temperature constant, O concentration plays a pivotal role in NW nucleation: in particular, as reported in figure 4.22, by selecting an annealing temperature of about 650°C, samples with O that amounts to less than 7% do not show NWs formation. Trapped O between 20% and 35% make it possible to form NWs. On the other hand, higher O content inhibits NWs nucleation.

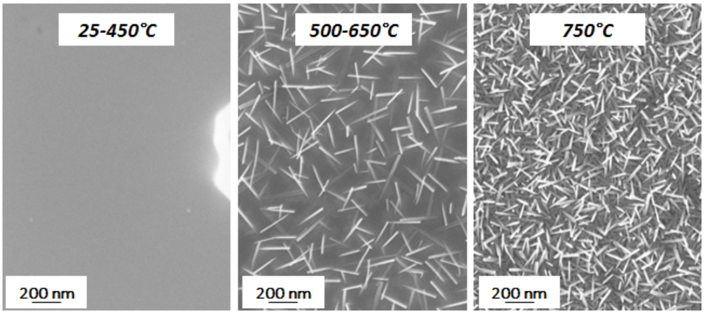

Figure 4.23: *SEM plain view of W film with O content of about 30% thermal annealed at different temperatures. The annealing temperature in film is pivotal for NWs growth.*

In the same way, the role of the annealing temperature is pivotal. In particular, the samples with an O content of about 30% were treated at different temperatures, as reported in figure 4.23. Below 450°C, NW growth does not take place; between 500°C and 650°C, NWs are detected, while a rise in temperature up to 750°C leads to increasing NW density and length. Figure 4.24 shows the cross section view of an area of n-W with an O concentration of about 30% annealed at 650°C, where a consistent NW nucleation takes place.

To conclude, by selecting the film O content and annealing temperature

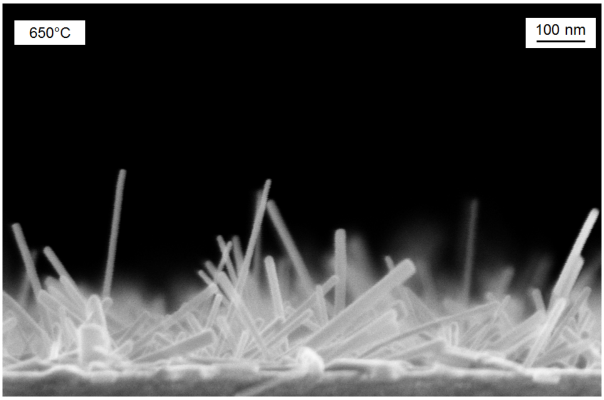

Figure 4.24: *SEM cross section image of NWs grown after vacuum annealing at 650°C of n-W film with an O content of 33.5%.*

properly, it was possible to calibrate the NW nucleation process and, in particular, also the NWs dimensions. It was possible to grow NWs that were 0.85-3.6μm long, with a thickness of between 20 nm and 40 nm. Moreover, the structure of NWs produced either at 500°C or at 650°C was investigated using high-resolution TEM, as reported in figure 4.25. Both structures have a crystalline nature. The NWs grown at 500°C are highly regular and their thickness does not change along the whole length. They show the typical features of the $W_{18}O_{49}$ phase, with a high degree of crystallinity. The NWs grown at 650°C exhibit a different morphology. They are tapered, and thickness increases proceeding from the base to the top. In addition, they are not regular and seem to be polycrystalline, while their crystalline structure has been assessed as monoclinic WO_3.

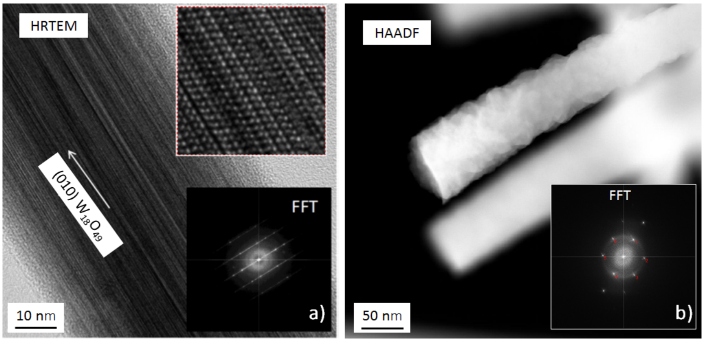

Figure 4.25: *TEM images of NW grown at 500°C that exhibit the* $W_{18}O_{49}$ *structure (a) and 650°C (b) that exhibit the* WO_3 *structure. The corresponding fast Fourier transforms (FFTs) are present in the insets.*

This result is also confirmed by Raman spectroscopy (not reported here).

5

Exposures to divertor-like plasma generators

This chapter focuses on the divertor-like plasma exposures of W-based films whose production and identification has been presented in chapter 4. In general, the aim is to expose films with different properties to similar divertor-like plasma in order to investigate their morphology, structure and elemental composition changes induced by plasma itself. Moreover, the relationship between film properties and the retained deuterium was assessed by using TDS and NRA techniques (see section 3.5) with particular attention given to the role of the oxygen trapped within the film.

Given T radioactivity, laboratory experiments are conventionally performed by using D plasma and this Ph.D. thesis mostly used and investigated pure deuterium plasma exposures (see section 5.1 and 5.2); however, a preliminary exposure toward mixed helium-deuterium plasma was also performed (see section 5.3). In general, tokamak relevant plasma can be generated by using linear devices. Some of these have been described in section 3.4. These machines can work either in a pulsed or steady-state regime by using non-superconductive magnets. In this configuration, pulsed devices are able to produce plasma shots with a precise time duration of a few seconds and with divertor-like high plasma flux ($\approx 10^{24}$ m^{-2}s^{-1}). Therefore, it is possible to reach ITER-relevant fluence ($\approx 10^{26}$ m^{-2}) within tens of shots. On the other hand, steady-state machines work continuously in time, generating a plasma flux of about 10^{22} m^{-2}s^{-1} and it is possible to finely calibrate the total fluence by selecting the exposure time. In general, it is also feasible to reach ITER-relevant fluence with these devices within a few hours of exposure time.

Apart from the plasma flux, which depends on machine configuration, the other plasma parameter can be freely chosen. Since ITER should work in a quasi steady-state regime with high impinging fluxes on the divertor region (see section 1.4), it is evident that present-day plasma generators do not simulate the plasma conditions foreseen in ITER entirely. Therefore, it is fundamental to uncouple the effects due to plasma exposure conditions (e.g. shots or continuous exposures) from those due to the different properties of tested materials.

The samples tested in pure deuterium plasma are discussed on the basis of their nature: metallic-W films (see section 5.1) and W-O films (see section 5.2). Metallic-W films were exposed both to high flux and pulsed deuterium plasma (see section 5.1.1) and low flux and steady-state plasma (see section 5.1.2) with the aim of comparing the results coming from different plasma regimes. Moreover, metallic-W film prompt-outgassing behaviors were investigated by using the so-called Laser Induce Desorption, as reported in section 5.1.3. The W-O systems were studied for various aims. In particular, samples with the same morphology and structure but different oxygen content were exposed to low flux and high fluence deuterium plasma to assess the role of oxygen, which can be naturally present in films, on retained deuterium in films (see section 5.2.1). In section 5.2.2, oxide W films were exposed to high flux and pulsed pure deuterium plasma in order to investigate the modifications induced by plasma on specimens and the changes in deuterium retention due to the oxide nature of samples. A preliminary exposure of relevant coatings to mixed helium-deuterium plasma was performed in PSI-2 and these results are presented in section 5.3. In conclusion, first He-loadings of W-based films were done by using a dedicated ion beam facility at Instituto Superior Técnico (Lisbon, Portugal) in order to have reference samples for validating Laser Induced Breakdown Spectroscopy technique (see section 5.4).

5.1 Deuterium plasma exposures of metallic W films

As described in depth in chapter 2, PFCs suffer in a very harsh environment during ITER operations to the extent that they change properties dramatically. Since the tokamak approach is not sufficient for testing modified materials, laboratory-scale investigations have been developed to fill these gaps. In this thesis, thanks to a versatile deposition technique (PLD), it was possible to make films that have the desired properties and can be proxies of the co/re-deposited layers found in present-day tokamaks and that could be found on ITER PFCs. In light of what was mentioned above, in the next sections, the exposures performed in a pulsed device (PILOT-PSI) of metallic W films are discussed, with particular attention given to morphological modifications induced by plasma itself and the amount of D retained in tested specimens. Then, in order to understand the role of different plasma regimes on material modifications and D retention, selected metallic W films were exposed to PSI-2 plasma that produces a continuous plasma. Then, a selection of samples was tested to study their prompt-outgassing D film behaviors after their exposure to a low flux steady-state plasma.

The sample types selected in these experiments are listed below:

- **columnar-W** (c-W) was selected because it can be a proxy of W-coated first wall installed in JET and AUG, which is made by CMSII: both have a columnar structure and have quite similar grain dimensions [47];
- **nanostructured-W** (n-W) can be a proxy of re-deposited W formed by energetic ions and particles or can be a proxy of highly damaged bulk W by neutron fluxes;
- **porous-W** (p-W) can simulate the re/co-deposited W layers in the shadowed regions of divertor.

In general, as discussed in section 3.2.1, PLD technique makes it possible to set finely the particle energies by changing deposition parameter. Theoretically, by knowing the energy of the ions and particles eroded from PFMs in a tokamak, it is possible to achieve the same conditions in a PLD system and, then, to deposit proxy re/co-deposited layers.

Moreover,as already discussed in section 2.1.1, the PFCs and, then, the re/co-deposited layers, are subjected to extreme thermal loads that modify material properties. In order to simulate re/co-deposits that suffered high temperature regimes, the c-W, n-W and p-W samples were thermal annealed at an ITER-relevant temperature (750°C) in a vacuum condition before the plasma exposures, generating the so-called annealed c-W, annealed n-W and annealed p-W. All samples were deposited on a bulk W substrate. A 150 nm-thick layer of c-W was put between film and W substrate in order to improve their reciprocal adhesion. Finally, bulk W specimens were exposed to D plasmas to have reference data to interpret the different film behaviors. It is worth mentioning that it was not possible to check if co-deposits were formed on each sample as a result of plasma exposure and, then, their possible contribution to the D retention is not taken into account in all D retention measurements reported in this Ph.D. thesis. Moreover, as reported in the following sections, the exposure conditions are similar to each other but not the same, mainly due to technical problems during various plasma exposures; however, in general, the regime was kept constant.

5.1.1 High flux, high fluence, pulsed plasma

The selected samples for this investigation were c-W, n-W and bulk-W. The film thickness was fixed at 1 μm. These films were exposed to D plasma at a low surface temperature ($T_{max} = 250°C$). The electron density and temperature of the plasma were measured by Thomson scattering [5]. The specimens were irradiated with 4 plasma shots of 80s which leads to an average plasma fluence of about $2.5 \cdot 10^{26}$ m^{-2}. The targets were kept at a constant bias of -40 V during the exposures.

Optical microscope images of the samples exposed to D plasma are reported in figure 5.1. Bulk W shows only a few small blisters (figure 5.1a). These blisters probably originate from plastic deformation. Many more and larger blisters are found on the c-W surface (figure 5.1b). These blisters are uniformly distributed and have a typical size of 20-30 μm. On the other hand, n-W exhibits a high number of blisters with a high average size (20-60 μm), which are concentrated at the periphery of the sample (figure 5.1c). The black circles indicate blisters that were burst and delaminated and this results in losing their caps. Figure 5.2 shows in detail a blister that formed and burst on the periphery of n-W. In this case, the blister has a mean dimension of 30 μm (figure 5.2a) and the film deposited

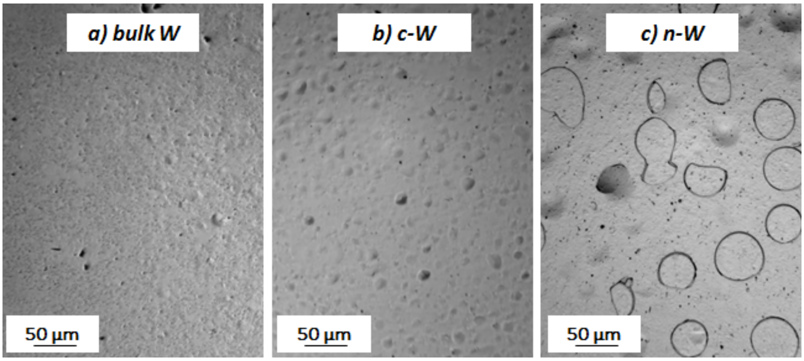

Figure 5.1: *Blister formation on the sample surfaces. a) bulk W, b) 1 μm c-W and c) 1 μm n-W*

on the W substrate was totally removed by the bursting event, underlining that the D accumulation happens between the film layer and the bulk substrate(figure 5.2b).

SEM analyses show the formation of structure at the nano-scale after high-flux plasma exposure (figure 5.3). Grains are evident on the bulk W sample. These grains exhibit different nanostructures (figure 5.3a). The grain in the top of the image shows nanolamellae formation, while the grain in the bottom part shows a triangular-like morphology. The features of these nanostructures strongly depend on the grain orientation, as reported in literature [108]. The nanostructures grown on c-W (figure 5.3b) seem to reflect the grain orientation of the substrate. This results in a precise interface between the triangular-like and nanolamellae structures. The n-W film shows a mixture of randomly oriented nanolamellae (figure 5.3c); this is probably due to a less evident coupling between the film and the substrate, mainly due to the very disordered structure of n-W film.

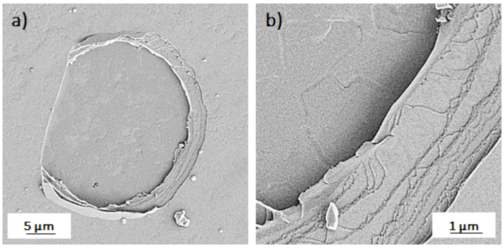

Figure 5.2: *SEM images of a blister formed and burst in the periphery region of n-W sample.*

The D retention was measured by TDS. The results are reported in figure 5.4. The bulk W retains a very small amount of D ($0.9 \cdot 10^{20}$ m^{-2}). On the other hand, c-W film retains much more D and reveals two desorption peaks at 500 K and 700 K. This means that the total D retained increases if the layer disorder is increased; the n-W samples show a large amount of D retained. The 500 K peak increases, while the 700 K peak disappears. In conclusion, the total retention increases by increasing the total number of defects in the film. Moreover, since the fraction of D in the bulk W is very low with regard to the retention in the films, the bulk W substrates barely contribute to the total D retention.

A summary of the obtained results is reported in table 5.1. In general, c-W and n-W samples maintain their overall integrity. Nevertheless, abundant blister formation was found both on the c-W and n-W film sur-

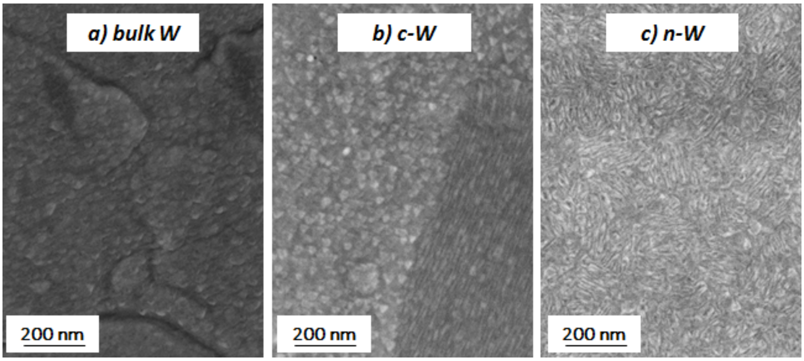

Figure 5.3: *SEM images of nanostructures on the samples' surface after D plasma exposure. a) bulk W, b) 1 μm c-W and c) 1 μm n-W. All these SEM images were acquired in the center of the samples.*

faces. The nanostructures are evident in all samples but their orientation depends on the film features. The D retention was enhanced in the PLD layers, mainly due to their complex structure and morphology. In general, the volumetric D retention in c-W was found to be 1.25 atomic %, which is comparable to saturated values of D retention in pre-damaged bulk W (1.44 at. % [27]). However, the total D retention in the pre-damaged case was found to be $5.4 \cdot 10^{20}$ m^{-2} and the D penetrated only 0.6 μm into the material. This means that the D penetration in the c-W is faster than the penetration into pre-damaged W. The TDS spectrum of n-W shows an important desorption peak at around 500K and the D retention amount is extremely high. This low temperature desorption peak is usually associated with the presence of grain boundaries and dislocations [109]. This is consistent, since the mean crystallite size is about 1 nm and the n-W sample has many grain boundaries that can reasonably trap D. The volumetric D retention of n-W samples was evaluated to be about 5.4 atomic %, but this value can be affected by some errors due to the incorrect evaluation of film mass density that is necessary to be able to extract this value from total D retained in the film.

5.1.2 Low flux, high fluence, steady-state plasma

The selected samples for this investigation were 1 μm-thick n-W, 3.5 μm-thick n-W (named thick-W), 1 μm-thick n-W thermally annealed at 750°C in vacuum atmosphere (named annealed-W) and 1 μm-thick p-W. These films were exposed to a D plasma at a low surface temperature ($T_{\max} = 210$°C). The electron density and temperature of the plasma

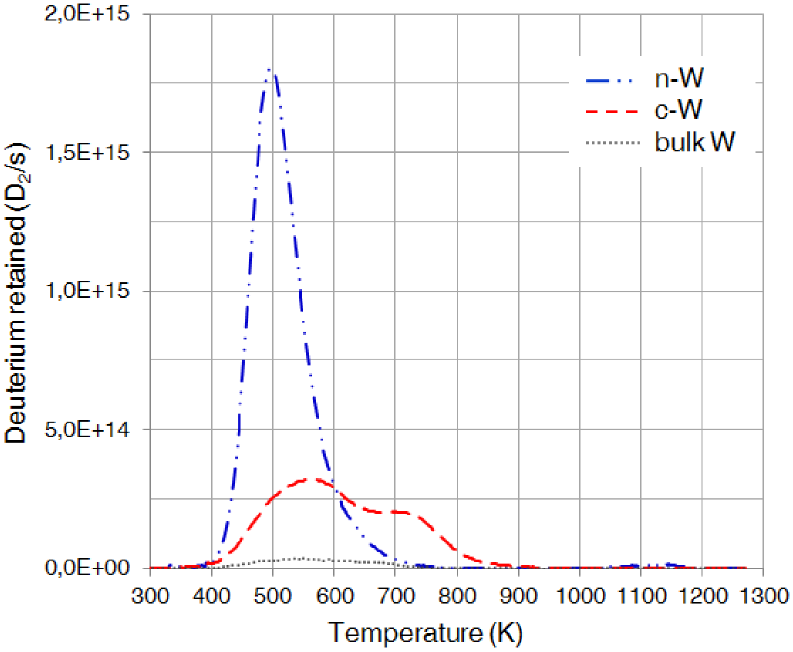

Figure 5.4: *Thermal desorption spectra of bulk W, c-W and n-W exposed to D plasma fluence of* $2.5 \cdot 10^{26}$ m^{-2} *at a low temperature (250° C).*

were estimated by a Langmuir probe. The specimens were exposed to steady-state plasma with a mean flux of about $1.3 \cdot 10^{22}$ m^{-2}s^{-1} for different exposure-times in order to test samples in different fluence regimes. Hence, the total plasma fluence ranged from $4.0 \cdot 10^{24}$ m^{-2} (5 minutes of plasma exposure) to $1.0 \cdot 10^{26}$ m^{-2} (4 hours of plasma exposure). The targets were kept at a floating bias.

SEM analyses of thick-W and n-W samples exposed to different fluence D plasma are reported in figure 5.5 and 5.6, respectively. They both show the formation of structures at the nano-scale after each plasma expo-

	bulk W	**c-W**	**n-W**
crystallite size	≈ μm	≈ 14 nm	≈ 1 nm
blisters	few none burst	uniform none burst	periphery often burst
nanostructure	grain dependent	grain dependent	mixture
D retention	$8.6 \cdot 10^{19}$ m^{-2}	$9.6 \cdot 10^{20}$ m^{-2}	$2.1 \cdot 10^{21}$ m^{-2}

Table 5.1: *Summary of the results obtained from Pilot-PSI exposures at fluence of* $2.5 \cdot 10^{26}$ m^{-2} *of bulk W, c-W and n-W specimens.*

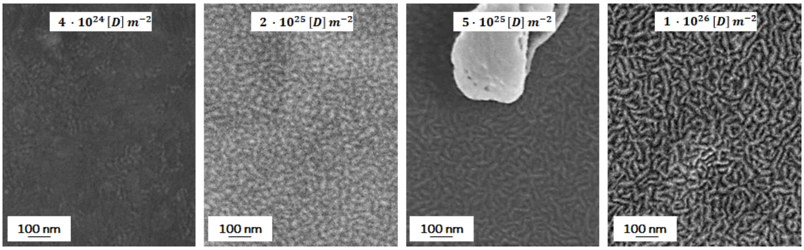

Figure 5.5: *SEM images of nanostructure formation on thick-W surface.*

sure. In particular, these structures start to form at the lowest exposure fluence, then, by increasing the D plasma exposure time, they become more evident. At the maximum fluence ($1.0 \cdot 10^{26}$ m^{-2}), the formation of nanolamellae is evident and is similar to what occurs for high-flux and pulsed plasma exposures done in PILOT-PSI device. Since n-W and thick-W films do not have a preferential grain orientation, they show a mixture of randomly oriented nanolamellae; this is probably due to a less evident coupling with the substrate.

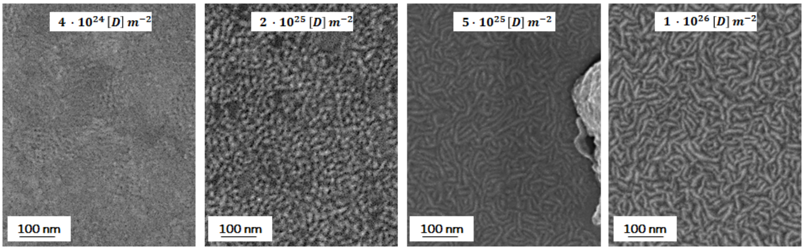

Figure 5.6: *SEM images of nanostructure formation on n-W surface.*

SEM analyses also confirm also the formation of burst blisters both on the thick-W and n-W (figure 5.7), as in the case of high-flux and pulsed plasma exposures. In particular, thick-W highlights large blister formation at a relatively low plasma fluence ($2.0 \cdot 10^{25}$ m^{-2}) that becomes larger and larger as exposure time increases. On the other hand, n-W shows blister formation only at the maximum plasma fluence ($1.0 \cdot 10^{26}$ m^{-2}). Figure 5.7a reports a blister that was found on the thick-W surface after the exposure at $2.0 \cdot 10^{5}$ m^{-2}; it has a mean diameter of about 40 μm. It has been observed that, by exposing samples to the maximum D plasma fluence, blisters can reach a mean diameter of about 100 μm. From figure 5.7b, which reports a detail of this blister, it is possible to conclude that the film deposited on W substrate is totally removed by the bursting event, pointing out that the D accumulation happens between the film layer and the bulk substrate. Figure 5.7c shows a blister formed on n-W after exposure to the maximum D plasma fluence. Its mean diameter is about 10 μm. The difference in blister dimensions for the thick-W and n-W could be due to their different thicknesses: since thick-W is 3.5 times thicker than n-W, it can potentially accumulate a higher amount of D in the interface between film and substrate because it can better accommodate the stresses produced by D accumulation and, therefore, it makes it possible to form larger blisters.

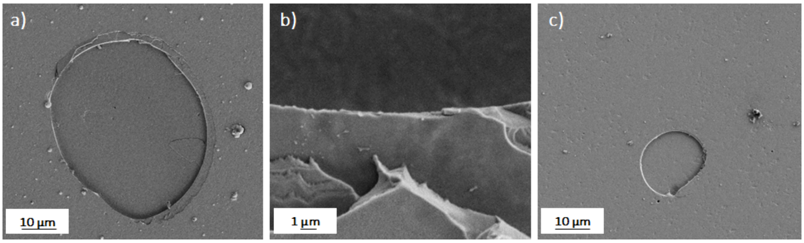

Figure 5.7: *SEM images of blister formation on a) the thick-W and b) the n-W. c) A detail of the thick-W blister is reported.*

SEM analyses of p-W samples exposed to different D plasma fluences are reported in figure 5.8. The behavior of the p-W sample with regard to increasing-time exposures to D plasma is peculiar; it is possible to observe from figure 5.8 that, at the lowest fluence $4.0 \cdot 10^{24}$ m^{-2}, the crack network is well-defined, while by increasing exposure time, the number of cracks and their dimensions decrease as though there were a recovery process. This unique behavior can be ascribed to p-W features. As described in section 3.4, the sample temperature in the PSI-2 device is monitored by a thermocouple which is put on the back side of the sample holder. p-W has an open morphology, with a porous structure, and exhibits high amounts of O trapped within the film matrix. Due to these peculiar properties, its thermal conductivity can be extremely low, causing the system to experience higher surface temperatures that can produce the peculiar recovery process discussed before. Moreover, there is no formation of blisters.

Figure 5.9 shows SEM analyses of annealed W exposed to different D plasma fluences. There are no evident changes up to a D plasma fluence of $2.0 \cdot 10^{25}$ m^{-2}. For higher fluences, as in the case of thick-W and n-W, the nanolamellae formation takes place and their orientation reflects those of film grains. Blisters are not found on these sample surfaces.

The D retention was measured by NRA. In particular, NRA makes it possible to measure both retained D atoms in film layers and W atoms. Therefore, it is possible both to estimate the total retained D in the film

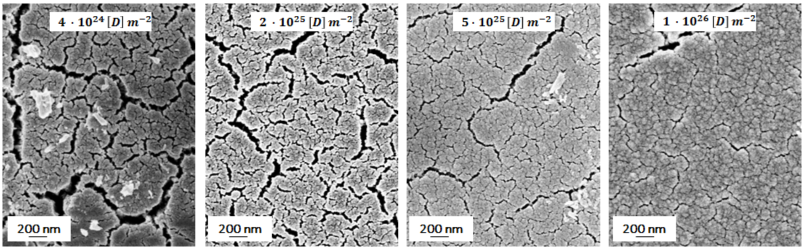

Figure 5.8: *SEM images of modifications induced on p-W surface.*

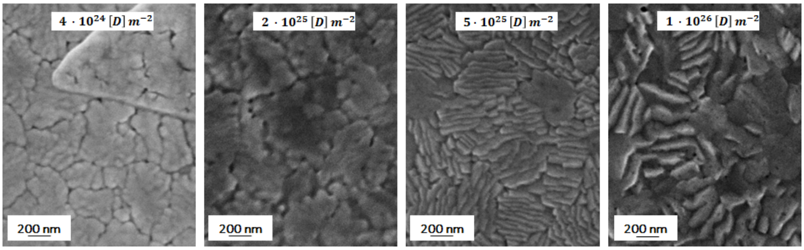

Figure 5.9: *SEM images of nanostructure formation on annealed-W surfaces.*

and the ratio between D and W. The former value is the same as that achievable with TDS analyses. The latter is also obtainable with TDS measurements but, in this case, it is necessary to know precisely both the film thickness and its mass density. As discussed in the previous section, the mass density of n-W is not so easy to obtain, mainly due to the unique deposition conditions in which n-W are made. By exploiting NRA measurements, D/W ratio is achievable. In general, the D/W ratio has a saturation value that depends on the layer type (e.g. morphology, structure and defect concentration) and plasma condition (e.g. temperature, flux and fluence) [27]. In particular, it was found that the D retained in self-damaged W at 0.45 dpa, when exposed to a D plasma similar to that described in the previous section, is 1.44 atomic % near the specimen surface and, then, it decreased going deeper into the sample due both to a self-shielding effect [110] and the depth profile produced with self-implantation itself. As already discussed in section 3.5.2, the NRA results of this thesis are not resolved with regard to film depth and indicate a mean value. In addition, PLD films used in this thesis have homogeneous properties with regard to their thickness.

The results with regard to D plasma fluence variation are reported in figure 5.10. In particular, figure 5.10a highlights the variation of the D/W ratio. From this graph, it is possible to observe that:

- the D/W ratio does not change if the plasma fluence is lower than $2.0 \cdot 10^{25}$ m^{-2}, while, for higher plasma fluence regimes, the D/W ratio increases;
- the maximum value of the D/W ratio strongly depends on film properties;
- only thick-W and n-W achieve the saturation ratio, with a value of about 1.25 at. %.

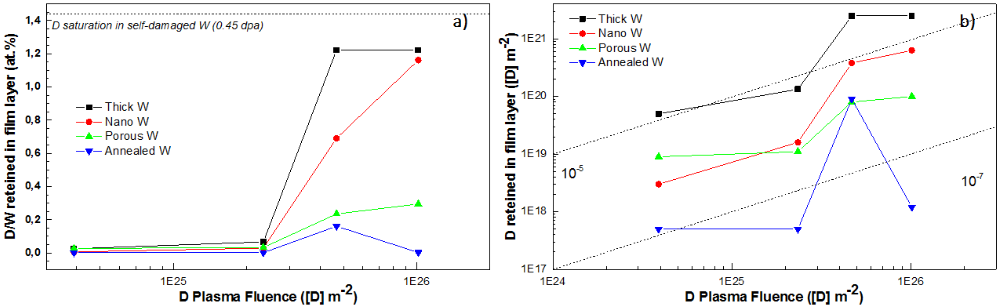

Figure 5.10: *a) D/W ratio with regard to D plasma fluence. b) Total D retained with regard to D plasma fluence.*

On the other hand, figure 5.10b reports the variation of the total retained D with regard to the total plasma fluence experienced by samples. It has been demonstrated that only a small fraction of the impinging plasma flux can penetrate and, then, be retained in the exposed material. For the bulk W case, this fraction ranges between 10^{-5} and 10^{-7} [110] and strongly depends on exposure conditions. The graph reported in figure 5.10b reports these limits and the D retention values of each film type are included in these limits.

Moreover, by analyzing the NRA spectra, it was possible to evaluate the fraction of D retained in film substrates: this quantity is very low with regard to the retention in the layers, therefore the bulk W substrates barely contribute to the total retention.

Since thick-W and n-W samples have the same properties but different thickness, it has been interesting to evaluate their D saturation behavior: the ratio between the total D retained in thick-W and n-W samples ($D_{\text{thick}-W}/D_{n-W}$) is plotted with regard to plasma fluence in figure 5.11a. Since the ratio between their thickness is about 3.5, it is reasonable to hypothesize that $D_{\text{thick}-W}/D_{n-W}$ should be 3.5, if the saturation condition is satisfied in both samples. From the graph reported in figure

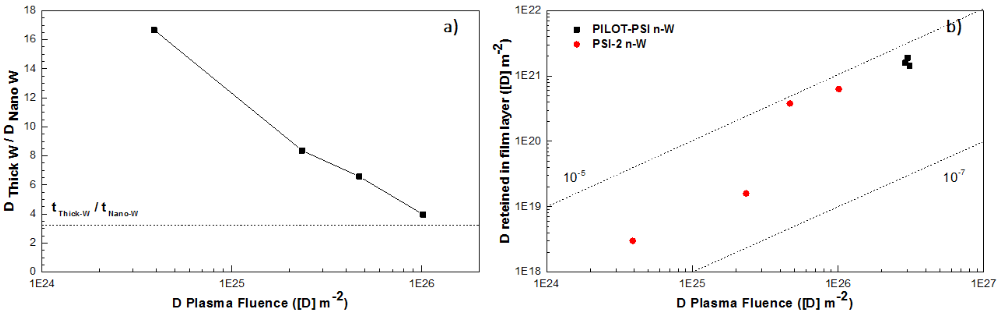

Figure 5.11: *a)* $\mathrm{D}_{\mathrm{thick-W}}/\mathrm{D}_{\mathrm{n-W}}$ *with regard to D plasma fluence. b) D retention results of samples exposed to PSI-2 (red circles) and those exposed to PILOT-PSI (black squares).*

5.11a, it is possible to observer that, when the D plasma fluence is low, $\mathrm{D}_{\mathrm{thick-W}}/\mathrm{D}_{\mathrm{n-W}}$ has a high value that means that D retained in thick-W is much more than that retained in n-W. Probably, this is due to thick-W having a higher number of sites where D can be retained because of its higher width. For this reason, it is possible to suppose that, since the available surface for both samples is the same, the D penetrates faster in the case of thick-W, driven by a more efficient D concentration gradient, also helped by the uniform defect concentration of these PLD films. Nevertheless, $\mathrm{D}_{\mathrm{thick-W}}/\mathrm{D}_{\mathrm{n-W}}$ decreases linearly with plasma fluence until it reaches the saturation value of about 3.5, which is reached at the maximum plasma fluence.

	thick-W	**n-W**	**p-W**	**annealed-W**
crystallite size	1 nm	1 nm	7 nm	20 nm
blisters	few	few	none	none
O content	20 at. %	20 at. %	55 at. %	0 at. %
nanostrucutre	mixture	mixture	none	grain dependent
D retention	$2.5 \cdot 10^{21}\ \mathrm{m}^{-2}$	$6.3 \cdot 10^{20}\ \mathrm{m}^{-2}$	$1.0 \cdot 10^{20}\ \mathrm{m}^{-2}$	$1.8 \cdot 10^{18}\ \mathrm{m}^{-2}$

Table 5.2: *Summary of the results obtained from PSI-2 exposures at the maximum ITER-relevant fluence of about* $1.0 \cdot 10^{26}\ \mathrm{m}^{-2}$ *of thick-W, n-W, p-W and annealed-W specimens.*

To conclude, in figure 5.11b, all D retention results, obtained from samples exposed both to PILOT-PSI D plasma and PSI-2 D plasma, are reported. It is possible to note that the two campaign results are consistent with each other; this indicates that, in the temperature regime selected for these experiments, D retention is not affected strongly enough by D plasma flux regime but is deeply correlated with the total fluence that can be achieved during exposure. Moreover, as illustrated in this section, the morphological modifications induced by high flux plasma (PILOT-PSI) and lower plasma flux (PSI-2) are comparable even if those caused by high flux plasma can be more severe.

To summarize, the D retention results and morphological modifications, concerning the exposure conducted at the highest plasma fluence, are reported in table 5.2 for each sample type. By comparing these results with those reported in the previous section, it is possible to observe that:

- the D retention value of n-W is similar to that measured after D plasma exposure in PILOT-PSI;
- the thick-W sample retains 3.5 time more than n-W; this indicates that both films have reached the saturation condition;
- the p-W retains less D than n-W; this is probably due to its bad thermal conductivity and, for this reason, the temperatures that it has experienced during exposure are higher than those measured by thermocouple;
- annealed-W retains very low amounts of D that are similar to those of bulk W. This can mean that thermal annealing at 750°C makes it possible to recover an important part of sites/defects where D can be retained.

Nevertheless, as highlighted in table 5.2, all samples have very different properties, in particular different crystallite dimensions and different O concentrations. It is natural to plot total retained D in films after the highest fluence exposure versus both O concentrations and crystallite dimensions. These graphs are reported in figures 5.12a and b, respectively. It is quite evident that a correlation between D retained and mean crystallite dimensions of the film exists, while there is not an obvious dependence between retained D and O concentration in the film. This preliminary result is very interesting because D retention seems to be correlated in depth with material micro- and nanostructure while the presence of some impurities has some effects on D retention, but this dependence must be further investigated.

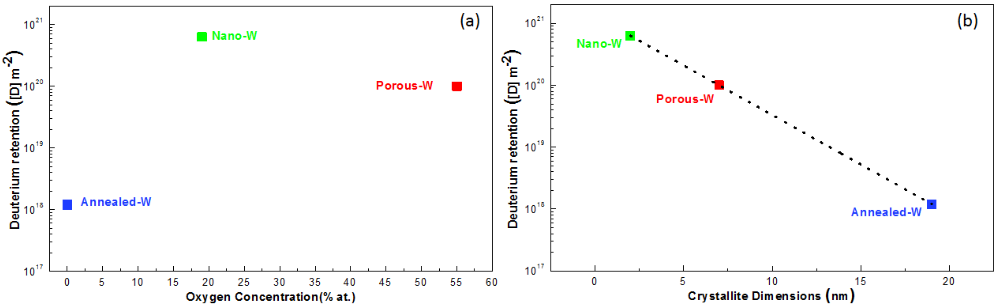

Figure 5.12: *a) Retained D in n-W, p-W and annealed after the highest fluence plasma exposure versus O concentration in films. b) Retained D in n-W, p-W and annealed after the highest fluence plasma exposure versus film mean crystallite dimensions.*

5.1.3 Laser Induced Desorption to study prompt-outgassing film behaviors

In general, it is worth noting that reported D retention values are referred to the D atoms that are strongly retained within the exposed material. Typically, when the plasma is shut down, a part of the retained D is promptly released because some D atoms can be trapped in very low energy traps or near the sample surface. Therefore, the investigation of this topic, regarding the outgassing dynamic of D from different W-based materials, is fundamental. This investigation was performed by exposing different metallic-W samples to low flux D plasma: p-W (both annealed in vacuum at 750°C and not), n-W (both annealed in vacuum at 750°C and not) and bulk W. The D plasma had a flux of about $7.0 \cdot 10^{21}$ m^{-2}s^{-1} and a fluence of about $5.0 \cdot 10^{25}$ m^{-2}. The samples reached a temperature of 300°C during plasma exposure and the bias voltage was kept floating. After the plasma exposure, the samples were moved to a dedicated vacuum chamber where a quadrupole mass spectrometer (QMS) is installed. The D out-gassing was forced by ablating the material with a ms laser beam and the released D was measured by the QMS: this is the basic outline of the Laser Induced Desorption (LID) technique. 5 laser shots were focused on each sample at different times to collect the QMS signals. These QMS signals can be analyzed by extracting the total electrical charge accumulated by the spectrometer after each laser shot. Moreover, it is possible to hypothesize that the prompt-desorption rate is written as follows:

$$\mathrm{D_{rate}} = \mathrm{C}t^{-\alpha} \tag{5.1}$$

where C is a constant, t is the time after the end of the exposure and α is the so-called *out-gassing parameter*. By exploiting this procedure, the α

is obtained for bulk-W, p-W, annealed p-W and annealed n-W. It was not possible to obtain data from n-W because the released D after each laser shot was out of QMS range. This is totally in accordance with the results discussed in the previous section, where it was demonstrated that n-W is able to retain a lot of D due to its unique features. The other out-gassing parameters are reported in figure 5.13.

The result of bulk W is totally in accordance with the literature value.

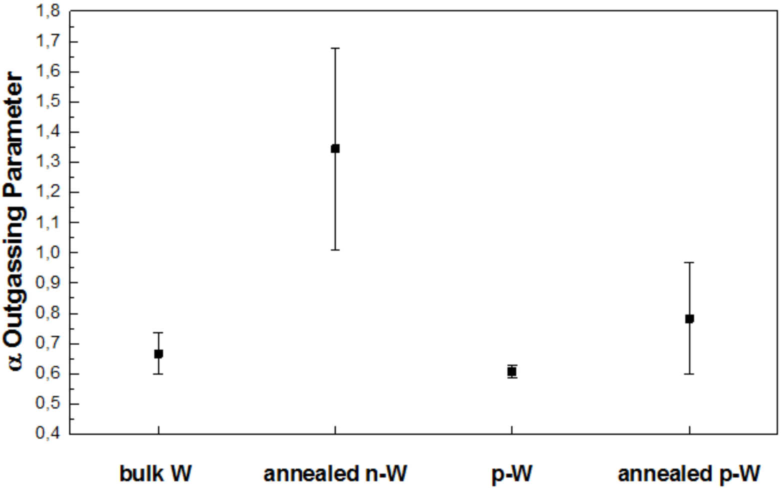

Figure 5.13: *Out-gassing parameters of different W films obtained with LID technique.*

In the case of p-W, α is comparable with the out-gassing parameter of bulk W. In the cases of n-W and annealed p-W, α is greater than that of bulk W; this means that the released D just after plasma shutdown is lower with regard to the bulk W and, then, this can be a problem for fuel management in future fusion tokamak reactors. These results are preliminary and further investigations must be performed to study this topic, which is of extreme interest.

5.2 Deuterium plasma exposure of W-O films

As described in section 2.1.3, tokamak layers can co-deposits together with impurities present in the tokamak environment (e.g. O). In section 4.1.2, the possibility of controlling the O content in films was discussed. By exploiting this possibility, modified n-W samples were deposited with different amounts of trapped O (**O loaded n-W**). These films were exposed to D plasma to assess the role of O during plasma exposures (see section 5.2.1). Once this information had been obtained, oxide W films were studied after their exposure to high flux pulsed D plasma generated by the MAGNUM-PSI device (see section 5.2.2) All samples were deposited onto a bulk W substrate. A 150 nm-thick layer of c-W was put between the film and W substrate in order to improve their reciprocal adhesion. Finally, bulk W specimens were exposed to D plasmas to have reference data to interpret the different film behaviors.

5.2.1 The role of oxygen on retained deuterium in films

As introduced above, it is fundamental to understand the role of O contamination with regard to D retention in films that have almost the same morphology and structure. In section 4.1.2, the possibility of depositing films with the same morphology and different O content has been shown. In particular, n-W and modified O-loaded n-W films were exposed to D plasma generated by the PSI-2 device. The plasma flux was about $6.9 \cdot 10^{21}$ $\mathrm{m^{-2}s^{-1}}$ and the total fluence was about $1.0 \cdot 10^{26}$ $\mathrm{m^{-2}}$ after 4 hours of exposure. The temperature was 300°C. Exposed samples were: n-W and modified O-loaded n-W films deposited in different flux O_2 contamination (2.5, 5 and 10 %). The first row of figure 5.14 shows the plain view of as-deposited samples. It is possible to note that, apart from the presence of some growth defects induced by the O contamination, the surface morphologies are similar. After plasma exposures, the whole samples exhibit nanolamellae formation that is consistent with typical morphological modifications of n-W induced by pure D plasma exposure.

NRA was used to determine the D retained in films. Results are reported in figure 5.15. It is possible to note that D retention is approximately the same for all exposed samples. In particular, n-W and modified O-loaded n-W films deposited with O_2 flux contamination of 2.5 and 5 % have totally comparable D retention values, while the sample made with the highest O_2 flux contamination has a slightly higher D retained amount. For comparison, the retained D in c-W is reported in figure 5.15. It is possible to observe that this value is lower than those of the other films, but, as said before, this is mainly due to its different nanostructure (i.e. mean crystallite dimensions). Therefore, it is possible to conclude that, as hypothesized in the previous section, the amount of retained D in films strongly depends on film nanostructure, while the dependence of O contamination appears not to exist or to make a negligible contribution.

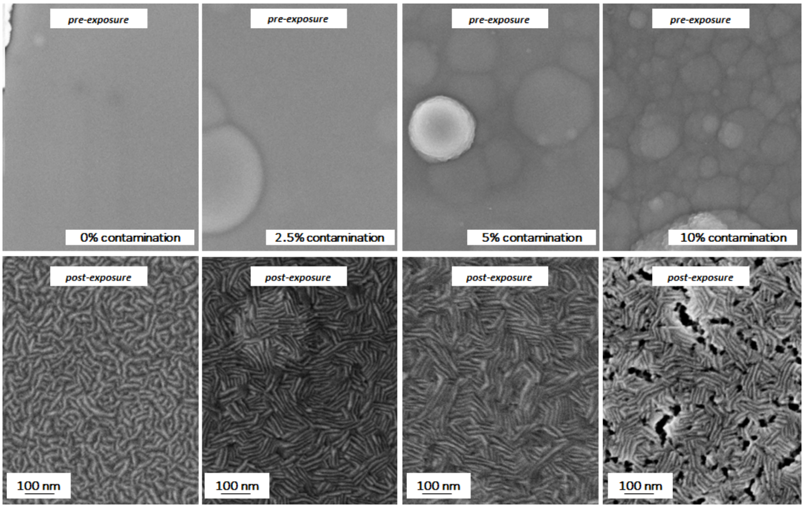

Figure 5.14: *First row: as-deposited film plain view; the morphology is almost the same, for less than some growth defects due to the presence of* O_2 *contamination. Second row: after exposures film plain view; the morphological modifications induced by D plasma are the same for all films and these modifications are consistent with the results obtained for n-W film.*

5.2.2 High flux and pulsed regime exposures of W oxide films

As discussed in detail in section 2.3.3, co-deposited oxide layers have been found on PFMS in present-day tokamaks [57, 60]. Therefore, it is fundamental to understand the behavior of these materials when faced to D plasma. In section 4.1.2, PLD has been used to deposit very interesting W-O systems: in particular, the compact a-WO_3 film was defined as the reference film to be exposed to D plasma in the MAGNUM-PSI device. The plasma flux in the center of the sample was about $1.0 \cdot 10^{24}$ $m^{-2}s^{-1}$ and the total fluence was varied by changing the plasma shoot number. These specimens were tested both in low temperature (LT) exposures ($\approx 300°C$) and in high temperature (HT) exposures ($\approx 600°C$). During all plasma exposures, the targets were kept at a floating voltage.
The selected samples are the following:

- 1 μm-thick compact a-WO_3. This film type was exposed both to LT and HT plasma at a fluence of about $1.0 \cdot 10^{26}$ m^{-2};
- 100 nm of compact a-WO_3 deposited on 900 nm of c-W. This film type was exposed to LT plasma at a fluence of about $1.0 \cdot 10^{26}$ m^{-2};
- 50 nm of compact a-WO_3 deposited on 500 nm of c-W. This film

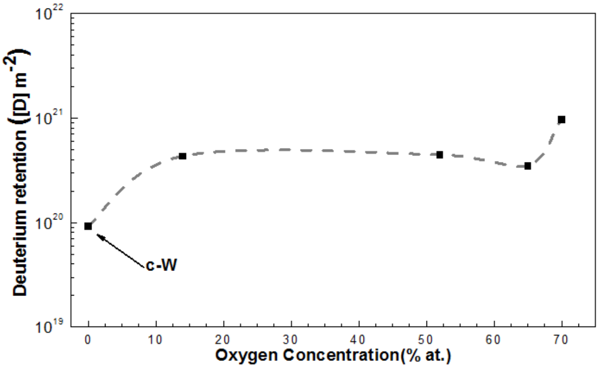

Figure 5.15: *a) Retained D in n-W and modified O-loaded n-W films after plasma exposure with regard to as-deposited O concentration in films. For comparison the retained D in c-W is reported.*

type was exposed to LT plasma at different fluence regimes(from $9.3 \cdot 10^{24}$ m^{-2} to $2.1 \cdot 10^{26}$ m^{-2});

- 1 μm-thick compact c-W. This film type was exposed both to LT and HT plasma at a fluence of about $1.0 \cdot 10^{26}$ m^{-2} and was used as the reference sample to compare results from oxide systems.

Figure 5.16 reports surface morphological modifications of 1 μm-thick compact a-WO_3 that are induced by LT D plasma exposure. It is evident that oxide film is still present after the plasma exposure. There are no film delaminations, blister formation or cracks, but point-like features are present on the film surface after exposure. Figure 5.17 reports sur-

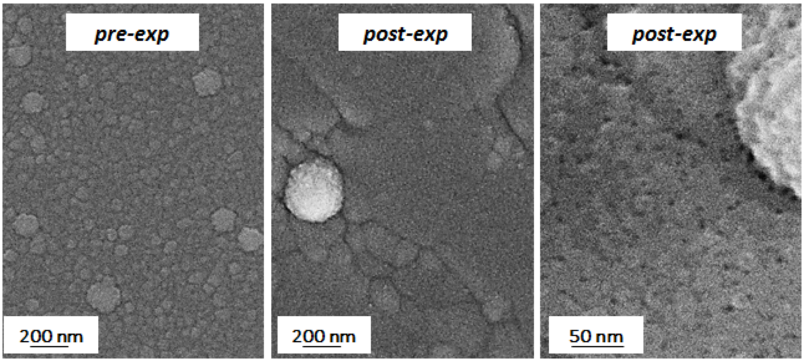

Figure 5.16: *SEM plain views of 1* μm*-thick compact a-*WO_3 *before and after its exposure to LT high flux (*$1.0 \cdot 10^{24}$ m^{-2}s^{-1}*) and high fluence (*$1.0 \cdot 10^{26}$ m^{-2}*) D plasma in MAGNUM-PSI.*

face morphological modifications of 1 μm-thick compact a-WO_3 that are induced by HT D plasma exposure. It is evident that oxide film is still present after the plasma exposure. There are no film delaminations or blister formations but crack network and point-like features are present on the film surface after exposure.

After each D plasma exposure, oxide films were characterized by using EDXS technique and Raman spectroscopy to assess their elemental composition and stoichiometry, respectively. These results are reported in figure 5.18a and b for both temperature exposures.

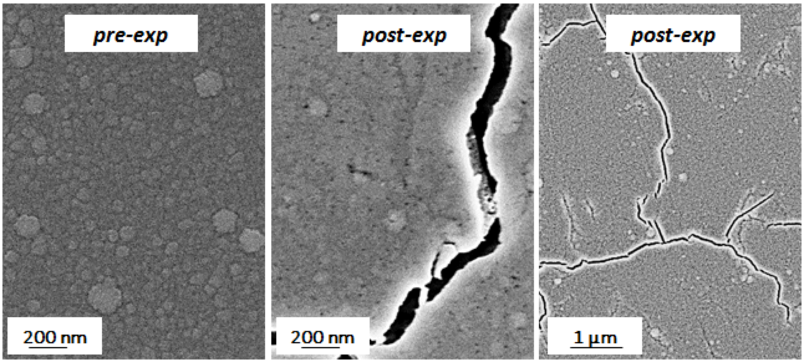

Figure 5.17: *SEM plain views of 1* μm*-thick compact a-*WO_3 *before and after its exposure to HT high flux* $(1.0 \cdot 10^{24}\ \mathrm{m}^{-2}\mathrm{s}^{-1})$ *and high fluence* $(1.0 \cdot 10^{26}\ \mathrm{m}^{-2})$ *D plasma in MAGNUM-PSI.*

In the graph reported in figure 5.18a, the ratio O/W with regard to the sample's position is reported; it is worth noting that only a part of the sample was directly exposed to plasma because of the samples' clamping system design that shadows the external part of the sample. Due to this configuration, this external part experienced only the temperature effects and not those induced by D plasma flux and, therefore, can be used as a control value. Moreover, in the graph the O/W data obtained after thermal annealing treatments performed at various temperatures in vacuum conditions (as discussed in section 4.2.1) are also indicated. It is possible to note that the combined effect of D plasma flux and exposure temperatures leads to O loss that is more evident than those observed after vacuum thermal annealing, both in LT and HT exposures. As a matter of fact, the O loss is enhanced by the presence of D plasma, which can chemically react with O present on film surfaces. This phenomenon can have a double effect: the former is to reduce O content in films that are exposed and the latter is to have a lower effective impinging plasma flux on sample surfaces because of these chemical reactions that can remove some D atoms from plasma flux.

The O loss is also confirmed by Raman spectra, which are reported in figure 5.18b: in both cases, the compact a-WO_3 becomes more amorphous. As a matter of fact, the related Raman spectrum is very broad and it is impossible to discern the bands of compact a-WO_3 discussed in section 4.1.2. However, in the case of HT exposure, it is possible to observe the presence of a sharp peak centered around a typical position of those of the monoclinic WO_3. This result partially confirms what is observed after thermal annealing treatments: in particular, after thermal annealing at 600°C, a-WO_3 film becomes a monoclinic WO_3 film. Therefore, it is possible to conclude that, also in this case, the temperature regime would bring the system to the monoclinic WO_3 phase but the presence of the D plasma makes the situation more complex, and this results in having an extremely amorphous WO_3 in both plasma temperature conditions with few monoclinic domains if the exposure temperature is enough. The multilayer sample composed of 100 nm of compact a-WO_3 deposited on 900 nm of c-W (900 c-W + 100 a-WO_3) was exposed in the same LT plasma condition. The morphological, elemental composition and stoichiometry changes, not reported here, are the same as those found in 1 μm-thick compact a-WO_3 film exposed to LT plasma.

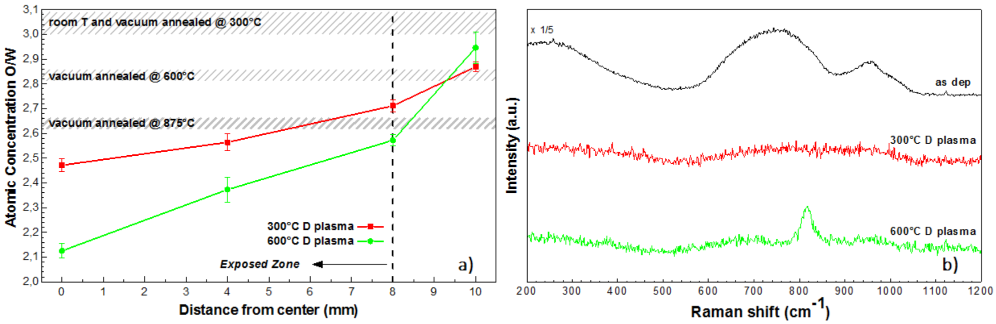

Figure 5.18: *a) EDXS results after 1 μm-thick compact a-WO_3 exposure to both HT and LT high flux ($1.0 \cdot 10^{24}$ m^{-2}s^{-1}) and high fluence ($1.0 \cdot 10^{26}$ m^{-2}) D plasma in MAGNUM-PSI. The results obtained from thermal vacuum annealing are reported in the graph. b) Raman spectra after the 1 μm-thick compact a-WO_3 film exposure to both HT and LT D plasma.*

The c-W samples exhibit the same changes that have been discussed in the first part of this section and, as discussed above, these films were exposed only in order to have reference data.

The retained D was assessed by using TDS in the same configuration as described above. The total D retained after LT plasma exposures in all film types are reported in figure 5.19 and in table 5.3. In general, the D

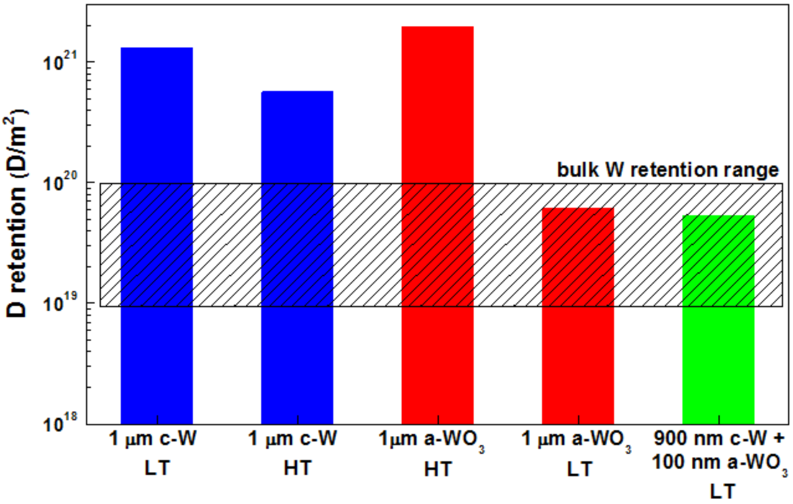

Figure 5.19: *D retained in 1 μm-thick compact a-*WO_3 *and c-W exposed to high flux and high fluence D plasma in different temperature regimes: high temperature (HT, 600° C) and low temperature (LT, 300° C). D retained in multi-layer film composed by 900 nm of c-W and 100 nm of compact a-*WO_3 *exposed to LT d plasma.*

retained in 1 μm-thick compact a-WO_3 film exposed to LT plasma is lower than D retained in c-W film exposed to the same plasma conditions. A possible interpretation is that O naturally present in the a-WO_3 interacts with D plasma: in particular, this process leads to forming heavy water molecules (HDO and H_2O) during exposure. This contributes both to creating a superficial O depleted layer and having a lower D impinging flux on the sample. Post-exposure Raman spectroscopy analysis, reported above, confirms that D plasma exposures lead to oxide amorphisation and O loss phenomena. Moreover, the D mobility is low in these temperature regimes, and a saturated D layer is probably formed in the superficial part of the O-depleted layer of the sample that works as a *barrier* layer.

In the case of HT exposures, retained D in the a-WO_3 film is higher than retained D in c-W film. This is probably due to oxide dissociation driven by exposure temperature, as discussed above and in section 4.2.1, which leads to having a more *metallic* film during exposure. This leads to having a larger active volume where the D can be retained without the formation of superficial localized O-depleted layer that can work as a *barrier* layer to retention.

However a very interesting result was obtained from the multi-layer system: as a matter of fact, the retained D in this film type is lower than

	1 μm c-W	**1 μm a-WO3**	**900 nm c-W + 100 nm a-WO3**
LT plasma (300° C)	$1.3 \cdot 10^{21}$[D]m^{-2}	$6.1 \cdot 10^{19}$[D]m^{-2}	$5.4 \cdot 10^{19}$[D]m^{-2}
HT plasma (600° C)	$5.7 \cdot 10^{20}$[D]m^{-2}	$2.0 \cdot 10^{21}$[D]m^{-2}	-

Table 5.3: *D retained in different W-based films exposed to pure D plasma in HT and LT regime.*

retained D in both c-W and a-WO_3 films.

Driven by these observations, similar systems, constituted by 50 nm of compact a-WO_3 deposited above 500 nm of c-W, were made and exposed to LT pure D plasma in different fluence regimes. In particular, plasma fluence was varied from $9.3 \cdot 10^{24}$ m^{-2} to $2.1 \cdot 10^{26}$ m^{-2}. Morphological changes are the same as those discussed in the previous sections. On the other hand, the elemental composition and stoichiometry changes deserve to be discussed. In figure 5.20a, the O/W variation with regard to the plasma fluence is reported. In figure 5.20b, Raman spectra of samples exposed to different plasma fluences are reported. From EDXS results, it is clear that the interaction between oxide films and D plasma deeply changes the elemental composition of the films: in particular, it is evident that just low D plasma fluence induces relevant O losses. Moreover, three different W/O stages can be recognized with regard to D plasma fluence. The presence of these amorphization stages is also confirmed qualitatively by Raman spectra, as reported in figure 5.20b.

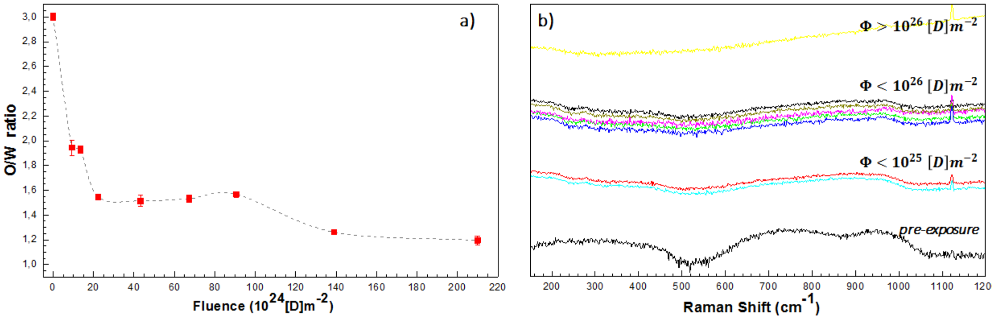

Figure 5.20: *a) The O/W variation with regard to D plasma fluence of multi-layer samples made of 500 nm of c-W and 50 nm of compact a-WO_3. b) Raman spectra of multi-layer films exposed to different D plasma fluence regimes.*

D retention was evaluated by using TDS technique, and the obtained data is reported in figure 5.21. It is evident that retained D in multi-layer

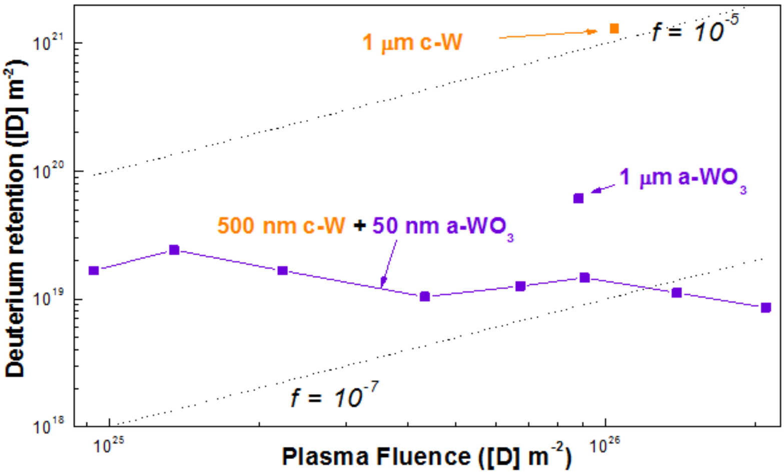

Figure 5.21: *Total retained D in multi-layer system composed of 50 nm of compact a-*WO_3 *deposited on 500 nm of c-W. The retained D values of 1 μm-thick compact a-*WO_3 *and μm-thick c-W exposed to the same D plasma are reported.*

systems seems to be independent from D plasma fluence. Moreover, D retention values of multi-layer systems are lower than those of 1 μm-thick compact a-WO_3 and c-W exposed to the same D plasma. As discussed above, one possible interpretation is that the 50 nm of compact a-WO_3 forms a sort of passivation layer because of the effects induced by the interaction between D plasma and O present in the film and the resulting O loss from the multi-layer system itself. However, it is necessary to note that during the interaction between the oxide layer and the D plasma, heavy water molecules can be created; some can be released during the exposure, while others can be retained. Unfortunately, the TDS system used in this investigation was not able to quantify these contributions: for this reason, the D retention values reported here can underestimate the real D retained in films.

5.3 First results from mixed D-He plasma exposures

Finally, since D-T fusion nuclear reaction produces He, the foreseen ITER plasma has a small percentage of He. Moreover, ITER, after a first demonstrative H plasma, should operate in pure He plasma. For these reasons, preliminary exposure in mixed He-D plasma of metallic W films was done in PSI-2: the focus is on the material modifications due to the presence of He. This is a hot topic and there is a lot of literature on the modifications induced by He plasma on bulk W specimens [111, 112]. However, the behavior of W films, with tailored properties, when exposed to pure He or mixed He-D, is not addressed in depth. The mixed He-D plasma, used in this preliminary investigation, had a total flux of about $7.1 \cdot 10^{21}$ m^{-2}s^{-1} and it was possible to achieve a total fluence of about $1.1 \cdot 10^{26}$ m^{-2} with 4 hour-long exposure. The temperature of samples was about 320°C and the bias voltage was kept floating. In order to have a reference sample, bulk W specimen was exposed together with the other films. The film types selected were: c-W (both annealed in vacuum at 750°C and not), n-W (both annealed in vacuum at 750°C and not) and p-W (both annealed in vacuum at 750°C and not). Figure 5.22 reports morphological modification induced by the mixed He-D plasma on bulk W surface.

After the He-D plasma exposure, bulk W shows the formation of the so-called *fuzzy W* [111] that is directly due to the presence of He in the plasma. Figure 5.23 reports morphological modification of films after the mixed plasma exposure.

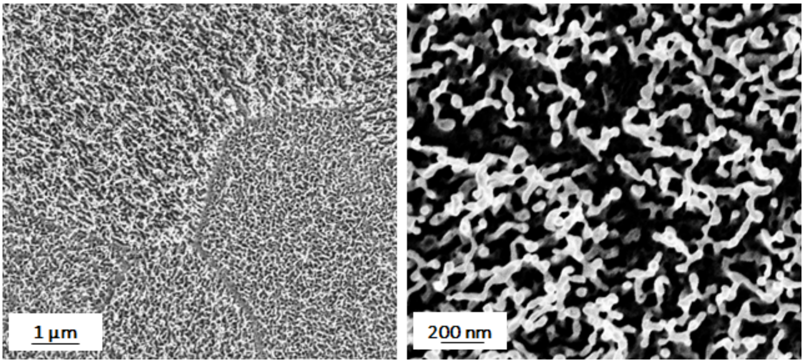

Figure 5.22: *SEM plain views of modifications induced by He-D plasma on bulk W surface.*

The formation of fuzzy W is evident only in the cases of the c-W and the annealed p-W, while the other samples do not exhibit these nanostructures. In particular, annealed c-W shows the formation of nanolamellae and p-W exhibits a diffuse crack network, while n-W and annealed n-W seem to not be affected by the He presence in the PSI-2 plasma. In general, it is possible to hypothesize that the fuzzy W formation could be related to the presence of contaminants in the exposed films: as a matter of fact, n-W, p-W and annealed-W exhibit a certain concentration of trapped O and these film types do not exhibit any fuzzy formation. On the other hand, both c-W and annealed c-W do not have O contamination

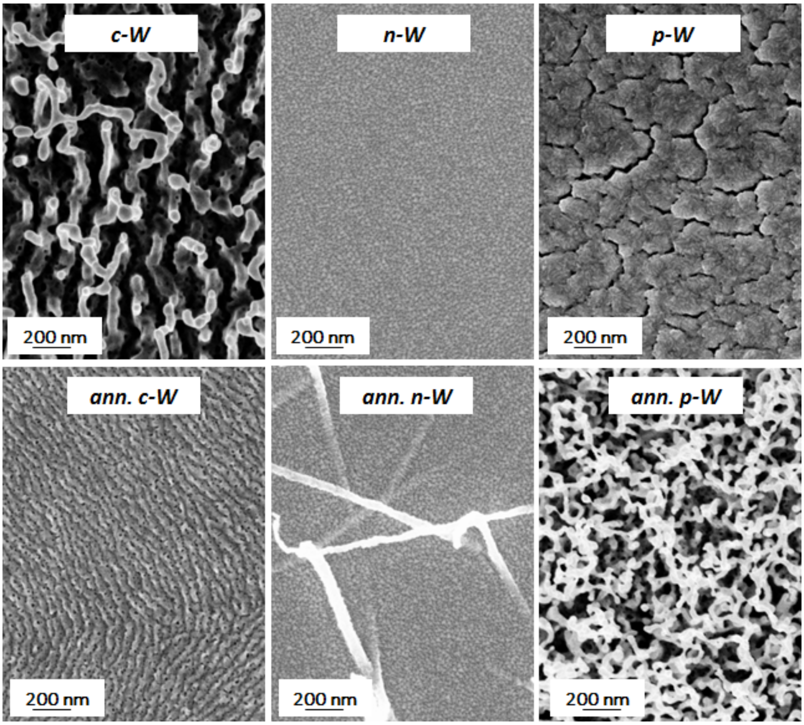

Figure 5.23: *SEM plain views of modifications induced by He-D plasma on surfaces of different film types.*

but the former highlights the fuzzy W formation while the latter shows the nanolamellae formation: this peculiar behavior can be ascribed to the thermal annealing treatments. Last but not least, annealed p-W exhibits fuzzy W formation and this is extremely difficult to interpret. Probably, this peculiar behavior can be due to the film nanostructure. To conclude, these are very peculiar results that must surely be investigated further, since it is not yet reported in any work in the literature.

5.4 He-loaded W-based films for developing Laser Induced Breakdown Spectroscopy

During the last period of this Ph.D., W-based films were loaded with He by using a high flux implanter, which is installed in the Instituto Superior Técnico (Lisbon, Portugal). In particular, nanostructured-W and porous-W samples, which have been described in depth in section 4.1.1, were implanted with consecutive He^+ ion flux by selecting the proper total fluence and impinging ion energy, as reported in table 5.4, in order to implant He ions at different depths.

Fluence $[\mathrm{He}^+]\mathrm{m}^{-2}$	**Power Density** $\mathrm{W/m}^2$	**Impinging Ion Energy** keV
$2 \cdot 10^{21}$	500	150
$2 \cdot 10^{21}$	500	100
$1 \cdot 10^{21}$	500	50

Table 5.4: *He implantation conditions to produce calibrated W-based samples*

Samples were characterized before and after the implantation by using RBS and Elastic Backscattering techniques (EBS). Actually, the only available data is that RBS spectra pointed out a significant He content in porous-W samples (up to 20 atomic %), while the other data is under investigation. The main goal is to produce samples with the desired properties and to load them with a specific amount of He (or other fusion-relevant ions) in order to have calibrated samples which can be used for the qualification of LIBS technique.

6

Conclusions and perspectives

THE main objective of this Ph.D. thesis was to study the properties of non-conventional tungsten-based layers with features resembling those which could be found on Plasma Facing Materials (PFMs), both in present-day tokamaks and in a future fusion reactor, and their behaviors and modifications when faced to divertor-like plasmas.

Nowadays, nuclear fusion is an attractive option for satisfying energy demands because it makes it possible to produce energy on a large scale by using cheap and abundant fuels with negligible levels of greenhouse emissions (chapter 1). One of the most studied design solutions for a fusion power plant uses suitable magnetic fields to confine a hot (temperatures of about 10^8 K) deuterium-tritium plasma in a torus shape, in devices called tokamaks. The most advanced experiment focused on controlled nuclear fusion is the ITER project, which is scheduled to start its operations in 2025 with the ambitious goal of proving the scientific feasibility of fusion energy production. In ITER and in future reactors (like the proposed demonstrative plant DEMO, scheduled for the 2030s/2040s), outstanding scientific and technological challenges must be faced, many of which relate to the interaction between thermonuclear plasma and PFMs.

As described in chapter 2, during plasma discharges, PFMs must withstand extreme conditions, such as very energetic neutrons (14.1 MeV neutrons able to generate radiation fields of about $2 \cdot 10^3$ Gy s^{-1}) and high particle fluxes (up to 10^{24} m^{-2}s^{-1}), as well as extreme heat loads (20 MW m^{-2} during steady-state operations and 10 GW m^{-2} during off-normal events). These phenomena induce severe modifications on PFMs, which can lead to erosion and sputtering processes. The eroded materials can migrate and re/co-deposit in other regions of the first wall, depending on tokamak geometry and design. These layers typically exhibit different properties with regard to those of pristine PFMs, e.g. re/co-deposits can retain a high amount of fuel mainly due to their complex features. In order to minimize these effects, different materials have been studied as PFMS. Among the tested materials, tungsten (W) has shown a good capability of facing thermonuclear plasmas because of its properties (high melt temperature, high thermal conductivity, low sputtering yield and low hydrogen isotope permeability and solubility). In particular, ITER divertor is made of W monoblocks that are actively cooled. In order to support ITER design, different present-day tokamaks changed their first wall:

- the ASDEX-UpGrade has a full W first wall;
- the JET-*ITER-Like Wall* has beryllium tiles in the blanket region and a full W divertor, like ITER PFMs configuration;
- the WEST project foresees the investigation of actively cooled W monoblock design in the divertor region in a quasi steady state plasma.

Even though operative conditions of these present-day tokamaks are not comparable with those foreseen for ITER and future reactors, their harsh environments make it possible to obtain first insights about material damage, material erosion, migration, mixing and re/co-deposition phenomena. These W-based re/co-deposited layers show complex morphologies, structures, elemental compositions and stoichiometries. Due to their peculiar features, re/co-deposited layers can retain extremely high amounts of hydrogen isotopes. Since the availability of layers made in tokamak environments is limited, it is essential to develop a material science approach which consists of depositing, via a suitable technique, coatings with desired and fusion-relevant properties and of testing these materials in dedicated linear devices which make it possible to simulate divertor-like plasma.

This Ph.D. thesis aimed to provide an experimental investigation, at the laboratory scale, to study non-conventional W-based layers and their behaviors when faced to divertor-like plasma. The goals of this thesis were (chapter 3):

- to produce, by using a suitable deposition technique and thermal annealing treatments, W-based coatings to investigate the above mentioned topics which are relevant in magnetic nuclear fusion research;
- to characterize these systems via suitable analysis techniques;

- to expose these tailored films to divertor-like plasmas and address the relationship between film properties, hydrogen isotope retention and modifications induced by plasma itself.

The Pulsed Laser Deposition (PLD) technique (see section 3.2.1) was used to produce different W-based films. In addition, thermal annealing treatments were used both to study modifications induced by ITER-relevant temperatures and to have an extra degree of freedom to control film properties. In addition, thanks to the collaborations developed in the framework of EUROfusion Work Plans, selected W-based films were exposed to ITER-relevant plasmas, which were produced by the PILOT-PSI, Magnum-PSI and PSI-2 linear devices (see section 3.4). These machines can work either in a pulsed or steady-state regime: the former can produce high flux plasma shots, while the latter can generate low flux continuous plasma.

The production of relevant W-based films had been focused on depositing films with controlled morphologies, structures, elemental compositions and stoichiometries in order to produce coatings that are relevant for magnetic fusion research (chapter 4).

In particular it was possible to deposit metallic W, W-O and W-N films with new and complex morphologies.

In order to achieve these results, the deposition conditions were carefully optimized. In particular, helium, argon, oxygen, nitrogen and mixed atmospheres were explored.

These investigations focused on the possibility of finely controlling film morphology and structure by selecting deposition pressure and the gas type. In particular, low pressures make it possible to obtain compact films, while high pressures induce porous morphology formations. Moreover, it was highlighted that porous film morphology naturally induces gas inclusion within the films. Coatings, which were deposited in a reactive atmosphere (i.e. oxygen and nitrogen), exhibit a threshold deposition pressure, above which oxide or nitride formation occurs and below which metallic films with a high gas inclusion were made.

Thermal annealing treatments make it possible to control both film structure and gas content. In particular, it was highlighted that the crystallization temperature in these metastable systems is lower than that of bulk W. Moreover, electrical resistivity measurements of annealed films, which were done in order to evaluate the overall system status, make it possible to show the variation of defects and impurities in films with regard to annealing temperature and to qualitatively quantify the recovery processes with regard to annealing temperature. Moreover, these temperature in-

vestigations highlighted a collateral aspect that is of particular interest: W-oxide nanowire nucleation was possible in a very interesting regime by opportunely calibrating oxygen content in films and annealing temperatures.
These results showed that PLD - thanks to its versatility and its capability to control material properties down to the nanoscale - may be an ideal tool for producing, at the laboratory scale, the complex re/co-deposition phenomena occurring in fusion devices. Moreover, the properties of these films can be further tailored by opportune thermal annealing procedures.

Some selected W-based films were exposed to deuterium (D) tokamak-relevant plasmas to study their retention behavior and morphological modifications with regard to their as-deposited properties (chapter 5). The exposed samples can be divided into metallic-W samples and W-O samples.
In particular, in the case of metallic-W films, it was highlighted that both high-flux plasma (10^{24} $m^{-2}s^{-1}$) and low-flux plasma (10^{21} $m^{-2}s^{-1}$) induce morphological modifications and D retention values that are comparable in the same film types.
The D retention and morphological modifications strongly depend on the defect density of coatings. In particular, high defect densities induce large D retention values, up to 20 times higher compared with bulk W, and intense morphological modifications. Interestingly, it was highlighted that a linear dependence seems to exist between D retention and film mean crystallite sizes, while a non-obvious dependence appears between D retention and film oxygen content, on the other hand. In particular, it was demonstrated that films with a similar morphology and different oxygen contents (from 15 up to 70 at. %) retain comparable amounts of D.
Oxide-W films were exposed to high flux D plasma and the results showed that oxide-W films change their properties after plasma exposures. This leads to oxygen loss, morphological modifications and oxide amortization: all these phenomena depend strongly on exposure temperature. Due to the modifications induced by different temperature exposures, the D retention values are different. It was highlighted that D plasma exposures induce the formation of an oxygen-depleted layer. In the case of low temperatures, this layer is superficial, and vice versa for high temperatures. Moreover, it is known that the mobility of D in W is higher in higher temperature regimes. For all these reasons, the D retention values found in similar films but exposed in different temperature regimes (low temperature regime 300°C and high temperature regime 600°C) are different. In addition, the multilayer systems, made of thick metallic-W film and a

thin oxide-W film, were exposed to D plasma. The results showed that the presence of this thin oxide-W layer deeply modifies D retention behavior by acting like a *passivation* layer.
In conclusion, preliminary exposure to a mixed helium-deuterium plasma of some W-based samples was also performed. Some of these samples exhibit the formation of fuzzy-W while others do not show any nanostructuration.

Further activities based on this Ph.D project could be

- to deposit additional W-nitrogen films with a higher film property control, e.g. gas content control, by keeping constant the desired morphology (i.e. compact or porous); this was already partially done by using a mixed atmosphere made of Ar and N_2 strategy during the deposition process;
- to characterize defect types in W-based films with specific techniques: in particular it will be possible to perform Positron Annihilation Spectroscopy (PAS) or develop a dedicated TDS campaign in order to define the defects' energy;
- to obtain the D retention in films with depth-resolution: NRA measurements, where the incident ion beam energy is opportunely changed, make it possible to achieve this result while ERDA measurements make it possible to study the surface film composition;
- to further explore the role of oxygen in D retention behaviors;
- to deepen mixed D-He plasma exposures.

In conclusion, in this Ph.D. thesis, the material science approach was wisely mixed with experimental plasma physics applied to study the plasma-wall interactions. This combination has brought tangible and fruitful results, which open the way to further investigations that use this approach.

List of Figures

List of Tables

Bibliography

[1] K. Krane. *Introductory nuclear physics.* Wiley, New York, 1988.

[2] C. Lombardi. *Impianti nucleari.* Polipress, Milano, 2009.

[3] J. D. Lawson. Some criteria for a power producing thermonuclear reactor. *Proceedings of the Physical Society. Section B*, 70(1):6–10, 1957.

[4] O. A. Hurricane, D. A. Callahan, D. T. Casey, et al. Fuel gain exceeding unity in an inertially confined fusion implosion. *Nature*, 506(7488):343–348, 2014.

[5] N. J. Peacock, D. C. Robinson, M. J. Forrest, P. D. Wilcock, and V. V. Sannikov. Measurement of the electron temperature by thomson scattering in tokamak T3. *Nature*, 224(5218):488–490, 1969.

[6] M. Keilhacker, A. Gibson, C. Gormezano, et al. High fusion performance from deuterium-tritium plasmas in JET. *Nucl. Fusion*, 39(2):209–234, 1999.

[7] Web page of ITER: `http://www.iter.org`.

[8] J. Wesson and D. J. Campbell. *Tokamaks.* International Series of Monographs on Physics. OUP Oxford, 2011.

[9] D. Stork. Neutral beam heating and current drive systems. *Fusion Engineering and Design*, 14(1):111–133, 1991.

[10] D. Q. Hwang and J. R. Wilson. Radio frequency wave applications in magnetic fusion devices. *Proceedings of the IEEE*, 69(8):1030–1043, 1981.

[11] I. H. Hutchinson. *Principles of Plasma Diagnostics*. Cambridge University Press, 2005.

[12] Web page of EUROfusion: `www.euro-fusion.org`.

[13] G. M. Olynyk, Z. S. Hartwig, D. G. Whyte, et al. Vulcan: A steady state tokamak for reactor relevant plasma material interaction science. *Fusion Engineering and Design*, 87(3):224–233, 2012.

[14] G. S. Was. *Fundamentals of Radiation Materials Science: Metals and Alloys*. Springer Berlin Heidelberg, 2011.

[15] M. R. Gilbert and J.-Ch. Sublet. Neutron-induced transmutation effects in W and W-alloys in a fusion environment. *Nuclear Fusion*, 51(4):043005, 2011.

[16] M. R. Gilbert, S. L. Dudarev, S. Zheng, L. W. Packer, and J. Ch. Sublet. An integrated model for materials in a fusion power plant: transmutation, gas production, and helium embrittlement under neutron irradiation. *Nuclear Fusion*, 52(8):083019, 2012.

[17] T. Tanno, A. Hasegawa, J. Ch. He, et al. Effects of transmutation elements on neutron irradiation hardening of tungsten. *Materials Transactions*, 48(9):2399–2402, 2007.

[18] A. Hasegawa, M. Fukuda, S. Nogami, and K. Yabuuchi. Neutron irradiation effects on tungsten materials. *Fusion Engineering and Design*, 89(7-8):1568–1572, 2014.

[19] J. Knaster, F. Arbeiter, P. Cara, et al. IFMIF, the European-Japanese efforts under the broader approach agreement towards a Li(d,xn) neutron source: Current status and future options. *Nuclear Materials and Energy*, pages –, 2016.

[20] J. Roth, E. Tsitrone, A. Loarte, et al. Recent analysis of key plasma wall interactions issues for ITER. *Journal of Nuclear Materials*, 390-391:1–9, 2009.

[21] A.S. Kukushkin, H.D. Pacher, V. Kotov, et al. Effect of neutral transport on ITER divertor performance. *Nuclear Fusion*, 45(7):608, 2005.

[22] G. F. Matthews. Material migration in divertor tokamaks. *Journal of Nuclear Materials*, 337-339:1–9, 2005.

[23] R. A. Pitts, J. P. Coad, D. P. Coster, et al. Material erosion and migration in tokamaks. *Plasma Physics and Controlled Fusion*, 47(12B):B303, 2005.

[24] M. Mayer, S. Krat, W. Van Renterghem, et al. Erosion and deposition in the JET divertor during the first ILW campaign. *Physica Scripta*, 2016(T167):014051, 2016.

[25] M. J. Rubel, G. Sergienko, A. Kreter, et al. An overview of fuel retention and morphology in a castellated tungsten limiter. *Fusion Engineering and Design*, 83(7-9):1049–1053, 2008.

[26] B.D. Wirth, K. Nordlund, D. G. Whyte, and D. Xu. Fusion materials modeling: Challenges and opportunities. *MRS Bulletin*, 36:216–222, 2011.

[27] M. H. J. t Hoen, B. Tyburska-Puschel, K. Ertl, et al. Saturation of deuterium retention in self-damaged tungsten exposed to high-flux plasmas. *Nuclear Fusion*, 52(2):023008, 2012.

[28] R. Frauenfelder. Permeation of hydrogen through tungsten and molybdenum. *The Journal of Chemical Physics*, 48(9), 1968.

[29] S. Brezinsek. Plasma-Surface interaction in the Be/W environment: Conclusions drawn from the JET-ILW for ITER. *Journal of Nuclear Materials*, 463:11–21, 2015.

[30] I. Ribeiro, C. Damiani, A. Tesini, et al. The remote handling systems for ITER. *Fusion Engineering and Design*, 86(6-8):471–477, 2011.

[31] J. Paméla, G.F. Matthews, V. Philipps, and R. Kamendje. An ITER-like wall for JET. *Journal of Nuclear Materials*, 363-365:1–11, 2007.

[32] W. R. Morcom, W. L. Worrell, H. G. Sell, and H. I. Kaplan. The preparation and characterization of beta-tungsten, a metastable tungsten phase. *Metallurgical Transactions*, 5(1):155–161, 1974.

[33] D. Maisonnier, I. Cook, P. Sardain, et al. DEMO and fusion power plant conceptual studies in europe. *Fusion Engineering and Design*, 81(8-14):1123–1130, 2006.

[34] K. Kim, H. C. Kim, S. Oh, et al. A preliminary conceptual design study for korean fusion DEMO reactor. *Fusion Engineering and Design*, 88(6-8):488–491, 2013.

[35] F. Romanelli and on behalf of JET Contributors.

[36] R. Neu, K. Asmussen, K. Krieger, et al. The tungsten divertor experiment at ASDEX Upgrade. *Plasma Physics and Controlled Fusion*, 38(12A):A165, 1996.

[37] J. Bucalossi, M. Missirlian, P. Moreau, et al. The WEST project: Testing ITER divertor high heat flux component technology in a steady state tokamak environment. *Fusion Engineering and Design*, 89(7-8):907–912, 2014.

[38] K. Krieger, H. Maier, and R. Neu. Conclusions about the use of tungsten in the divertor of ASDEX Upgrade. *Journal of Nuclear Materials*, 266-269:207–216, 1999.

[39] R. Neu, V. Bobkov, R. Dux, et al. Ten years of W programme in ASDEX Upgrade-challenges and conclusions. *Physica Scripta*, 2009(T138):014038, 2009.

[40] S. Deschka, C. GarcÃía-Rosales, W. Hohenauer, et al. Manufacturing and high heat flux loading of tungsten coatings on fine grain graphite for the ASDEX-Upgrade divertor. *Journal of Nuclear Materials*, 233:645–649, 1996.

[41] H. Maier and S. K˙Performance of tungsten coatings as plasma facing components used in ASDEX upgrade. *Journal of Nuclear Materials*, 258-263, Part 1:921–926, 1998.

[42] H. Maier, J. Luthin, M. Balden, et al. Properties of tungsten coatings deposited onto fine grain graphite by different methods. *Surface and Coatings Technology*, 142-144:733–737, 2001.

[43] A. Cambe, E. Gauthier, J. M. Layet, and S. Bentivegna. Development of tungsten coating for fusion applications. *Fusion Engineering and Design*, 56-57:331–336, 2001.

[44] H. Maier, R. Neu, H. Greuner, et al. Tungsten coatings for the JET ITER-like wall project. *Journal of Nuclear Materials*, 363-365:1246–1250, 2007.

[45] C. Ruset, E. Grigore, H. Maier, et al. Tungsten coatings deposited on CFC tiles by the combined magnetron sputtering and ion implantation technique. *Physica Scripta*, 2007(T128):171, 2007.

[46] C. Ruset, E. Grigore, I. Munteanu, et al. Industrial scale 10 Î¼m W coating of CFC tiles for ITER-like Wall Project at JET. *Fusion Engineering and Design*, 84(7-11):1662–1665, 2009.

[47] C. Ruset, E. Grigore, H. Maier, et al. Development of W coatings for fusion applications. *Fusion Engineering and Design*, 86(9-11):1677–1680, 2011.

[48] A. Herrmann, H. Greuner, N. Jaksic, et al. Solid tungsten Divertor-III for ASDEX Upgrade and contributions to ITER. *Nuclear Fusion*, 55(6):063015, 2015.

[49] H. Maier, R. Neu, H. Greuner, et al. Qualification of tungsten coatings on plasma-facing components for JET. *Physica Scripta*, 2009(T138):014031, 2009.

[50] G. F. Matthews, P. Coad, H. Greuner, et al. Development of divertor tungsten coatings for the JET ITER-like wall. *Journal of Nuclear Materials*, 390-391:934–937, 2009.

[51] K. Heinola, A. Widdowson, J. Likonen, et al. Fuel retention in JET ITER-Like Wall from post-mortem analysis. *Journal of Nuclear Materials*, 463:961–965, 2015.

[52] K. Heinola, A. Widdowson, J. Likonen, et al. Long-term fuel retention in JET ITER-like wall. *Physica Scripta*, 2016(T167):014075, 2016.

[53] S. Brezinsek, T. Loarer, V. Philipps, et al.

[54] D. Guilhem, J. Bucalossi, S. Burles, et al. Tungsten covered graphite and copper elements and ITER-like actively cooled tungsten divertor plasma facing units for the WEST project. *Physica Scripta*, 2016(T167):014066, 2016.

[55] B. J. Braams. Characterization of Size, Composition and Origins of Dust in Fusion Devices. Summary Report of the Third Research Coordination Meeting. 2013.

[56] A. Baron-Wiechec, E. Fortuna-Zalesna, J. Grzonka, et al. First dust study in JET with the ITER-like wall: sampling, analysis and classification. *Nuclear Fusion*, 55(11):113033, 2015.

[57] D. Ivanova, M. Rubel, A. Widdowson, et al. An overview of the comprehensive First Mirror Test in JET with ITER-like wall. *Physica Scripta*, 2014(T159):014011, 2014.

[58] M. Balden, N. Endstrasser, P. W. Humrickhouse, et al.

[59] M. Rasinski, E. Fortuna-Zalesna, M. Mayer, et al. High resolution scanning transmission electron microscopy (HR STEM) analysis of re-deposited layer on ASDEX Upgrade tile. *Fusion Engineering and Design*, 86(9-11):1753–1756, 2011.

[60] A. Litnovsky, M. Matveeva, A. Herrmann, et al. First studies of ITER-diagnostic mirrors in a tokamak with an all-metal interior: results of the first mirror test in ASDEX Upgrade. *Nuclear Fusion*, 53(7):073033, 2013.

[61] W. R. Wampler and R. P. Doerner. The influence of displacement damage on deuterium retention in tungsten exposed to plasma. *Nuclear Fusion*, 49(11):115023, 2009.

[62] M. Shimada, Y. Hatano, P. Calderoni, et al. First result of deuterium retention in neutron-irradiated tungsten exposed to high flux plasma in TPE. *Journal of Nuclear Materials*, 415(1, Supplement):S667 – S671, 2011.

[63] O.V. Ogorodnikova, V.V. Gann, M.S. Zibrov, and Yu.M. Gasparyan. Comparison of deuterium retention in tungsten pre-damaged with energetic electrons, self-ions and neutrons. *Physics Procedia*, 71:41–46, 2015.

[64] B. Tyburska, V. Kh. Alimov, O. V. Ogorodnikova, K. Schmid, and K. Ertl. Deuterium retention in self-damaged tungsten. *Journal of Nuclear Materials*, 395(1-3):150–155, 2009.

[65] V. Kh. Alimov, Y. Hatano, B. Tyburska-PÃ¼schel, et al. Deuterium retention in tungsten damaged with W ions to various damage levels. *Journal of Nuclear Materials*, 441(1-3):280–285, 2013.

[66] O. V. Ogorodnikova, B. Tyburska, V. Kh. Alimov, and K. Ertl. The influence of radiation damage on the plasma-induced deuterium retention in self-implanted tungsten. *Journal of Nuclear Materials*, 415(1, Supplement):S661–S666, 2011.

[67] Y. Hatano, M. Shimada, T. Otsuka, et al. Deuterium trapping at defects created with neutron and ion irradiations in tungsten. *Nuclear Fusion*, 53(7):073006, 2013.

[68] Y. Oya, M. Shimada, M. Kobayashi, et al. Comparison of deuterium retention for ion-irradiated and neutron-irradiated tungsten. *Physica Scripta*, 2011(T145):014050, 2011.

[69] D. Dellasega, G. Merlo, C. Conti, C. E. Bottani, and M. Passoni. Nanostructured and amorphous-like tungsten films grown by pulsed laser deposition. *Journal of Applied Physics*, 112(8), 2012.

[70] A. Pezzoli, D. Dellasega, V. Russo, et al. Thermal annealing and exposure to divertor-like deuterium plasma of tailored tungsten oxide coatings. *Journal of Nuclear Materials*, 463:1041–1044, 2015.

[71] M. H. J. t Hoen, D. Dellasega, A. Pezzoli, et al. Deuterium retention and surface modifications of nanocrystalline tungsten films exposed to high-flux plasma. *Journal of Nuclear Materials*, 463:989–992, 2015.

[72] P. Wang, W. Jacob, L. Gao, S. Elgeti, and M. Balden. Deuterium retention in tungsten films deposited by magnetron sputtering. *Physica Scripta*, 2014(T159):014046, 2014.

[73] P. Wang, W. Jacob, and S. Elgeti. Deuterium retention in tungsten films after different heat treatments. *Journal of Nuclear Materials*, 456:192–199, 2015.

[74] P. Gasior, M. Bieda, M. Kubkowska, R. Neu, and J. Wolowski. Laser induced breakdown spectroscopy as diagnostics for fuel retention and removal and wall composition in fusion reactors with mixed-material components. *Fusion Engineering and Design*, 86(6-8):1239–1242, 2011.

[75] S. Amoruso, B. Toftmann, and J. Schou. Thermalization of a uv laser ablation plume in a background gas: From a directed to a diffusion-like flow. *Phys. Rev. E*, 69:056403, May 2004.

[76] R. Eason. *Pulsed laser deposition of thin films: applications-led growth of functional materials.* Wiley-Interscience, 2007.

[77] D.B. Chrisey and G.K. Hubler. *Pulsed Laser Deposition of Thin Films.* Wiley, 1994.

[78] L. van der Pauw. A method of measuring specific resistivity and hall effect of discs of arbitrary shape. *Philips Res. Rep.*, 13:1–9, 1958.

[79] G. J. van Rooij, V. P. Veremiyenko, W. J. Goedheer, et al. Extreme hydrogen plasma densities achieved in a linear plasma generator. *Applied Physics Letters*, 90(12), 2007.

[80] B. de Groot, Z. Ahmad, R.P. Dahiya, et al. Magnum-psi, a new linear plasma generator for plasma-surface interaction studies in ITER relevant conditions. *Fusion Engineering and Design*, 66-68:413–417, 2003.

[81] B. Unterberg, R. Jaspers, R. Koch, et al. New linear plasma devices in the trilateral euregio cluster for an integrated approach to plasma surface interactions in fusion reactors. *Fusion Engineering and Design*, 86(9-11):1797–1800, 2011.

[82] P.A. Redhead. Thermal desorption of gases. *Vacuum*, 12(4):203–211, 1962.

[83] M. Mayer. SIMNRA, a simulation program for the analysis of NRA, RBS and ERDA. *AIP Conference Proceedings*, 475(1), 1999.

[84] F. Di Fonzo, A. Bailini, V. Russo, et al. Synthesis and characterization of tungsten and tungsten oxide nanostructured films. *Catalysis Today*, 116(1):69 – 73, 2006.

[85] J.N. Brooks, J.P. Allain, R.P. Doerner, et al. Plasma-surface interaction issues of an all-metal ITER. *Nuclear Fusion*, 49(3):035007, 2009.

[86] L. K. Keys, J. P. Smith, and J. Moteff. High-temperature recovery of tungsten after neutron irradiation. *Phys. Rev.*, 176:851–856, 1968.

[87] H. Schultz. Defect parameters of b.c.c. metals: group-specific trends. *Materials Science and Engineering: A*, 141(2):149 – 167, 1991.

[88] A. Debelle, M.F. Barthe, and T. Sauvage. First temperature stage evolution of irradiation-induced defects in tungsten studied by positron annihilation spectroscopy. *Journal of Nuclear Materials*, 376(2):216–221, 2008.

[89] E. Markina, M. Mayer, A. Manhard, and T. Schwarz-Selinger. Recovery temperatures of defects in tungsten created by self-implantation. *Journal of Nuclear Materials*, 463:329–332, 2015.

[90] D. Dellasega, S. M. Pietralunga, A. Pezzoli, et al. Tungsten oxide nanowires grown on amorphous-like tungsten films. *Nanotechnology*, 26(36):365601, 2015.

[91] E. Besozzi, D. Dellasega, A. Pezzoli, et al. Amorphous, ultra-nano- and nano-crystalline tungsten-based coatings grown by pulsed laser deposition: mechanical characterization by surface brillouin spectroscopy. *Materials & Design*, 106:14-21, 2016.

[92] A. Ponzoni, V. Russo, A. Bailini, et al. Structural and gas-sensing characterization of tungsten oxide nanorods and nanoparticles. *Sensors and Actuators B: Chemical*, 153(2):340–346, 2011.

[93] J. Gabrusenoks, A. Veispals, A. von Czarnowski, and K.-H. Meiwes-Broer. Infrared and raman spectroscopy of WO3 and CdWO4. *Electrochimica Acta*, 46(13-14):2229–2231, 2001.

[94] G.L. Frey, A. Rothschild, J. Sloan, et al. Investigations of non-stoichiometric tungsten oxide nanoparticles. *Journal of Solid State Chemistry*, 162(2):300–314, 2001.

[95] T.T. Sheng, R.B. Marcus, F. Alexander, and W.A. Reed. Structural and electrical properties of sputtered tungsten films. *Thin Solid Films*, 14(2):289–298, 1972.

[96] G. M. Mikhailov, A. V. Chernykh, and V. T. Petrashov. Electrical properties of epitaxial tungsten films grown by laser ablation deposition. *Journal of Applied Physics*, 80(2):948–951, 1996.

[97] J. Ligot, S. Benayoun, and J. J. Hantzpergue. Characterization and modeling of electrical resistivity of sputtered tungsten films. *Journal of Vacuum Science and Technology A*, 19(3):798–804, 2001.

[98] G.S. Chen, L.C. Yang, H.S. Tian, and C.S. Hsu. Evaluating substrate bias on the phase-forming behavior of tungsten thin films deposited by diode and ionized magnetron sputtering. *Thin Solid Films*, 484(1-2):83–89, 2005.

[99] Angela Furrer, Matteo Seita, and Ralph Spolenak. The effects of defects in purple aual2 thin films. *Acta Materialia*, 61(8):2874–2883, 2013.

[100] K. Fuchs and N. F. Mott. The conductivity of thin metallic films according to the electron theory of metals. *Mathematical Proceedings of the Cambridge Philosophical Society*, 34(01):100, 1938.

[101] A. F. Mayadas and M. Shatzkes. Electrical-resistivity model for polycrystalline films: the case of arbitrary reflection at external surfaces. *Physical Review B*, 1:1382–1389, 1970.

[102] D. Choi, C. S. Kim, D. Naveh, et al. Electron mean free path of tungsten and the electrical resistivity of epitaxial (110) tungsten films. *Physical Review B*, 86(4), 2012.

[103] D. Choi. The electron scattering at grain boundaries in tungsten films. *Microelectronic Engineering*, 122:5–8, 2014.

[104] K. R. Reyes-Gil, C. Wiggenhorn, B. S. Brunschwig, and N. S. Lewis.

[105] R. Seelaboyina, J. Huang, J. Park, D. H. Kang, and W. B. Choi. Multistage field enhancement of tungsten oxide nanowires and its field emission in various vacuum conditions. *Nanotechnology*, 17(19):4840, 2006.

[106] G. Gu, B. Zheng, W. Q. Han, S. Roth, and J. Liu.

[107] C. H. Chen, S. J. Wang, R. M. Ko, et al. The influence of oxygen content in the sputtering gas on the self-synthesis of tungsten oxide nanowires on sputter-deposited tungsten films. *Nanotechnology*, 17(1):217, 2006.

[108] A.S Argon and S.R Maloof. Plastic deformation of tungsten single crystals at low temperatures. *Acta Metallurgica*, 14(11):1449–1462, 1966.

[109] O. V. Ogorodnikova, J. Roth, and M. Mayer. Ion-driven deuterium retention in tungsten. *Journal of Applied Physics*, 103(3), 2008.

[110] M. H. J. 't Hoen, M. Mayer, A. W. Kleyn, and P. A. Zeijlmans van Emmichoven. Strongly reduced penetration of atomic deuterium in radiation-damaged tungsten. *Phys. Rev. Lett.*, 111:225001, 2013.

[111] M.J. Baldwin and R.P. Doerner. Formation of helium induced nanostructure fuzz on various tungsten grades. *Journal of Nuclear Materials*, 404(3):165–173, 2010.

[112] R.P. Doerner, M.J. Baldwin, and P.C. Stangeby. An equilibrium model for tungsten fuzz in an eroding plasma environment. *Nuclear Fusion*, 51(4):043001, 2011.